# Development of a realistic computer model of the human ventricles for the study of reentrant arrhythmias

Olivier G. Bernus

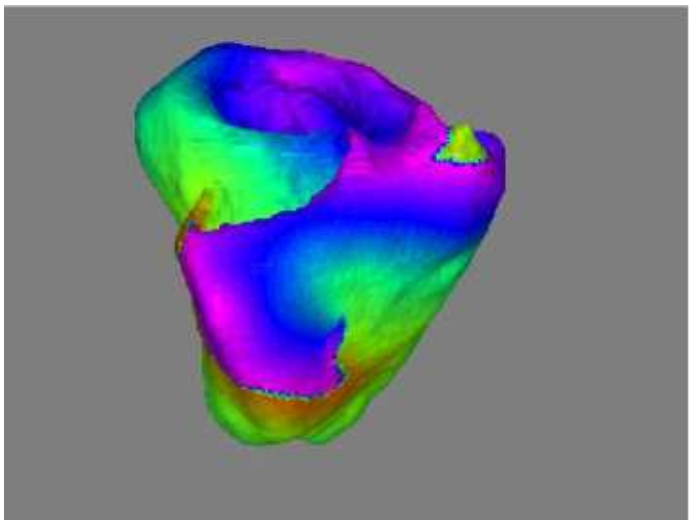

Proefschrift ingediend aan de Faculteit Wetenschappen
tot het behalen van de graad van
Doctor in de Wetenschappen: Natuurkunde

Promotor: Prof. Dr. H. Verschelde
Co-promotor: Prof. Dr. A.V. Panfilov

Universiteit Gent
Faculteit Wetenschappen
Vakgroep Wiskundige Natuurkunde en sterrenkunde
Academiejaar 2002-2003

UNIVERSITEIT GENT

> Models are always, necessarily, partial representations of reality. Their aim is understanding and explanation in a simplified representation, and this must consist partly in determining what features of a system are necessary and sufficient to understand it. [...] That is the power of a model. A complete representation - a clone of reality - would not do that. It would leave us just as wise, or as ignorant, as before.

D. Noble, "Biological Computation", in *Encyclopedia of the Life Sciences*.

# Dankwoord

Deze thesis is mogelijk gemaakt door de bijdrage van vele mensen. Allereerst zou ik Henri willen bedanken om mij de kans te hebben gegeven dit doctoraat aan te vatten, al lag het onderwerp ervan buiten zijn onderzoeksgebied. Ik zou hem willen bedanken voor het vertrouwen en voor de vrijheid bij het richting geven aan mijn werk en voor het nalezen van deze thesis. Bijzondere dank gaat uit naar Sasha: voor alle vertrouwen gedurende deze vier jaren, voor het blijvend optimisme dat me steeds weer kon motiveren, voor de vele contacten met andere onderzoeksgroepen en voor alle hulp op wetenschappelijk vlak, zonder dewelke een groot deel van dit werk onmogelijk zou geweest zijn.

Dank aan Christian Zemlin en Ronald Wilders voor de vruchtvolle samenwerking met betrekking tot het rPB model en ook aan Kirsten ten Tusscher voor de software en de discussies. Dank aan Rok Hren om de anatomische data van de menselijke ventrikels ter beschikking te stellen. Dank aan Denis en Penny Noble, Arkadii Pertsov en Léon Glass voor de vaak korte maar uiterst boeiende studieverblijven in Oxford, Syracuse en Montréal. Dank aan Christian voor het verblijf in Syracuse en het experiment op een varkenshart. Eveneens dank aan Richard Clayton, Martyn Nash, Marcel Wellner en Albert Goldbeter voor de uiterst interessante gesprekken.

Wijnand wens ik hier ook te bedanken, voor de inwijding in de wondere wereld van C/C++, voor de talloze discussies (en niet enkel over wetenschap) en om het mij hier in het begin wegwijs te maken. Bij deze bedank ik eveneens Bavo, voor het doorgeven van zijn style-files en voor alle nuttige tips bij het schrijven van deze thesis, en Gerbrand, die ik te pas en te onpas kwam lastig vallen over een vermeend "technisch probleempje". Ook dank aan Frans, Willy, Tom, Frank, Gerald, David, Jos, Karel, Hugo, Anny en de andere vakgroepcollega's voor de leuke babbels tussendoor.

Ik zou eveneens van de gelegenheid willen gebruik maken om Karel Vereecke, Beatrijs Van Eyck en Sarah Van Laere te bedanken voor hun bijdrage als thesisstudenten.

Mijn ouders (en mijn zusje!) wens ik hier ook te bedanken voor hun liefde, vertrouwen, opvoeding, logistieke steun, en nog veel meer.

Deze thesis zou vrijwel onmogelijk geweest zijn zonder de nodige dosis ontspanning: dank aan Thomas, Elisabeth, Marc, Deirdre, Wouter, Cristina, Chris, Raf, Bavo, Hans, Karel en alle anderen voor de verjaardagsfeestjes, gezelschapsspelavonden, fuiven, ... . Dank ook aan de mannen van het "INW-minivoetbal" en de "Kringboys" voor de sportieve woensdag- en zaterdagmiddagen. Mijn broer wens ik ook te bedanken voor de reizen, de talloze etentjes, en de bowlingavonden met Karen, Carlos, Ilse en Bernard. Dank ook aan de BAS-cursisten en Yves voor de vele uren trommelplezier.

Tenslotte wens ik nog Nickou te bedanken voor alles wat ze is, voor alle liefde en om er steeds weer te zijn als het even minder goed ging.

Olivier Bernus
Maart 2003

# Contents

# Introduction

The mechanical contractions of the heart are triggered by electrical waves of excitation propagating through cardiac tissue. Transmission of information by waves of excitation is a common phenomenon in human and animal biology, and occurs in nervous and muscular systems, including the heart muscle. Modeling in cardiac electrophysiology is one of the most exciting and important examples of applications of methods of theoretical and computational physics in medicine and biology. The history of modeling biological excitable media such as nerve and heart tissue started 50 years ago with the Noble-price winning Hodgkin-Huxley model for propagation of excitation waves in nerve cells of the giant squid axon [Hodgkin and Huxley 1952]. Later, the modeling was extended to cardiac tissue by Noble [1962] and FitzHugh [1961] and these models were further adapted with an increasing accuracy [Beeler and Reuter 1977, Luo and Rudy 1991, 1994, Noble et al. 1998], as the experimental techniques for studying the properties of the cell membrane improved continuously. It turned out, that abnormalities in the wave propagation in the heart underlay the most dangerous cardiac arrhythmias and sudden cardiac death, accounting for about 1 death in 10 in industrialised countries [Winfree 1994].

From a physical point of view the heart is an excitable medium driven by limit-cycle oscillations [Glass 1996]. An excitable medium is a spatially distributed system in which a small but finite perturbation above a certain threshold leads to a large excursion away from equilibrium - an excitation - before equilibrium is restored. In the case of the heart, the excitation, or action potential, is associated with an electro-mechanical wave which induces the cardiac muscle contractions and causes the heart to pump deoxygenated blood to the lungs and oxygenated blood to the rest of the body. The propagation of excitation waves follows two main rules:

1. an excited cell can transmit excitation to its neighbours, initiating or conducting a wave of excitation.

2. some time after a wave has passed through the medium, a so-called refractory period sets in, during which a second wave cannot be initiated.

One of the most striking phenomenon in excitable media is the existence of reentrant patterns. If we consider a thin ring of excitable tissue and initiate a single wave propagating in one direction, than this wave will make a complete turn in the time $l/CV$, where $l$ denotes the circumference of the ring and $CV$ the conduction velocity. If this time is longer than the refractory period, than the wave will continue to rotate. This sustained rotation of a wave in a ring, or, in general, in the heart along a closed anatomical pathway, is an example of one-dimensional reentry.

This procedure can be extended in two dimensions, by considering a sheet of tissue with an inexcitable obstacle. Assume a straight wave front with an end touching the inexcitable obstacle, which starts propagating in one direction. Different points of the wave front will propagate along different trajectories: the point at the tip of the front will propagate around the inexcitable obstacle, while points far from the obstacle will follow a quasi linear trajectory.

This results in the curling of an initially straight wave front and the formation of a stationary spiral wave which rotates with some period around the obstacle. It turns out that such spiral waves can also exist in media without obstacles, where they rotate around the refractory tail of the wave tip.
In three dimensions we speak of scroll waves, which are curled around an organising center, called the filament. Scroll waves can have different shapes, depending on the geometry of the filament: simple scroll waves have a straight filament and are the most simple extension of a spiral wave in three dimensions as any cross section orthogonal to the filament yields a two-dimensional spiral wave. In some cases the filament can be a ring, and such waves are denoted as scroll rings. When the wave front is twisted around the filament, one speaks of twisted scroll.

Rotating spiral or scroll waves, also known as rotors [Winfree 1972] or vortices [Agladze and Krinsky 1982] occur in a wide variety of non-linear excitable media. Biological examples of such media include populations of *Dictyostelium discoideum* amoebae [Siegert and Weijer 1992], the retina [Gorelova and Bures 1983], *Xenopus* oocytes [Lechleiter et al. 1991] and heart tissue [Allessie et al. 1973, Davidenko et al. 1991]. In physico-chemical systems spiral waves have been observed in oscillating reactions [Zaikin and Zhabotinsky 1970, Winfree 1972] and heterogeneous catalysis [Rotermund et al. 1990].

If a spiral wave occurs in the heart, it will disturb the normal rhythm. In normal conditions the heart is activated by a natural pacemaker, which can be thought as consisting of cells which are limit-cycle oscillators. The period of oscillation of this pacemaker is regulated by the nervous system and determines the heart rate. It has been found that scroll waves in heart tissue have a period 2 to 3 times shorter than the period of the natural pacemaker. Hence, rotors suppress the pacemaker activity of the heart and induce a fast rhythm, which is called tachycardia, a serious cardiac disease. In many cases tachycardia deteriorate into a turbulent pattern of spatially unsynchronised excitation, which is called fibrillation.
The exact mechanism of fibrillation is still unknown, however, it is believed to be associated with complex dynamics of wave propagation in the heart. For almost four decades the dominating hypothesis of cardiac fibrillation was Moe's multiple wavelet hypothesis [Moe et al. 1964]. It describes fibrillation as wave patterns organised by multiple wandering wavelets which occur due to heterogeneity of cardiac tissue in the refractory period. Another hypothesis which is closely related, is 'induced fibrillation' [Jalife et al. 1998a,b]. It requires heterogeneities, but in this case the wavelets are induced by a stable high frequency source, and fibrillation disappears when the source is removed. Gray et al. [1995a] have proposed fast drifts of spiral waves as a possible mechanism of ventricular fibrillation. Other studies have tried to explain fibrillation as a decay of a stable spiral wave into a complex turbulent regime. Stability analysis has shown, that such decay can occur as a result of the process of spiral breakup: a successive self reproduction of new sources of excitation. Spiral breakup can be the result of an instability occurring after an infinite dimensional Hopf bifurcation [Courtemanche et al. 1993] or other mechanisms reviewed in [Fenton et al. 2002].
Similar mechanisms have been proposed for several other types of cardiac arrhythmias. For example, monomorphic tachycardia, which produce a periodic electrocardiogram, are believed to be associated with a stationary rotation of excitation in the heart [Pertsov et al. 1993]. Polymorphic ventricular tachycardia which produce a non-periodic electrocardiogram and torsades de pointes, which produce electrocardiograms similar to two-periodic motion, have recently been explained by non-stationary dynamics of spiral waves, with a degree of non-stationarity less than during ventricular fibrillation [Gray et al. 1995b].

An important fact to mention is that all these mechanisms have been observed in experiments on hearts of various animals: rabbit, dog, guinea pig, etc. Hearts of these animals differ from the human heart in size and tissue properties. Studies involving human hearts are very limited and the reasons are quite obvious: it is impossible to implant several hundreds of electrodes during an arrhythmia to investigate the wave patterns, or to stop the heart contractions for the optical mapping of waves of excitation, or perform similar procedures used in experimental electrophysiology. The only data available comes from multiple electrocardiogram recordings, some NMR images or measurements of the magnetic field generated by the electrical currents in the heart. Unfortunately, these data are not very accurate and give only a very general picture of the wave patterns in the human heart. Therefore, new methods should be developed for projecting results obtained in experiments on animal hearts to problems of arrhythmias in the human heart. It would also be important to connect wave patterns in the human heart to signals measurable in clinical investigations, such as electrocardiograms. One of the most promising methods with that respect, is that of computational modeling, which is already applied in several other branches of science, such as aerodynamics. The idea of realistic computer modeling of wave propagation in the heart is more than 20 years old (see review in [Panfilov 1997]). Old models were however anatomically inaccurate and had a bad spatial resolution in order to be applied to the study of cardiac arrhythmias. Recently a detailed model of the canine heart was developed in [Panfilov and Keener 1995a] on the basis of anatomical data presented by Nielson et al. [1991] and was successfully used for reproduction of experimental data of ventricular fibrillation [Gray et al. 1995b]. The number of such whole heart studies is however still very limited and they were not systematically applied to clinically important situations.

In this thesis we focus on the development of an anatomical computer model of the human ventricles, which can be applied to study reentrant arrhythmias. First of all we develop an accurate model which describes the electrophysiological properties of the human ventricular tissue and wave propagation in the ventricles. We also have anatomical data of the human ventricles in order to capture the complex geometry of the ventricles. This anatomical data furthermore include information on the orientation of the muscle fibers in each point of the ventricles, as it plays an important role in the spread of excitation through the cardiac muscle. Finally, we take care of the boundary conditions needed to integrate the equations in such a complex system.

## Outline

In the first chapter we introduce two models of the electrophysiological properties of the human ventricular tissue. The first model is a three-variable model which reproduces the general excitable properties of human ventricular cells in a phenomenological way. It is efficient for large scale computations but lacks electrophysiological accuracy. Based on ideas generated during the construction of this model, we developed an electrophysiological accurate and efficient six-variable model. This new model was obtained by a reduction of a second-generation ionic model constructed by Priebe and Breuckelmann [1998] (PB) and which was based on the Luo-Rudy type II models [Luo and Rudy 1994] (LR). Our model is more stable than the original PB model and retains the most important electrophysiological properties relevant to reentrant arrhythmias.

A brief overview of electrocardiography is given in Chapter 2. We discuss the generation of the electrocardiogram during normal cardiac activity. In electrocardiography a distinction

is usually made between the forward and the inverse problem. The forward problem deals with the formulation of models of the electrical sources in the heart, where the main aim is to compute the resulting potential in a field point. In most clinical applications however, the interest lies in determining the nature of the source from a set of potentials recorded at some distance from the heart. This is called the inverse problem.

The dynamics of spiral waves in two-dimensional sheets of cardiac tissue are studied in the third chapter. We investigate their stability properties in the case of the normal parameter values and when simulating the effects of potassium channel openers, e.g. cromakalim, which destabilise the spiral waves. We also simulate spiral waves in media with biphasic restitution curves and study how the biphasic bump can destabilise the reentrant source. Moreover, we show that a specific type of drugs can prevent the onset of instabilities or convert turbulent patterns in organised ones.

In Chapter 4 we investigate the possibility of using an intermediate class of models which, on one hand, retain a detailed description of the ionic currents, but, on the other hand, have the numerical efficiency of the so-called low-dimensional FitzHugh-Nagumo models. We start from the observation that in most ionic models the upstroke of the action potential is produced by the fast inward sodium current. This current plays a key role in the transmission of excitation, while it has almost no influence on other important properties of cardiac tissue. We present a method to modify this current in such a way that it preserves its main properties, but reduces the steepness of the upstroke. We show that using such a procedure, a good numerical accuracy can be obtained at large space steps, while the description of all other ionic currents is unaltered. The presented technique is general and can be applied to any ionic model. In three-dimensions we obtain a computational gain of up to a factor 20.

Chapter 5 deals with an anatomical model of the human ventricles which was obtained by Hren [1996]. We describe the methods used to obtain the anatomical data and incorporate the fiber orientation field based on measurements in human [Streeter 1979] and canine [Nielson et al. 1991] hearts. We validate the model by incorporating our reduced PB model and reproducing the activation patterns as observed in experiments by Durrer et al. [1970].

Finally, we extend the results of Chapter 3 to the anatomical model of the human ventricles. We begin by studying the stability of three-dimensional scroll waves induced at three distinct places in the ventricles. We then investigate the deterioration of stable scroll waves to turbulent patterns in the right ventricle by simulating the effects of a potassium-channel opener. Finally, we study the conversion from fibrillation to tachycardia by gradually blocking the calcium-channel in the model equations.

# I

# Models of the human ventricular tissue

In this chapter we start with a short introduction on the electrophysiological properties of cardiac tissue. We then introduce two models of the electrophysiological properties of the human ventricular tissue. The first model is a three-variable model which reproduces the general excitable properties of human ventricular cells in a phenomenological way. It is efficient for large scale computations but lacks electrophysiological accuracy. Based on ideas generated during the construction of this model, we developed an electrophysiological accurate and efficient six-variable model. This new model was obtained by a reduction of a second-generation ionic model constructed by Priebe and Breuckelmann [1998] (PB) and which was based on the Luo-Rudy type II models [Luo and Rudy 1994] (LR). Our model is more stable than the original PB model and retains the most important electrophysiological properties relevant to reentrant arrhythmias. We will refer to this model as the rPB model. We also pay attention to the so-called biphasic restitution curves and develop a method to adapt ionic models in order to reproduce experimentally measured biphasic restitution curves [Morgan et al. 1992b] in a straightforward way. We apply this method to the rPB model and call it the biphasic rPB model.

## 1 Introduction

### 1.1 The cell membrane

The smallest unit in living tissue is the cell, which is specialised in its anatomy and physiology to perform different tasks. All cells are enclosed by a cell membrane, consisting of a bilayer of phospholipid molecules. These molecules have a phosphoric acid head, that is attracted to water and glyceride tails, that are repelled by water. The tails of the two layers constituting the membrane are oriented towards each other, creating a barrier between the intra- and extracellular medium. These media are aqueous solutions of several ion species, which appear in different concentrations inside and outside the cell. This results in a voltage difference across the membrane. The membrane voltage or membrane potential $V_m$ of an excitable cell is defined as the potential at the inner surface relative to that at the outer surface of the cell membrane.

Within the phospholipid bilayer, several proteins can be found that fulfill different roles. From the bioelectric viewpoint, the ionic protein channels constitute an important part of the membrane, as they are gates through which ions can flow or be transported. These ionic currents form the basis of the bioelectric properties of the cells. The resting voltage of a cell $V_r$ denotes the value of the membrane voltage when the cell is in rest in its natural environment. It should be emphasised that the resting state is not a passive state, but a stable active state where the net transmembrane ionic current is zero. We define an inward or depolarising current as an inward movement of positively charged ions, causing the membrane voltage to increase, while an outward or a repolarising current is the opposite. The channels appear to have complex dynamical properties, as their conducting behaviour is dependent on membrane voltage and time. Nerve and muscle cells are so-called excitable cells, as they can respond to

an external stimulus by generating an electrical impulse, called action potential (AP), which can propagate to neighbouring cells. In muscles, the electrical waves of excitation trigger the mechanical contraction of the cell. Hence, abnormal propagation of excitation in heart tissue can result in life-threatening cardiac arrhythmias.

Note that, the transmembrane currents are not the sole currents contributing to the electrical properties of excitable cells. Ion species can be stored and released within the cell, causing fluctuations in the intracellular concentrations and hence influencing the membrane potential. The most important intracellular process is probably the so-called $Ca^{2+}$-handling, which describes the complex kinetics of $Ca^{2+}$-ions within the cell. Since in normal conditions, these processes do not influence the macroscopical electrophysiological properties of cardiac tissue, most simplified models ignore them and assume all ionic concentrations to be constants.

## 1.2 The action potential

Upon sufficiently strong electrical stimulation, the cell generates an action potential. In experiments, the stimulating current is injected into the cell by an intracellular microelectrode depolarising the membrane. Following this depolarisation, the conductance to sodium ions increases. Since the sodium concentration is greater in the extracellular space, an inward sodium current starts to depolarise the cell as well. This further depolarisation increases the sodium conductance even more and a regenerative process is triggered, leading to the rising phase or upstroke of the action potential. If the stimulating current is turned off at that time, the cell will not return to the resting state before completion of the action potential. During the depolarisation, the conductance of potassium and other ions increases as well. As the concentration of potassium ions is greater inside the cell, there is an efflux of these ions which counterbalances the inward current of calcium ions being activated at that time. After a period of constant membrane potential, the so-called plateau phase, the potassium current becomes the largest transmembrane current and repolarisation sets in, until the membrane recovers its rest potential. The duration of the whole process varies from 200 ms to 400 ms, depending on the location in the heart and on the pacing rhythm.

The action potential is an "all-or-nothing" event: for a given duration of a stimulus, a minimal amplitude is required to generate an action potential. Some time after an action potential has been generated, a so-called absolute refractory period sets in, during which a second pulse cannot be initiated. When more time has elapsed, new action potentials can be induced, but only with larger stimulus amplitudes. This time window is called the relative refractory period and continues until all ionic processes in the cell have recover their rest state.

## 1.3 The restitution properties

When the heart beats at a faster rate than normal, the duration of the action potential is adjusted to ensure an efficient pumping of the blood. If this was not the case, the ventricles would not be filled before contracting and ejecting the blood in the body. Hence, when a second action potential is initiated shortly after a first one, before the ionic processes have returned to their rest state, the action potential duration ($APD$) of the second pulse will be shorter than the first. It follows that the $APD$ is a function of the time elapsed since completion of a preceding action potential, also known as the diastolic interval ($DI$). This relationship is often referred to as $APD$ restitution.

Another fundamental property of cardiac tissue is the restitution of conduction velocity. When a sequence of action potentials propagate through tissue, the influence of the preceding excitation wave is not only reflected in a shortening of the $APD$, but also in a decrease of the conduction velocity ($CV$). The restitution of $CV$ relates the velocity of a pulse at a given site, to the preceding $DI$ at that site. Note that the restitution and refractory properties of cardiac tissue are closely related.

Experiments have shown that the restitution curves are usually monotonic increasing functions with some horizontal asymptote [Morgan et al. 1992a, Nánási et al. 1996]. In some cases however, non-monotonic curves were recorded, showing a bump at low $DI$ [Morgan et al. 1992b, Franz et al. 1983]. These curves are referred to as biphasic or supernormal restitution curves.

## 1.4 Basics of modeling excitable properties of cardiac and nerve cells

In 1952 Alan L. Hodgkin and Andrew F. Huxley published their model of the action potential in nerve cells of giant axons of the squid. They described their work by saying [Hodgkin and Huxley 1952]:

> Our object here is to find equations which describe the conductance with reasonable accuracy and are sufficiently simple for theoretical calculation of the action potential and refractory period. For sake of illustration we shall try to provide a physical basis for the equations, but must emphasise that the interpretation given is unlikely to provide a correct picture of the membrane.

In the Hodgkin-Huxley model a transmembrane current $I_x$ of a ion specie $x$ can be written as:

$$I_x = G_x \left(V_m - V_x\right) \tag{1.1}$$

where $G_x$ stands for the conductance of the channel and $V_x$ denotes the Nernst potential of the ion specie $x$. The Nernst potential can be seen as the rest potential of the membrane, in case there were only $x$-ions dissolved in the intra- and extracellular media. This approximation holds in a reasonably small area around the $x$-channel.
Experiments have shown that the conductance of channels evolves in time and is dependent of the membrane potential. Hodgkin and Huxley speculated on the ion conductance mechanism by saying that it depends on charged particles that move within the channels, allowing ions to pass or not, when occupying particular sites in the membrane. The only reason why Hodgkin and Huxley introduced those particles, was that they could associate with them a probability of being in the "open state", and hence write down dynamical equations, which could describe the properties of the channel. We will illustrate this, by discussing their model for the sodium channel.

Hodgkin and Huxley found that when a cell is clamped at a fixed membrane potential, the sodium conductance shows an initial sharp increase. They associated this rise in conductance with charged particles called m-particles and defined $m$ as being the probability of such a particle being in the open state, i.e. letting sodium ions through. If we denote by $\alpha_m(V_m)$ the voltage-dependent transfer rate coefficient for m-particles from closed to open state, and by $\beta_m(V_m)$ the voltage-dependent transfer rate coefficient for m-particles from open to closed state, then we can write the equation for the activation of sodium conductance as:

$$\frac{dm}{dt} = \alpha_m(V_m)\left(1 - m\right) - \beta_m(V_m)\, m \tag{1.2}$$

or as

$$\frac{dm}{dt} = \frac{m_\infty(V_m) - m}{\tau_m(V_m)} \tag{1.3}$$

with

$$m_\infty(V_m) = \frac{\alpha_m(V_m)}{\alpha_m(V_m) + \beta_m(V_m)}$$
$$\tau_m(V_m) = \frac{1}{\alpha_m(V_m) + \beta_m(V_m)}$$

This is an equation of the relaxation type, as at constant membrane potential $m$ relaxes to the value $m_\infty$ in a characteristical time $\tau_m$. On basis of the early part of the rise in sodium conductance, Hodgkin and Huxley supposed the sodium channel is open only if three m-particles are in the open state. Hence, the conductance is proportional to $m^3$.

The rise of sodium conductance is however not maintained and is followed by an inactivation process, which Hodgkin and Huxley modeled by introducing a single inactivating h-particle, having similar kinetics as the m-particles.

Consequently, the behaviour of the sodium conductance is modeled by:

$$G_{Na} = g_{Na}\, m^3\, h \tag{1.4}$$

where $g_{Na}$ denotes the maximal conductance. The voltage-dependent transfer rate coefficients of the m- and h-particles are experimentally determined.

At rest potential $m = 0$ and $h \sim 1$. When the cell undergoes a sufficient depolarisation, $m$ increases, while $h$ decreases. Initially, the increase in $m$ is much faster than the decrease in $h$, which results in a sharp rise of the sodium conductance, responsible for the upstroke of the action potential. After a few milliseconds, the inactivation process overtakes activation and the sodium conductance returns to 0, when $h = 0$. During the repolarisation of the membrane $m$ quickly returns to 0, before $h$ reactivates and increases to $\sim 1$, in such a way that the sodium conductance does not reactivate during repolarisation.

Denis Noble was the first to apply the formalism of Hodgkin and Huxley in a model of cardiac cells in 1962 [Noble 1962] and since then, most people have used it to describe the kinetics of transmembrane currents [Beeler and Reuter 1977, Luo and Rudy 1991, 1994, Noble et al. 1998].

## 2 The three-variable model

Currently there are two major classes of models of cardiac tissue: the low-dimensional FitzHugh-Nagumo models (FHN) [FitzHugh 1961, Nagumo et al. 1962, Aliev and Panfilov 1996] and the ionic models [Luo and Rudy 1994, Noble et al. 1998]. Ionic models provide a detailed description of the processes of activation of cardiac cells and can be used for accurate electrophysiological studies at the cellular level [Luo and Rudy 1994, Noble et al. 1998]. Unfortunately, their use for large scale simulations is seriously limited by computational constraints. On the other hand, FHN-models are efficient for large scale computational studies, but they lack electrophysiological accuracy with respect to the action potential shape, mechanisms of excitation, etc [Aliev and Panfilov 1996].

The choice of the model depends on the problem to be solved and on the computational resources available. In whole heart modeling, many problems require the use of detailed ionic

models (e.g. action of pharmacological agents on cardiac arrhythmias). Some problems can however be solved reasonably well using FHN-models. If, for example, we are interested in finding patterns of excitation in the heart we do not need all details of the generation of an action potential.

In this section we describe a 3-variable FHN-like model of the ventricular tissue we constructed in order to reproduce the basic properties of ventricular cells, such as the restitution properties, in a controllable and efficient way. Some techniques we developed during this process, formed the basis for the development of a more detailed ionic model, discussed in the next section.

### 2.1 The model equations

In 1998 a 3-variable model of the cardiac tissue was developed by Fenton and Karma [1998]. Their model consisted of three ionic currents that mimicked the basic properties of excitable tissue. We followed a similar approach and based our model on the assumption that the AP can be subdivided into three distinct parts:

1. *a fast upstroke:* this part of the action potential is mainly due to a fast inward current, which we will denote as $I_{fi}$.

2. *a plateau of constant membrane potential:* the slow in- and outward currents are being activated and have approximately the same amplitude. The sum of all slow inward currents will further be referred to as $I_{si}$, while the sum of the slow outward currents will be written as $I_{so}$.

3. *a slow repolarisation:* after some time, $I_{so}$ becomes dominant, and the cell repolarises to its rest potential.

The restitution of conduction velocity is mainly determined by the time it takes for $I_{fi}$ to recover from a previous activation, while the $APD$ restitution depends on the behaviour of the slow currents. Based on these assumptions we constructed the following model, where $u$ stands for the membrane voltage normalised to the interval $[0, 1]$, and $v$ and $w$ are two state variables:

$$\begin{cases} \frac{du}{dt} = -\frac{1}{C_m} \cdot I_{ion}(u, v, w), \\ \frac{dv}{dt} = \frac{v_\infty(u) - v}{\tau_v(u)}, \\ \frac{dw}{dt} = \frac{w_\infty(u) - w}{\tau_w(u)} \end{cases} \tag{2.5}$$

$$I_{ion}(u, v, w) = I_{fi}(u, v) + I_{si}(u, w) + I_{so}(u, w) + I_{rec}(u), \tag{2.6}$$

$$\begin{cases} I_{fi}(u, v) = g_{fi} \cdot v^2 \cdot F(u) \cdot (u - u_{Na}), \\ I_{si}(u, w) = -g_{si} \cdot \frac{w \cdot u}{\tau_{si}(w)}, \\ I_{so}(u, w) = g_{so} \cdot \frac{w \cdot u}{\tau_{so}}, \\ I_{rec}(u) = g_{rec} \cdot u \cdot (u - u_c) \cdot (u - 0.9) \end{cases} \tag{2.7}$$

We chose relaxation equations for the dynamics of the variables $v$ and $w$ using the formalism developed by Hodgkin and Huxley [1952].

## 2.2 The currents

*The fast inward current $I_{fi}$:* this current is basically the fast sodium current. In most ionic models of cardiac tissue the sodium current is described by following equation ([Luo and Rudy 1991, Noble et al. 1998]) :

$$I_{Na} = g_{Na} \cdot h \cdot j \cdot m^3 \cdot (V_m - E_{Na}) \tag{2.8}$$

with $m$ a fast activation variable, $h$ and $j$ slower in- and reactivation variables, $g_{Na}$ the conductivity of the sodium channel and $E_{Na}$ the Nernst potential of sodium ions. Since $m$ has very rapid kinetics (small characteristical time function $\tau_m$), we can eliminate this variable adiabatically, by $m = m_\infty(V_m)$. Hence, after having rescaled $V_m$, we obtain $F(u) = m_\infty^3(u)$ from equation (2.7). The variable $v$ was designed to mimic the combined properties of in- and reactivation modeled by $h$ and $j$ in ionic models. The method we used will be discussed in section 3 of this chapter.

*The slow currents and the variable $w$:* the kinetics of the slow in- and outward currents are similar and we decided to model them using a single state variable $w$. During the plateau phase of the action potential, we would like to have a constant membrane potential. Since by that time $I_{fi} = 0$ and $I_{rec}$ is negligible, we have $I_{so} + I_{si} = 0$. At the end of the plateau, the amplitude of $I_{so}$ should become larger than the amplitude of $I_{si}$.
We chose the functions $w_\infty$ and $\tau_w$ in order to have $w$ to increase during plateau towards a maximal value $w_{max}$ in a time $\tau$:

$$w_\infty(u) = w_{max} \cdot H(u - w_t) \tag{2.9}$$

$$\tau_w(u) = \tau_r \cdot (1 + \frac{\tau - \tau_r}{\tau_r} H(u - w_t)) \tag{2.10}$$

with $H$ the Heaviside step function and $w_t$ an activation threshold for the slow currents. We define the plateau as the period of time during which $w < w_p$, a threshold value smaller than $w_{max}$. Hence, as long as $w < w_p$, $|I_{so}|$ should equate $|I_{si}|$ and afterwards we should have $|I_{so}| > |I_{si}|$. In order to have this fulfilled, it suffices that:

$$\begin{cases} \tau_{si}(w \leq w_p) = \tau_{so} \\ \tau_{si}(w > w_p) > \tau_{so} \end{cases} \tag{2.11}$$

We opted for the following equation:

$$\tau_{si}(w) = \tau_{so} + g_w \cdot (w - w_p)^3 \cdot H(w - w_p) \tag{2.12}$$

*The rectifying current $I_{rec}$:* when a cell undergoes a subthreshold stimulus, i.e. a stimulus that is not strong enough to trigger an AP, the membrane potential quickly recovers its rest value. This is mainly achieved by outward rectifying currents. We achieved this by introducing a current $I_{rec}$ that is negative (outward) below a critical value $u_c$. This value is chosen to correspond with the activation threshold of the fast inward current. We chose $g_{rec}$ small, compared to the other currents, as to limit its influence on the macroscopic properties of the AP. Moreover, the factor $(u-0.9)$ prevents a jump in membrane potential whenever a pulse is applied during the plateau phase.

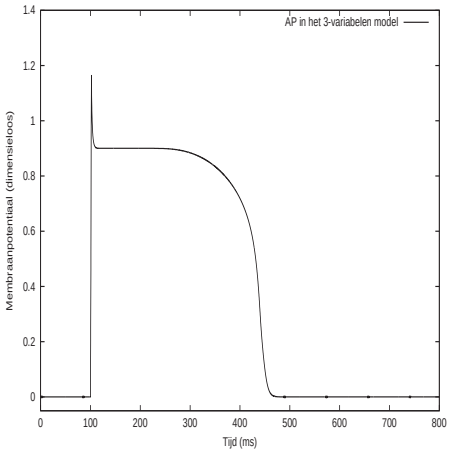


Figure I.1: Action potential.

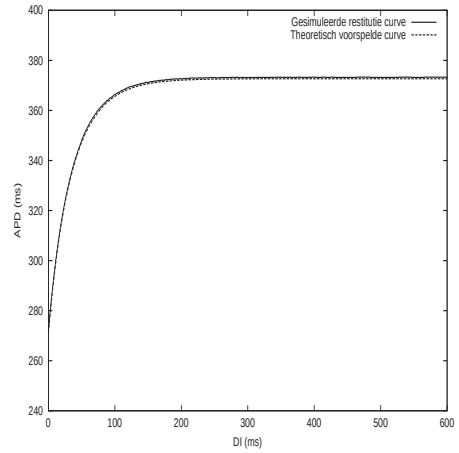


Figure I.2: Comparison of restitution curves.

### 2.3 The restitution properties

The simplicity of the model permits us to derive the restitution properties analytically. The length of the plateau phase is a measure for the $APD$. During plateau $u = 0.9$ en hence we can solve the equation for $w$ :

$$w(t) = w_{max} - (w_{max} - w(0)) \cdot e^{-\frac{t}{\tau}} \tag{2.13}$$

The plateau finishes when $w(t) = w_p$. This yields:

$$APD(w(0)) = \tau \cdot \ln \frac{w_{max} - w(0)}{w_{max} - w_p} + T_{rep} \tag{2.14}$$

where $T_{rep}$ denotes the repolarisation duration. The $APD$ of a free pulse is thus given by:

$$APD(\infty) = \tau \cdot \ln \frac{w_{max}}{w_{max} - w_p} + T_{rep} \tag{2.15}$$

In order to obtain the restitution of $APD$ in function of $DI$, we need to find a relation between $w(0)$ and $DI$. The diastolic interval is the time that $w$ needs to evolve from $w_b$ to $w(0)$, where $w_b$ stands for the value of $w$ when the membrane finishes repolarisation ($u = 0$). Since $w_\infty(0) = 0$ we obtain:

$$w(0) = w_b \cdot e^{-\frac{DI}{\tau_r}} \tag{2.16}$$

which yields the $APD$ restitution:

$$APD(DI) = \tau \cdot \ln \frac{w_{max} - w_b \cdot e^{-\frac{DI}{\tau_r}}}{w_{max} - w_p} + T_{rep} \tag{2.17}$$

Figures I.1 and I.2 show an action potential and a comparison between theoretically calculated and simulated restitution curves, using the parameter values of Table I.1. For these values we found $T_{rep} = 254.4$ ms and $w_b = 0.319$.

| | | | |
|---|---|---|---|
| $u_{Na}$ | 1.3 | $\tau$ (ms) | 265.0 |
| $g_{fi}$ | 16.0 | $\tau_r$ (ms) | 40.0 |
| $g_{rec}$ | 0.8 | $w_p$ | 0.36 |
| $g_w$ | 0.8 | $w_{max}$ | 1.0 |
| $g_{so}$ | 1.0 | $w_t$ | 0.3 |
| $g_{si}$ | 1.0 | $u_c$ | 0.3 |

Table I.1: Parameters of the 3-variable model (dimensionless, unless indicated otherwise)

## 3 The rPB model [Bernus et al. 2002c]

The history of modeling biological excitable media using detailed descriptions of the cellular processes started 50 years ago with the Hodgkin-Huxley model of the giant squid axon, as discussed in section 1.4. The first model of cardiac tissue (Purkinje fibers) was proposed by Noble [1962] and consisted of 4 variables. During the following decades the experimental techniques for studying the properties of the cell membrane were improved continuously, leading to new cardiac tissue models of increasing accuracy, e.g., the phase-2 Luo-Rudy model of a single guinea pig ventricular cell [Luo and Rudy 1994], which has 12 variables and the models developed by Noble et al. consisting of 40 to 60 equations, see for example [Noble et al. 1998]. Recently, comprehensive models have been proposed to account for specific properties of human cardiac tissue: Nygren et al. [1998] and Courtemanche et al. [1998] developed models of single human atrial cells, whereas Priebe and Breuckelmann [1998] proposed a model of a single human ventricular cell.

The PB model is based on the phase-2 LR model. However, five major ionic currents, including the fast and slow components of the delayed rectifier potassium current, the L-type calcium current, the transient outward current and the inward rectifier potassium current, are based on experimental data obtained on human myocytes. In addition parameters of the $[Ca^{2+}]_i$ handling were changed in such a way that simulated transients are comparable to observed experimental data on human myocytes [Beuckelmann et al. 1992]. The remaining currents have been adjusted from the LR model, with their amplitude scaled to fit human cell data. Priebe and Beuckelmann developed their model in order to compare the electrophysiological properties of failing and non-failing ventricular myocytes. It can be used for accurate simulations of the ionic currents and concentrations in a single cell during electrical activity. Our objective, however, is to simulate reentrant sources of arrhythmias in 2D and 3D, which are believed to underlie most ventricular tachycardias and ventricular fibrillation [Gray et al. 1998, Jalife et al. 1998b, Witkowsky et al. 1998]. Although the PB model is based on experimental measurements in human heart tissue, we refrained from using it for the study of reentrant arrhythmias for several reasons. First, the complexity and the high number of variables make the PB model inefficient for extensive computer simulations of large pieces of tissue. Secondly, the PB model is a second-generation model, in which, besides membrane potential and gating variables, ion concentrations vary in time. Second-generation models, made up of ordinary differential equations describing the time-dependence of membrane potential, gating variables, and ion concentrations, are inherently unstable, showing complications involving long-term drifts of ion concentrations and degeneracy of equilibria, as recently emphasised by both Arce et al. [2000] and Endresen and Skarland [2000].

Our main aim was to develop a model of an intermediate class, between the comprehensive ionic models and the FHN-models of cardiac tissue. The model should be computationally

efficient, less complex than the second-generation ionic models and free of their inherent instabilities. At the same time the model should retain important properties of human ventricular tissue such as restitution properties, AP shape, and change of AP shape under variation of major ionic currents. This aim was achieved by reformulating the PB model as a six-variable model, which keeps the major ionic currents but discards some single cell processes that do not substantially affect the desired tissue properties. It should be noted that the reformulation procedure does not depend on the PB model and can be applied to any ionic model.

### 3.1 Reduction of the Priebe-Beuckelmann model

The several stages in the reformulation of the PB model are discussed for each ionic current of the reduced model. We also pay attention to the numerical accuracy and stability of the reduced model and we discuss numerical schemes used in the simulations. Throughout this section time is expressed in ms, membrane potential in mV, ion concentrations in mM, rate constants in $ms^{-1}$, current in pA/pF, and conductance in nS/pF. Single cell membrane capacitance, cell length, and cell diameter are 153.4 pF, 100 $\mu$m, and 22 $\mu$m, respectively (same as in the original PB model). $[\cdot]_i$ denotes an intracellular concentration, while an extracellular concentration is written as $[\cdot]_e$.

*Intracellular ion concentrations*

The intracellular ion concentration handling in second-generation models can be a source of instabilities [Arce et al. 2000, Endresen and Skarland 2000]. This also holds for the PB model, which shows long term drifts of $[K^+]_i$ and $[Na^+]_i$ when paced at different frequencies (see section 3.6). Therefore, noting that the variations of $[K^+]_i$ and $[Na^+]_i$ over the course of an AP are extremely small, we set $[K^+]_i$ and $[Na^+]_i$ to constant values of 140 and 10 mM, respectively, i.e., the initial values in the PB model. In contrast, the intracellular calcium concentration undergoes substantial changes during the action potential. We do not intend to study details of $Ca^{2+}$ dynamics, but are mainly interested in overall properties of the L-type $Ca^{2+}$ current and its influence on the AP shape and restitution properties of cardiac tissue. Moreover, in the Priebe-Beuckelmann model the calcium subsystem is represented by a model that mimics $Ca^{2+}$-induced $Ca^{2+}$ release (CICR) as an all-or-none event and reproduces $Ca^{2+}$ transients with realistic amplitudes, but is phenomenological in construction and is not sufficient to accommodate predictions of intracellular $Ca^{2+}$ dynamics under more complex experimental conditions. Therefore we decided to assign a constant value of 400 nM to the free intracellular calcium concentration appearing in the calcium current equations of the original PB model, as an average of its value during the course of an action potential. It should be noted that we do not claim that the intracellular calcium handling is irrelevant for cardiac activity, but that the simplified equations for the L-type calcium current listed below are sufficient for a correct representation of AP shape and restitution of action potential duration.

*Ionic currents*

*Fast sodium current ($I_{Na}$):* In the PB model, the kinetic behavior of $I_{Na}$ is described by a very fast activation variable $m$ and fast and slow inactivation variables $h$ and $j$,

respectively:

$$I^o_{Na} = g_{Na} \cdot m^3 \cdot h \cdot j \cdot (V_m - E_{Na}) \tag{3.18}$$

in which the superscript 'o' denotes an equation used in the original PB model, $g_{Na}$ maximum sodium conductance, and $E_{Na}$ Nernst potential (similar notations for the other currents). The activation of $I_{Na}$ is the fastest process during an AP. Hence it is tempting to eliminate $m$ adiabatically. However, such reduction induces an unrealistically steep upstroke of the AP and drastically decreases the numerical accuracy of the model (see below). Therefore, we refrained from changing $I_{Na}$ activation. Note that in the 3-variable model, we did eliminate $m$ adiabatically, since the lower number of variables permitted us to integrate the equations at smaller time and space steps, compensating for the computational time lost by the decreased accuracy.

Inactivation of $I^o_{Na}$ is modeled by the product of two variables $h$ and $j$. For our purposes, a single variable $v$ of the Hodgkin-Huxley type suffices. Retaining the quadratic dependence of sodium current inactivation, we obtain:

$$I_{Na} = g_{Na} \cdot m^3 \cdot v^2 \cdot (V_m - E_{Na}) \tag{3.19}$$

The time course of $v$ is determined by:

$$\frac{dv}{dt} = \frac{v_\infty(V_m) - v}{\tau_v(V_m)} \tag{3.20}$$

The constraint we put on $v$ is that the behaviour of $I^o_{Na}$ under a fixed membrane potential (voltage clamp) should be well reproduced by the above formulated $I_{Na}$. Thus, our aim is to obtain a reasonable approximation of $I^o_{Na}(t)$ at all times for each clamped potential. The kinetics of the gating variable $v$ can be determined in two steps. First, we determine $v_\infty(V_m)$, which is readily found from (3.18) and (3.19) :

$$v_\infty(V_m) = \sqrt{h_\infty(V_m) \cdot j_\infty(V_m)} \tag{3.21}$$

Next, we determine $\tau_v(V_m)$ by simulating a voltage clamp experiment and investigating the time course of $I_{Na}$ at fixed membrane potentials. To obtain a reasonable fit for all $t$ we used a least-squares method by minimizing a function $\Delta_{Na}(\tau_v(V_m))$ given by:

$$\Delta_{Na}(\tau_v(V_m)) = \int_0^{T_e} (I^o_{Na}(t) - I_{Na}(t))^2 \, dt \tag{3.22}$$

Since the sodium current is a rapid current we performed a voltage clamp during $T_e =$ 100 ms for 10,000 equidistant values of membrane potential within the interval [-100 mV, 90 mV]. The obtained functions, $v_\infty(V_m)$ and $\tau_v(V_m)$, are shown in Fig. I.3 A and B, respectively. In subsequent simulations we used values directly tabulated from the voltage clamp simulations, but they can be well approximated by the functions listed in section. Figure I.3, C and D, shows simulated voltage clamp records of the original and reformulated $I_{Na}$, illustrating that at both test potentials the two closely match, both in amplitude and time. Similar results were obtained at other test potentials between $-70$ and $+50$ mV (data not shown).

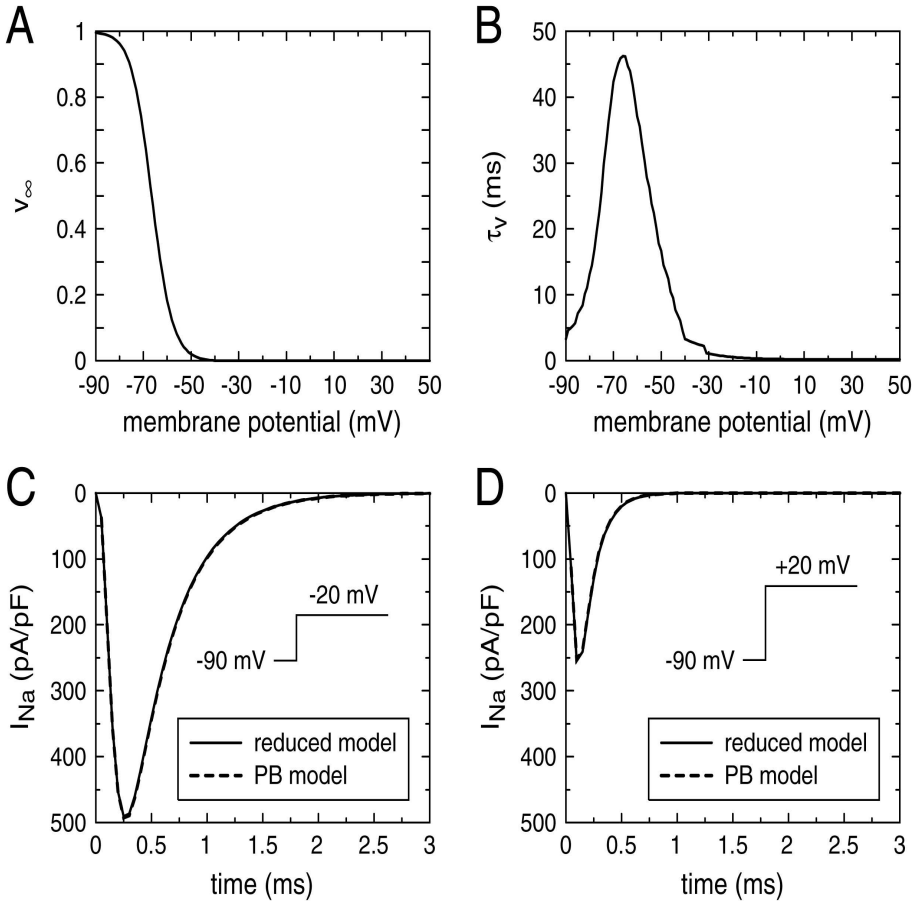


Figure I.3: (A) Steady state value, $v_\infty$, and (B) time constant, $\tau_v$, of the inactivation gating variable $v$ of the fast sodium current ($I_{Na}$) in the reformulated Priebe-Beuckelmann model. (C, D) Comparison of fast sodium current ($I_{Na}$) in the reduced and the original Priebe-Beuckelmann model. Activation of $I_{Na}$ in response to a voltage clamp step from a holding potential of $-90$ mV to a test potential of (C) $-20$ and (D) $+20$ mV.

*Calcium current ($I_{Ca}$):* Priebe and Beuckelmann modeled $I_{Ca}$ using Hodgkin-Huxley type activation and inactivation variables, $d$ and $f$. In addition, they introduced $[\mathrm{Ca}^{2+}]_i$-dependent inactivation by a $V_m$-independent factor $f_{Ca}$:

$$I^o_{Ca} = g_{Ca} \cdot d \cdot f \cdot f_{Ca}([Ca^{2+}]_i) \cdot (V_m - E_{Ca}), \tag{3.23}$$

$$f_{Ca}([Ca^{2+}]_i) = \frac{1}{1 + \frac{[Ca^{2+}]_i}{0.0006}} \tag{3.24}$$

The activation of $I_{Ca}$ is a fast process. Hence, we eliminated $d$ adiabatically and obtained:

$$I_{Ca} = g_{Ca} \cdot d_\infty \cdot f \cdot f_{Ca} \cdot (V_m - E_{Ca}) \tag{3.25}$$

in which $f_{Ca}$ has a constant value of 0.6, since $[\mathrm{Ca}^{2+}]_i$ was set to 400 nM in the reduced model, as set out above.

*Transient outward current ($I_{to}$):* The equation that Priebe and Beuckelmann used for the transient outward current is:

$$I^o_{to} = g_{to} \cdot r \cdot to \cdot (V_m - E_{to}) \tag{3.26}$$

in which $r$ is a very fast activation variable and $to$ is an inactivation variable. Eliminating $r$ adiabatically yields our reduced current:

$$I_{to} = g_{to} \cdot r_\infty \cdot to \cdot (V_m - E_{to}) \tag{3.27}$$

where $g_{to}$ was increased by 30% (see below).

*Delayed rectifier potassium current ($I_K$):* In the PB model, $I_K$ consists of two components, $I_{Kr}$ and $I_{Ks}$, each with a single activation variable, $X_r$ and $X_s$, respectively:

$$I^o_K = I_{Kr} + I_{Ks} = g_{Kr} \cdot X_r \cdot \frac{1}{1 + exp[(V_m + 26)/23]} \cdot (V_m - E_{Kr}) + g_{Ks} \cdot X_s^2 \cdot (V_m - E_{Ks}) \tag{3.28}$$

Using the same approach as for $I_{Na}$, but with $T_e$ set to 300 ms, we combined $I_{Kr}$ and $I_{Ks}$ into a single $I_K$ with a single activation variable $X$ and reversal potential $E_K$, for given $g_{Kr}$ and $g_{Ks}$:

$$I_K = g_K \cdot X^2 \cdot (V_m - E_K) \tag{3.29}$$

For the parameter values of the original PB model the resulting $X_\infty$ and $\tau_X$ are plotted in Fig. I.4, A and B, respectively. Continuous approximations are listed in Appendix A. The value of $g_K$ was determined by the constraint that $X_\infty$ should range between 0 and 1. In order to obtain good restitution of $APD$ we increased $\tau_X$ slightly around the resting potential by adding a sigmoidal function $\tau'_X$ (see Appendix A). This minor change had no marked influence on the shape of the AP or on the time course of $I_K$ (not shown). Note that using a single $I_K$ current does not prevent our model to be applied for, e.g., studies of drug action on the separate rapid and slow components of the potassium current. Therefore, one should just reapply the above fitting procedure with different initial values of $g_{Kr}$ and $g_{Ks}$ (see section 3.5). Figure I.4, C and D, shows simulated voltage clamp records of the original (sum of $I_{Kr}$ and $I_{Ks}$) and reformulated $I_K$. In the reformulated model $I_K$ shows slightly faster kinetics than in the original PB model, resulting in a somewhat larger current at the end of the 300-ms pulse.

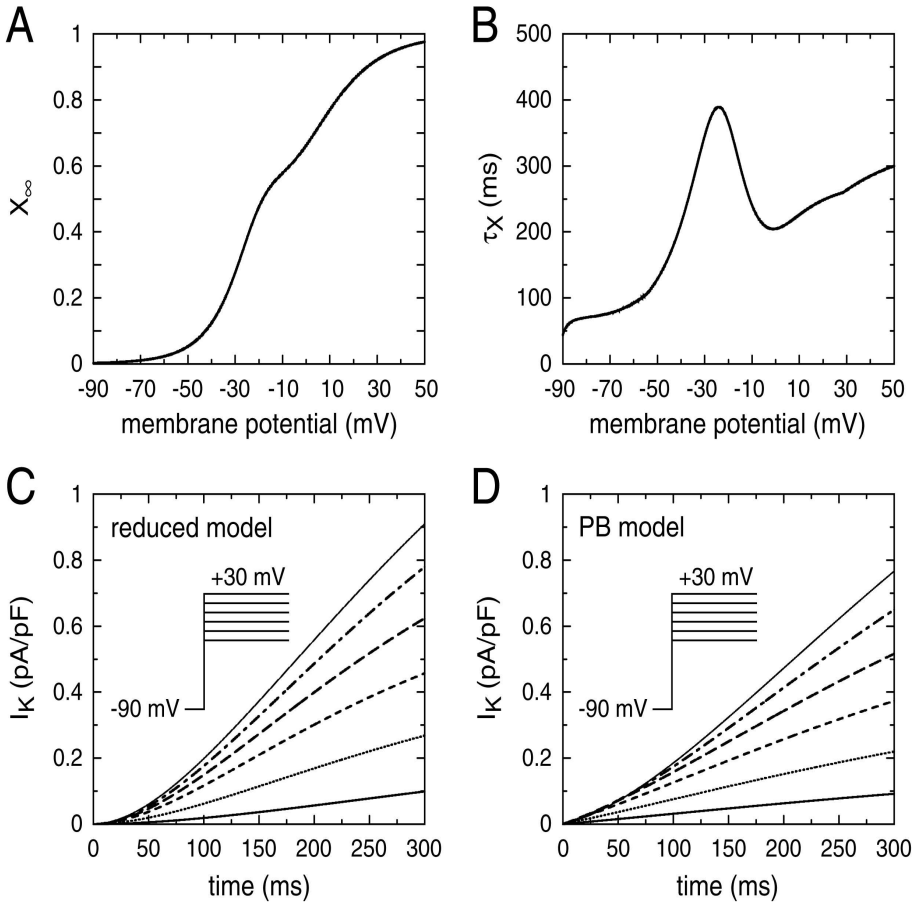


Figure I.4: (A) Steady state value, $X_\infty$, and (B) time constant, $\tau_X$, of the activation variable $X$ of the delayed rectifier potassium current ($I_K$) in the reformulated Priebe-Beuckelmann model. (C, D) Comparison of delayed rectifier potassium current ($I_K$) in the reduced and the original Priebe-Beuckelmann model. Activation of $I_K$ in response to a voltage clamp step from a holding potential of 90 mV to a series of test potentials of 20, -10, 0, +10, +20, and + 30 mV. (C) Reformulated model. (D) Original Priebe-Beuckelmann model.

*Time-independent currents:* For each of the time-independent currents, except $I_{K1}$, we used the original equations from the PB model, which appear in Appendix A. For $I_{K1}$, we used the original equations, but increased its conductance $g_{K1}$ by 56% (see below).

*Parameter values:* The difference between the parameter values of the original PB model and our reduced model have all been listed above. We did not change any of the other parameters. The values of all parameters of the two models are compared in Appendix Table A.1.

### 3.2 Numerical approach and numerical accuracy

The propagation of an AP is modeled by the (one-dimensional) cable equation:

$$C_m \frac{\partial V_m}{\partial t} = -I_{ion} + \frac{1}{S \cdot \rho} \frac{\partial^2 V_m}{\partial x^2} \tag{3.30}$$

where $C_m$ denotes cell capacitance per surface unit, $S$ surface to volume ratio, and $\rho$ cellular resistivity. $I_{ion}$ is the net membrane current, which consists of the aforementioned $I_{Na}$, $I_{Ca}$, $I_{to}$, $I_K$, and $I_{K1}$ as well as background sodium and calcium currents ($I_{Na,b}$ and $I_{Ca,b}$, respectively) and the net currents generated by the electrogenic sodium-potassium pump and sodium-calcium exchanger ($I_{NaK}$ and $I_{NaCa}$, respectively). For $C_m = 2.0$ $\mu$F/cm$^2$ and $S = 0.2$ $\mu$m$^{-1}$ (same value as in the PB model) and $\rho = 180$ $\Omega$cm we obtained a plane wave conduction velocity of 70 cm/s. The value was the same as that reported by Jongsma and Wilders [2000] for longitudinal $CV$ in a linear cable of PB model cells at $\rho = 181$ $\Omega$cm. We used Crank-Nicholson as well as forward Euler methods to integrate (3.30). The relaxation equations for the gating variables were integrated using a technique presented by Rush and Larsen [1978] (see also Appendix B). All simulations were coded in C++ and ran either on a PC with an Intel Pentium III 500 Mhz CPU or on a Compaq AlphaServer DS20E with a 666 Mhz Alpha 21264 CPU.

We tested the numerical accuracy of our model in a cable by changing the time and space step and measuring the $CV$ of a propagating AP. We used a Crank-Nicholson method as well as a forward Euler method (see Appendix B), yielding similar results (not shown). Table I.2 shows the results we obtained: in both the original and reduced model an increase of the time step from 0.01 to 0.02 ms caused a change of less than 1%, whereas an increase in $\Delta x$ from 0.01 to 0.03 cm reduced $CV$ by 10% (comparable to results obtained by Qu et al. [Qu et al. 1999] ). The bottom rows of Table I.2 show the accuracy of the reduced model upon adiabatical elimination of $m$. The $> 50\%$ decrease in $CV$ that occurred when $\Delta x$ was increased from 0.01 to 0.03 cm readily explains why we refrained from eliminating $m$ adiabatically.

### 3.3 AP and main ionic currents

Figure I.5 shows a steady-state AP and the main (gated) ionic currents in the reduced and the original PB model (solid and dotted lines, respectively), obtained by pacing a single cell at 1 Hz with a 2-ms, 3-nA depolarising current. The AP in the reduced model is almost identical to the AP in the original model (Fig. I.5A, Table I.3). We observed an almost perfect match between $I_{Na}$ in the reduced and original model (Fig. I.5B). Peak $I_{Ca}$ has increased by 40%, but the global time course is preserved (Fig. I.5C). The time course and amplitude of $I_K$ are similar in the reduced and original model (Fig. I.5D). In the reduced model, $I_{to}$ shows

| | Conduction velocity, cm/s | | | | |
|---|---|---|---|---|---|
| $\Delta x =$ | 0.10 mm | 0.15 mm | 0.20 mm | 0.25 mm | 0.25 mm |
| PB model | | | | | |
| $\Delta t = 0.01$ ms | 69.4 | 67.9 | 65.8 | 63.4 | 60.8 |
| $\Delta t = 0.02$ ms | 69.5 | 68.1 | 65.8 | 63.4 | 61.0 |
| Reduced model | | | | | |
| $\Delta t = 0.01$ ms | 69.9 | 68.1 | 66.0 | 63.5 | 60.5 |
| $\Delta t = 0.02$ ms | 70.4 | 68.2 | 65.8 | 63.5 | 60.3 |
| Reduced model with $m = m_\infty$ | | | | | |
| $\Delta t = 0.01$ ms | 57.1 | 46.3 | 38.2 | 31.7 | 26.6 |
| $\Delta t = 0.02$ ms | 57.4 | 46.6 | 38.1 | 31.7 | 26.6 |

Table I.2: Numerical accuracy of conduction velocity for different integration time and space steps

| | PB model | Reduced model |
|---|---|---|
| $V_r$, mV | −91.2 | −90.2 |
| Activation threshold, mV | −60.8 | −60.2 |
| $\frac{dV_m}{dt}(max)$, V/s | 385.2 | 386.2 |
| $APD$, ms | 356.9 | 357.2 |

Table I.3: Action potential parameters for the PB model and the reduced model

a significantly larger peak and an earlier inactivation compared to the original model (Fig. I.5E). However, the net charge carried by this current in the reduced model has only increased by about 40% compared to the original model (not shown). Except for the large amplitude of $I_{to}$ (see below), the AP and ionic currents in the reduced model agree well with those in the PB model. Moreover, we investigated the relative influence of each gated current on the AP shape by gradually decreasing the conductances and obtained results that closely match those obtained by Priebe and Breuckelmann [1998] for the full model (not shown).

### 3.4 Restitution of $APD$ and $CV$

Restitution of $APD$ was obtained using an S1-S2 protocol on a single cell, consisting of 10 S1 stimuli at 1 Hz frequency and an extra stimulus delivered at some diastolic interval ($DI$) after the last S1 AP. The restitution curve is then obtained by plotting $APD$ of the extra AP versus $DI$. Stimulus current lasted 2 ms and its strength was two times threshold. The $APD$ was defined using a threshold potential of 76 mV, corresponding to 90% repolarisation. Restitution of $CV$ was measured by periodically pacing one end of a one-dimensional cable of cells. The $CV$ was measured at a point in the middle and by increasing the pacing rate we were able to measure $CV$ at various diastolic intervals. Simulations were performed using Crank-Nicholson integration in a cable of 4 cm length with with $\Delta x$= 0.1 mm and $\Delta t = 0.02$ ms.

The $APD$ restitution is known to play a crucial role in the formation and stability of reentrant wave patterns like spiral waves [Courtemanche et al. 1993, Glass 1996, Qu et al. 1999]. Figure I.6A shows the $APD$ restitution curves of the reduced model and the original

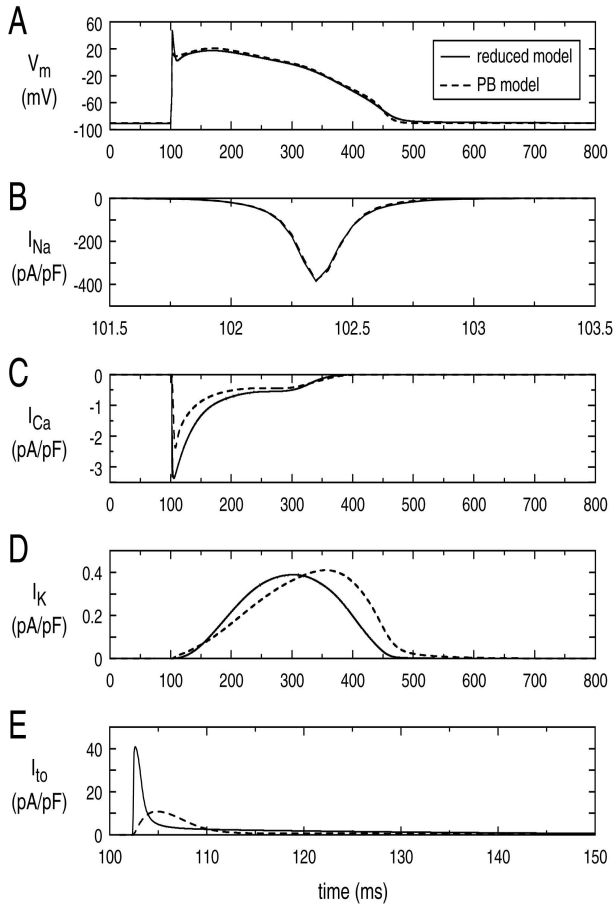


Figure I.5: Action potential and associated membrane currents in the reformulated PB model (solid lines) and in the original PB model (dashed lines). Action potential shown is the 5th from a cell paced at 1 Hz with a 2-ms stimulus current of two times threshold. (A) Membrane potential ($V_m$). (B) Fast sodium current ($I_{Na}$). (C) L-type calcium current ($I_{Ca}$). (D) Delayed rectifier potassium current ($I_K$). (E) Transient outward current ($I_{to}$).

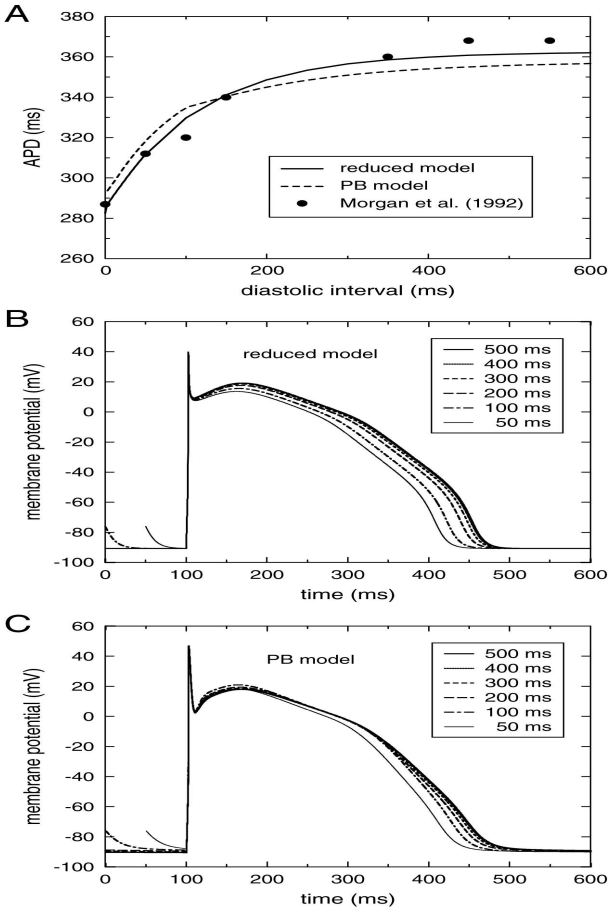


Figure I.6: Restitution of action potential duration. (A) $APD$ restitution curves in the reformulated model and the original Priebe- Beuckelmann model, and experimental data obtained by Morgan et al. [Morgan et al. 1992a]. (B, C) Dependence of action potential shape on diastolic interval ($DI$). $DI$ was gradually decreased from 500 to 50 ms, as indicated. (B) Reformulated model. (C) Original Priebe-Beuckelmann model.

model as well as the experimental data obtained from human right ventricle by Morgan et al. [Morgan et al. 1992a]. The two model curves are quite similar, the reduced model matching the experimental data even slightly better than the original model. Figure I.6, B and C, illustrates the changes in shape of the AP with decreasing $DI$. At short $DI$ we observed a lowering of the plateau in both models. We conclude that the restitution properties of the PB model are well reproduced in our reduced model, both with respect to AP shape and duration, and that the reformulated model nicely reproduces available experimental data.

The activation properties of the original PB model and our reduced model are compared in Fig. I.7. Figure I.7A shows the stimulus strength-duration curves of both models, whereas Fig. I.7B shows the $CV$ restitution curves. The stimulus strength-duration curve relates the amplitude of a stimulating current to the time it should be applied in order to trigger an AP. Hence, it is a measure for the excitability of the cell. The decrease in $CV$ with decreasing $DI$ is due to the decreasing amount of $I_{Na}$ that is available for (re)activation. In the full model this amount is determined by the fast and slow inactivation variables $h$ and $j$, whereas in our model it is solely determined by $v$. The curves behave similarly at long $DI$, but at

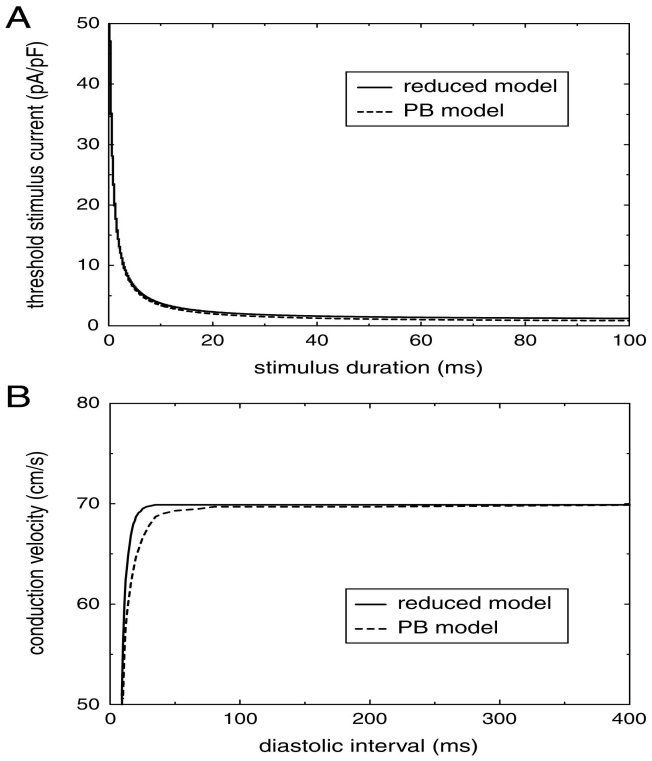


Figure I.7: Activation properties of the reformulated model and original Priebe-Beuckelmann model. (A) Stimulus strength-duration curves. (B) Conduction velocity ($CV$) restitution curves.

short $DI$ the reduced model shows a slightly steeper dependence than the original model, caused mainly by $\tau_v$ being slightly too small. We did not try to get a perfect match with the $CV$ restitution curve in the full model, because there exist no reliable experimental data on $CV$ restitution in normal human ventricular tissue. Note, however, that the $CV$ restitution properties can easily be adapted to new experimental data by minor modifications of $\tau_v(V_m)$.

### 3.5 Action potential heterogeneity

The transmural heterogeneity of the ventricular AP that has been observed in animal and human myocardium [Antzelevitch et al. 2001, Li et al. 1998, Liu et al. 1993, Main et al. 1998] plays an important role in the ECG transcription, especially with respect to the J and T wave. As we intend to investigate and simulate ECGs of ventricular arrhythmias it is important to take this heterogeneity into account. Three main AP morphologies are observed through the ventricular wall: the epicardial AP with the typical notch and spike-and-dome shape, the M cell AP with less pronounced notch and prolonged repolarisation phase, and the endocardial AP with the more triangular shape [Antzelevitch et al. 2001, Li et al. 1998, Liu et al. 1993]. The prolonged $APD$ of the M cells is associated with a reduced $I_{Ks}$ [Liu et al. 1993], while the change from a spike-and-dome to a more triangular shape is due to a transmural gradient in amplitude and kinetics of $I_{to}$. From epicardium to endocardium, $I_{to}$ shows a decrease in amplitude, a negative shift in half-inactivation voltage, and an increase in reactivation time [Li et al. 1998]. As a test on the role of selected ionic currents, we investigated how the reformulated model could reproduce the observed AP heterogeneity. The full PB model and

| | Epicardial Cells | M Cells | Endocardial Cells |
|---|---|---|---|
| $1/p$ | 1 | 1.7 | 2.8 |
| $V_{shift}$, mV | 0 | -4 | -12 |
| $g_{to}$, nS/pF | 0.4 | 0.35 | 0.13 |
| $g_K$, nS/pF | 0.019 | 0.013 | 0.019 |

Table I.4: Parameter values of the reformulated PB-model for the three ventricular cell types

our reduced version thereof show a clear notch and spike-and-dome morphology and were assumed to resemble an epicardial cell. To create an M cell model, we changed both $I_{to}$ and $I_K$ (through its slow component $I_{Ks}$). To create an endocardial cell model, we only made changes to $I_{to}$.

The amplitude of $I_{to}$ was changed by altering $g_{to}$. We increased the inactivation time of $I_{to}$ by multiplying $\alpha_{to}(V_m)$ and $\beta_{to}(V_m)$ with a constant factor $p < 1$, thus increasing $\tau_{to}$ while preserving the function $to_\infty$. The half-inactivation voltage was changed through a shift in the gating functions of $to$ by $V_{shift}$. The resulting equations for $\alpha_{to}(V_m)$ and $\beta_{to}(V_m)$ are listed in Appendix A. In order to prolong the $APD$ of the M cells, we decreased $g_{Ks}$ by 50% in the original PB model and performed new voltage clamp simulations on the sum of $I_{Kr}$ and $I_{Ks}$ to obtain $X_\infty$, $\tau_X$, and $g_K$ for the M cell. The thus obtained tabulated values of $X_\infty$ and $\tau_X$ are well approximated by the functions listed in Appendix A. The new $g_K$ was found to equal 0.013 nS/pF. The AP heterogeneity was obtained by using the parameter values listed in Table I.4. Note that all relative changes are well within the experimentally observed range [Li et al. 1998]. The simulated APs for epicardium, M cells and endocardium are shown in Fig. I.8, A−C, and have a duration of 360, 362, and 400 ms, respectively, and are similar to the APs observed experimentally [Antzelevitch et al. 2001, Li et al. 1998]. Figure I.8D shows the $APD$ restitution curves for the different cell types. As reported by Antzelevitch et al. [Antzelevitch et al. 2001], the restitution curves for epicardium and endocardium almost coincide, whereas the restitution curve for the M cells is considerably steeper.

### 3.6 Stability, ionic drift and computational efficiency

We compared the speed of computations by pacing a cell at 1 Hz during 1000 s model time. All computations were performed on the 666 Mhz Alpha 21264 CPU of a Compaq AlphaServer DS20E using Euler type integration with a time step of 10 $\mu$s. For the original model the simulation took 386.5 s of computer time,whereas for the reduced model the simulation finished in 79.5 s. During this simulation, the original model shows a drift in both $[Na^+]_i$ and $[K^+]_i$. Over 1000 s model time, mean $[Na^+]_i$ decreased from 10 to 8.1 mM (Fig. I.9B), while mean $[K^+]_i$ decreased non-monotonically from 140 to 139.5 mM (Fig. I.9C). As a consequence the PB model did not reach a steady state and after 1000 s model time the $APD$ ran up to 425 ms (Fig. I.9A).

Since $[Na^+]_i$ and $[K^+]_i$ change very little over the course of one AP, it is tempting to eliminate their drifts by putting them to a constant value. If the above simulation of 1000 s of model time is repeated with $[Na^+]_i$ and $[K^+]_i$ set to constant values of 140 and 10 mM, respectively, the PB model does reach a steady state with an $APD$ of 360 ms and the simulation takes 305 s of computer time (not shown). However, if the cycle length is abruptly changed, e.g., to 2 Hz, a very slow adaptation of $[Ca^{2+}]_i$ is observed (Fig. I.10B) and it takes $> 150$ s of model time for the cell to reach a new steady state (Fig. I.10A), where $APD$ has an unrealistic value of over 350 ms. They were the main reasons why we refrained from

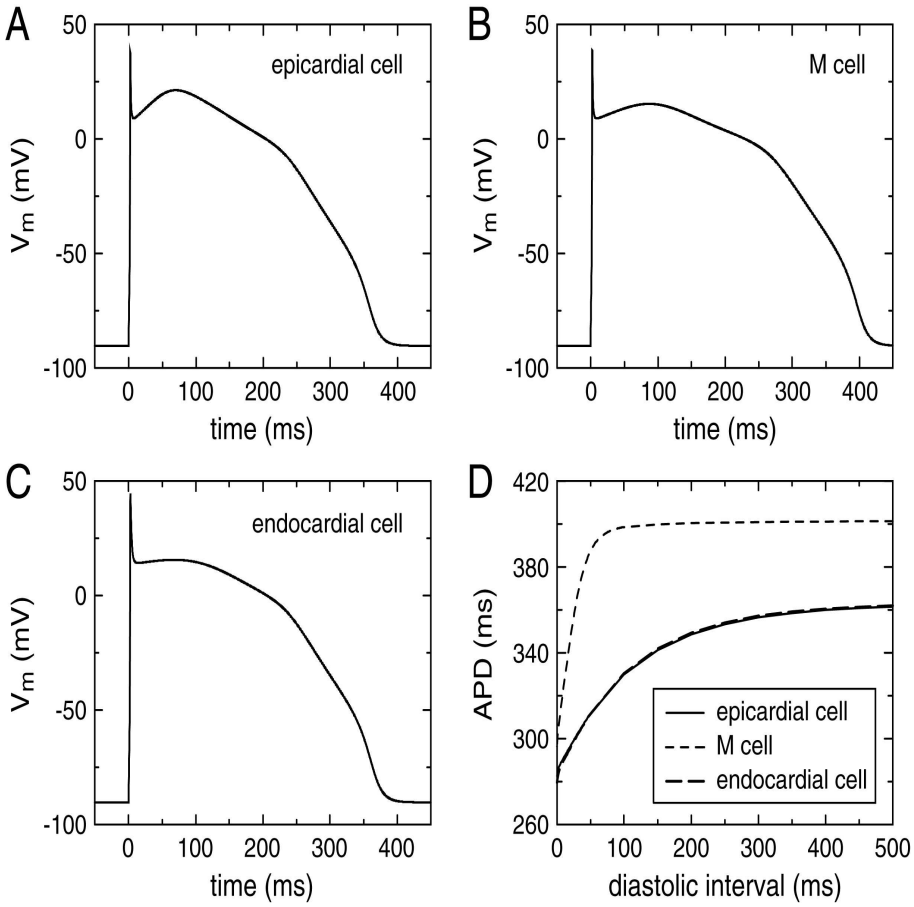


Figure I.8: Action potential and $APD$ restitution in three different configurations of the reformulated model, representing the different cell types that are present in the ventricular wall. Action potential of (A) an epicardial cell, (B) a midmyocardial cell (M cell), and (C) an endocardial cell. (D) $APD$ restitution curves for each of the cell types.

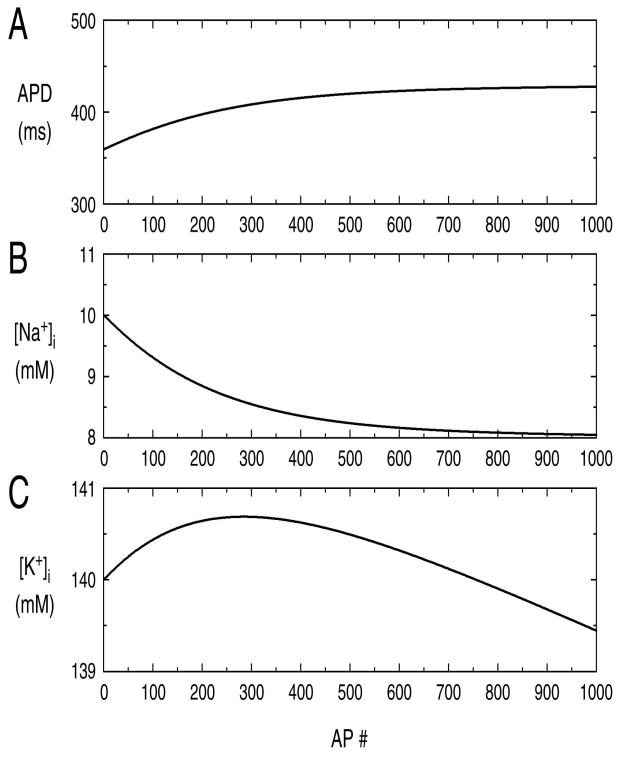


Figure I.9: Beat-to-beat changes in (A) action potential duration ($APD$), (B) mean intracellular sodium concentration ($[Na^+]_i$), and (C) mean intracellular potassium concentration ($[K^+]_i$) in the original Priebe-Beuckelmann model paced at 1 Hz.

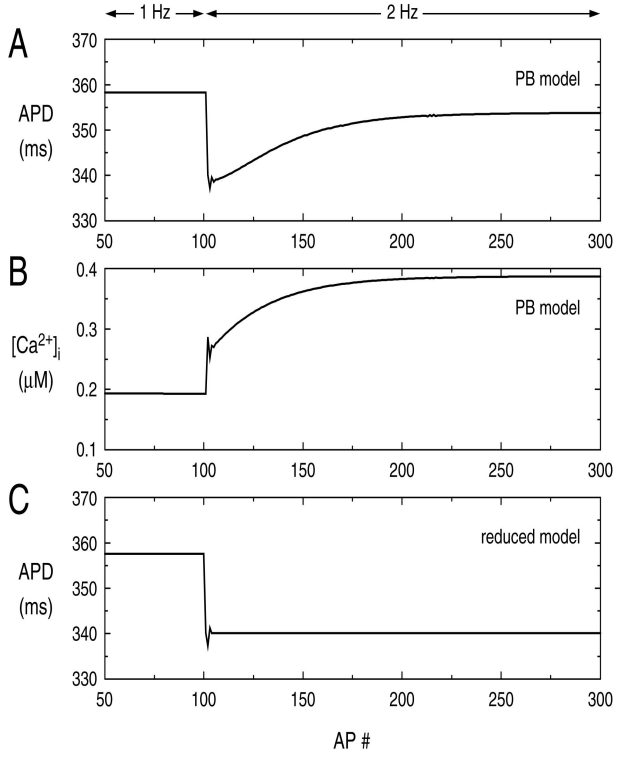


Figure I.10: Beat-to-beat changes in (A) action potential duration ($APD$) and (B) mean intracellular calcium concentration ($[Ca^{2+}]_i$) in the original Priebe-Beuckelmann model ( $[Na^+]_i$ and $[K^+]_i$ fixed at 10 and 140 mM, respectively) upon a step increase in stimulation frequency from 1 to 2 Hz at time 100 s. (C) Beat-to-beat changes in $APD$ in the reformulated model using the same stimulation protocol.

using the original PB model, even with $[Na^+]_i$ and $[K^+]_i$ set to constant values, for extensive simulations of arrhythmias. In those cases, it would take a long time before all transient drifts would have disappeared. In the reformulated model the cell adapts after a few beats to a given cycle length, even after an abrupt change (Fig. I.10C), just like real cells. Given the increase in computational speed obtained with the reformulated model an increase by a factor of 4.9 compared to the full PB model and a factor of 3.8 compared to the PB model with constant $[Na^+]_i$ and $[K^+]_i$ as well as the much faster and more realistic adaptation to changes in cycle length, it is clear that the use of the reduced model saves a huge amount of computational time, when investigating reentrant arrhythmias. Also, with the number of model variables reduced from 15 to 6, the demand for computer memory is reduced by a factor of 2.5.

## 4 The biphasic rPB model [Bernus et al. 2003b]

Normally, longer $DI$ yield longer $APD$, so that the restitution curve increases in a monotonic way [Morgan et al. 1992a]. Some experimental studies have however reported the existence of non-monotonic or biphasic restitution curves in human ventricular tissue, showing a local maximum and minimum at low diastolic intervals [Franz et al. 1983, Morgan et al. 1992b]. The difference in $APD$ between these extremals is about 40 ms, while the local maximum

occurs at $DI$ between 50 and 100 ms. The precise mechanism underlying biphasic restitution is still poorly understood, but it was suggested to be the result of a supernormal behaviour of the calcium dynamics resulting in increased calcium channel activity [Bass 1975, Iunuma and Kato 1979, Morgan et al. 1992b]. Hence, we reproduced biphasic restitution in a phenomenological way, by modification of the L-type calcium channel in ionic models. The equation of the L-type calcium current $I_{Ca}$ is usually given by

$$I_{Ca} = g_{Ca} \cdot d \cdot f \cdot (V_m - E_{ca}) \tag{4.31}$$

where $g_{Ca}$ denotes the conductance, $E_{Na}$ the reversal potential and $d$ and $f$ gating variables of the Hodgkin-Huxley type [Hodgkin and Huxley 1952], fulfilling a relaxation equation of the same type as equation (4.33).

It is known that the $APD$ is correlated to the amplitude of $I_{Ca}$: larger amplitude results in longer $APD$. In order to reproduce biphasic restitution we replaced the constant value $g_{Ca}$ by $g_{Ca} + g_{Ca} \cdot S(cDI)$, where $S(cDI)$ is a function of $cDI$ (computed $DI$, see explanation later in the text). $S(cDI)$ is zero for almost all values of the argument, and is positive in a small interval of $cDI$, corresponding to the bump of the biphasic restitution curve. Basically, this function generates an extra inward current which elongates $APD$ for short $DI$. Using the following sigmoidal functions, we are able to design the function $S(cDI)$ in a controllable way:

$$\begin{aligned} S(cDI) = A \quad & \cdot(1 - tanh(a_-(cDI - d_-))) \\ & \cdot(1 + tanh(a_+(cDI - d_+))) \end{aligned} \tag{4.32}$$

By changing the parameters $A$, $a_+$, $a_-$, $d_+$ and $d_-$ we can fit the shape and location of the biphasic bump to any experimentally obtained curve.

In order to make our fits as close as possible to real experimental data we need to correlate $cDI$ to the real diastolic interval. However, the real $DI$ is not a variable of ionic models, and therefore, we introduced a new gating variable $d_s$, with following dynamics:

$$\partial_t d_s = \frac{d_{s,\infty}(V_m) - d_s}{\tau_{d_s}(V_m)} \tag{4.33}$$

with

$$d_{s,\infty} = 5.0 \quad \tau_{d_s} = 10.0 \quad \text{for } V_m \in [-55, -40] \tag{4.34}$$

$$d_{s,\infty} = 1.0 \quad \tau_{d_s} = 200.0 \quad \text{for } V_m < -55 \tag{4.35}$$

$$d_{s,\infty} = 1.0 \quad \tau_{d_s} = 5000.0 \quad \text{for } V_m > -40 \tag{4.36}$$

It is easy to see that the value of $d_s$ is close to 5.0 at the back of the 'preceding action potential' when $V_m = -55$, and then (until the next pulse) exponentially decays to the value 1.0 with a time constant of 200.0 ms. The time constant of 5000.0 ms when $V_m > -40$, guaranties that $d_s$ remains almost unchanged over the bulk of the action potential (till its back). It can then be found that $DI$ can be evaluated from the value of $d_s$ by following equation:

$$cDI = -20 - 200 \cdot \ln \frac{d_s - 1}{4} \tag{4.37}$$

Equations (4.32), (4.33) and (4.37) provide a framework for fitting basic restitution curves of human ventricular tissue and make desired modifications thereof. Note that, the several

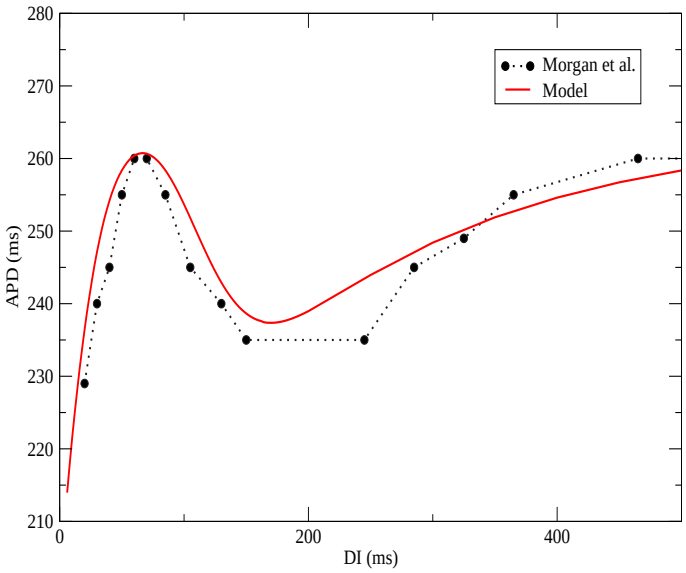


Figure I.11: Biphasic action potential duration restitution fitted to experimental data obtained by Morgan et al. [Morgan et al. 1992b].

constants used for such a fitting, for example $d_{s,\infty} = 5.0, \tau_{d_s} = 5000.0$, are phenomenological and one can easily achieve similar fits using other numerical values.

We were able to fit biphasic $APD$ restitution curves obtained in experiments performed by Morgan et al. [1992b]. Figure I.11 shows such a fit, where we used following parameter values: $A = 0.32$, $a_+ = 0.04$, $a_- = 0.025$, $d_+ = 35$ and $d_- = 125$. The simulated restitution curve was obtained using an S1-S2 stimulation protocol, with 10 S1 stimuli at 1s basic cycle length and an S2 stimulus at a certain $DI$ after the last S1 AP.

## 5 Discussion

### 5.1 The 3-variable model

This model is an improvement compared to the usual 2-variable FHN-models [FitzHugh 1961, Nagumo et al. 1962, Aliev and Panfilov 1996]: the restitution of action potential duration can easily be fitted to any experimental curve, by adjusting the parameters $\tau$, $\tau_r$ and $w_p$, as can be inferred from (I.2). Moreover, we use a detailed equation for the fast inward current that was fitted to match the fast sodium current equation from the PB model [Priebe and Breuckelmann 1998]. Hence, we have a realistic $CV$ restitution, that can be matched to experimental curves by altering the dynamics of $v$ through $\tau_v(V_m)$. Usually this is not the case in FHN-models, as excitability is modeled using a single parameter, that can solely control the activation threshold. Furthermore, the model is computationally efficient, as it only requires integration of three simple equations. On the other hand, our FHN-like model lacks an electrophysiological basis: although $I_{fi}$ is associated with the sodium current in real tissue, the description we use for the slow currents is not realistic. Study of pharmacological interventions is therefore not possible with such a model, as many drugs are designed to block the slow potassium or calcium currents [Qu et al. 1999]. Moreover, the shape of the AP is

idealised, while it is believed to be important in many problems, e.g. in electrocardiography [Plonsey and Barr 1988]. These were the main reasons, why we decided to develop a more detailed type of model, while retaining the computational efficiency of FHN-models.

## 5.2 The rPB model

*The action potential:* The results of our simulations show that the overall properties of the AP in the original PB model are well reproduced in the reduced model. The shape of the AP is similar in both models (Fig. I.5) and AP parameters are preserved (Table I.3). In order to have comparable $V_r$ and $APD$ we had to increase $g_{K1}$ by 56%. With a maximum outward current in the negative voltage range of 0.36 pA/pF at -60 mV, Beuckelmann et al. [1993] found quite low values of $I_{K1}$ in human ventricular myocytes, whereas higher values, up to 8 pA/pF [Koumi et al. 1995], have been reported in other studies. In our reduced model, with increased $g_{K1}$, the maximum of $I_{K1}$ in the negative voltage range is 1.33 pA/pF, which is well within the range of experimental data.

*The main gated currents:* The overall time course of the individual ionic currents resembles that in the original model (Fig. I.5). The amplitudes of $I_{to}$ and $I_{Ca}$ are however larger than in the PB model, due to the adiabatic elimination of the activation variables $r$ and $d$, respectively. The amplitude of $I_{to}$ is furthermore enhanced by a 30% increase in $g_{to}$. This increase was necessary to preserve the typical notch that follows the AP upstroke. Although these amplitudes may seem less realistic, we found that they had no influence on the properties of the AP we studied.

*Restitution properties:* The restitution properties of the original PB model were obtained far from steady states, where large ionic drifts occur (see Fig. I.9). Therefore, we didn't solely compare our model with the original PB model, but also with available experimental data. The reformulated model closely fits the data obtained by Morgan et al. [1992a] (Fig. I.6A). The $CV$ restitution is steeper than in the full model (Fig. I.7B). Since there are no experimental data on $CV$ restitution in human myocardium we did not attempt to flatten the $CV$ curve in the reduced model. Moreover, when Saumarez et al. [1992] measured the latency of propagating pulses in human ventricular tissue, they found that normal ventricular tissue (less susceptible to cardiac arrhythmias) showed a steeper increase in latency at short $DI$ than the tissue of patients who had cardiac arrhythmias. Therefore, the steeper curve in the reduced model may be an even more accurate model of normal ventricular tissue.

*AP heterogeneity:* Based on experimental findings on $I_{to}$ and $I_{Ks}$ [Li et al. 1998, Liu et al. 1993], we were able to reproduce the observed AP heterogeneity in the ventricular muscle. We obtained an $APD$ prolongation in the M cells through a 50% block of $I_{Ks}$ like reported by Liu et al. [1993]. The simulated $APD$ difference between M cells and epi- and endocardium is however smaller than the difference observed by Li et al. in myocytes isolated from human right ventricle [Li et al. 1998]. This could indicate that other currents are involved in the $APD$ prolongation of M cells. Indeed, $I_{K1}$ seems to be somewhat smaller in M cells from canine ventricle [Liu et al. 1993], and transmural inhomogeneities in other currents are starting to be reported as well [Ashamalla et al. 2001, Zygmunt et al. 2000, 2001]. On the other hand, quite small $APD$ differences were measured in guinea-pig ventricular tissue by Main et al. [1998]. These observations reflect species differences and more recently differences between right and

left ventricles have also been observed [Volders et al. 1999]. For the moment, we feel that our simulations of the observed transmural AP heterogeneity, based on differences in $I_{to}$ and $I_{Ks}$, are realistic enough, but are aware that we may have to include transmural inhomogeneities in other currents as well, once these are demonstrated experimentally in human ventricle.

*Numerical efficiency:* We were able to reformulate the PB model with 5 gating variables by altering only two electrophysiological parameters, $g_{to}$ and $g_{K1}$. The total number of variables has been reduced from 15 in the original model to 6 in the reformulated model, i.e., the membrane potential $V_m$ and the gating variables of $I_{Na}$ ($m$ and $v$), $I_{Ca}$ ($f$), $I_{to}$ ($to$), and $I_K$ ($X$). The computational gain at the cellular level was of the order of a factor 4. The computational speed can be increased further by the choice of sophisticated numerical schemes, such as adaptive space masks [Cherry et al. 2000] or adaptive time step schemes [Qu and Garfinkel 1999]. We used a scheme similar to the latter in 2D simulations of reentrant arrhythmias. Furthermore, there was a considerable gain in stability and rate adaptation. Moreover, in the reduced model, it is less difficult to relate changes in parameter values to changes in the action potential. Taken together, the reformulated model is very efficient for extensive 2D and 3D simulations of reentrant arrhythmias.

*Limitations of the model:* The inherent limitations of the full PB model have been discussed in the paper by Priebe and Breuckelmann [1998]. The main limitation of our reformulated model is the lack of ionic concentration handling. Giving constant values to all intracellular concentrations is a drastic way of reducing the number of equations and puts some constraints on the applicability of the model: the dynamics of calcium overload, sodium overload, etc., can no longer be studied. It should, however, be noted that the equations representing the calcium subsystem are still evolving and even the latest comprehensive models fail to adequately represent fundamental properties of calcium handling. Jafri et al. [1998] have incorporated an entirely new description of intracellular $Ca^{2+}$ handling into the phase-2 Luo-Rudy model, resulting in a set of as many as 30 ordinary differential equations that provide an improved description of the L-type $Ca^{2+}$ channels and CICR release from ryanodine receptor channels exhibiting adaptation. Whereas this model reproduces important aspects of cardiac $Ca^{2+}$ cycling, it also exhibits all-or-none rather than graded $Ca^{2+}$ release [Rice et al. 1999].

### 5.3 Modeling biphasic $APD$ restitution

We have developed a method to modify the calcium current in order to obtain biphasic restitution curves. Our method is an improvement compared to previous constructions of biphasic curves, where $DI$ was an external variable that needed to be evaluated in each point of the medium [Zemlin and Panfilov 2001, Qu et al. 1997]. Fenton et al. introduced a new current in the Fenton-Karma model [Fenton and Karma 1998] in order to obtain supernormal action potentials [Fenton et al. 2002]. Their restitution curves showed however some qualitative differences with experimental data. In our model we can easily relate the dynamics of the new variable $d_s$ to the diastolic interval and hence, change the restitution properties in a straightforward way. We illustrate this by fitting an experimental restitution curve obtained by Morgan et al. [1992b]. We modeled biphasic restitution curves by modifying the calcium current, based on some experimental studies [Bass 1975, Iunuma and Kato 1979, Morgan et al. 1992b]. However, until today, there's no agreement on the exact mechanism

of biphasic restitution. Our approach can easily be extended to reproduce other mechanisms of such non-monotonicity, for example by modifying the potassium current conductance $g_K$ into $g_K \cdot (1 - D(cDI))$, with a function $D(cDI)$ similar to $S(cDI)$ from (4.32). Note that, the presented method can be applied to any ionic model of cardiac tissue.

# II
# Electrocardiography

The electrical properties of the heart can be recorded by measuring the electrical potential in points of the body. The tracings of the electrical activity of the human heart, the electrocardiogram (ECG), was first measured by Augustus Waller in 1887. Since then, the techniques for recording the electrical signature of the heart on the human torso have been improved continuously. In this chapter we discuss the forward and inverse problems in the electrocardiography. The forward problem deals with the formulation of models of the electrical sources in the heart, where the main aim is to compute the resulting potential in a field point, which is of primal importance for the modeler. In most clinical applications however, the interest lies in determining the nature of the source from a set of potentials recorded at some distance from the heart. This is called the inverse problem.

## 1 Genesis of the electrocardiogram

The electrical activation of the heart starts in the right atrium in the sinoatrial (SA) node, which consists of specialised muscle cells which are self-excitatory. From the SA node, activation spreads throughout the atria, but it cannot propagate directly across the boundary between atria and ventricles. The pulse has to pass through the atrioventricular (AV) node, the only conducting pathway between atria and ventricles. Propagation from the AV node to the ventricular muscle is provided by a specialised conduction system. Initially, the system consists of a large bundle, called the bundle of His, which separates into two bundle branches propagating along each side of the interventricular septum. These branches further ramify into Purkinje fibers that diverge to the inner side of the ventricular walls. From there, activation propagates through the ventricular wall. After activation, a repolarisation wave can be observed, as all cells return to their rest state. Figure II.1 depicts the action potentials in the different regions described above. It also shows a standard ECG signal. We see that the P-wave is associated with the activation of the atria, whereas the QRS-complex occurs when ventricles are activated. The T and U waves correspond to the ventricular repolarisation, while atrial repolarisation is masked by the ventricular activation.

## 2 The forward problem

The forward problem in electrocardiography deals with the formulation of models for the electrical sources and for the volume conduction effects of the body. The main aim is to compute the resulting potential in a field point, given the electrical sources and the conducting media.

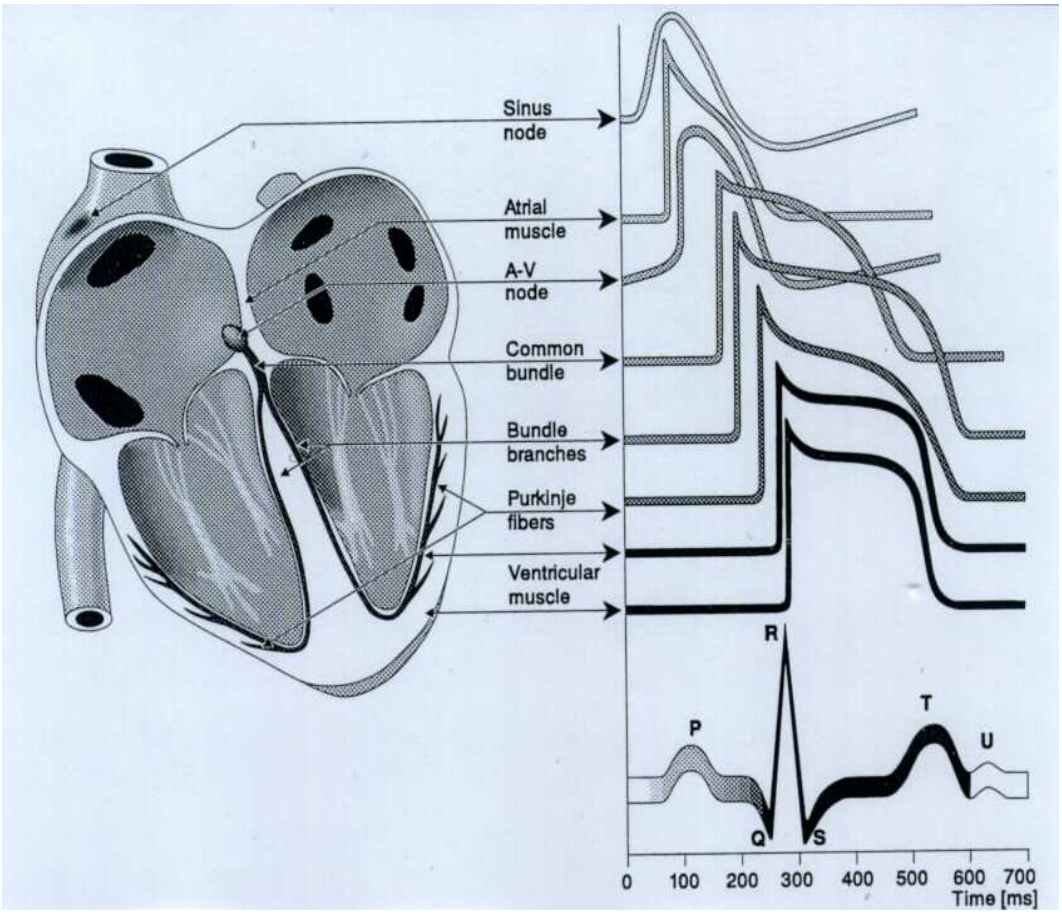


Figure II.1: Action potentials in different regions of the heart and standard electrocardiogram (taken from [Malmivuo and Plonsey 1995]).

## 2.1 Potentials in an infinite medium

*Equations of Laplace and Poisson*

We can introduce some electric potential $\Phi$ defined by $-\nabla\Phi = \vec{E}$, $\vec{E}$ being the electrical field. Using the relation $\vec{J} = \sigma\vec{E}$ with $\sigma$ the conductivity of the infinite, homogeneous medium, we obtain the equation of Laplace :

$$\nabla\sigma \cdot \nabla\Phi = 0 \tag{2.1}$$

This equation yields the potential at any point in the medium, provided there's no electrical activity.

In human heart tissue, there can exist some local 'impressed' current density $i_v$, that is resulting from the electrical activity of the cells. The total current must be zero, since there cannot be any charge accumulation in the medium. The potential in a point of the medium is in that case given by the equation of Poisson, where the term $i_v$ can be seen as the term $d\rho/dt$ in the equation for conservation of energy:

$$\nabla\sigma \cdot \nabla\Phi = -i_v \tag{2.2}$$

*Point Sources*

Consider a current point source with strength $I_0$ and position $\vec{r}$. For a homogeneous, isotropic, infinite medium this problem has spherical symmetry. Hence, the current density $\vec{J}$ in a point $\vec{r'}$ is oriented radially from the source and has strength:

$$J(\vec{r'}) = \frac{I_0}{4\pi R^2} \tag{2.3}$$

We then find easily the strength of the electrical field as being:

$$E(\vec{r'}) = \frac{I_0}{4\pi\sigma R^2} \tag{2.4}$$

From the relationship between the electrical field and the potential $\Phi$ we finally find :

$$\Phi_\infty(\vec{r'}) = \frac{-I_0}{4\pi\sigma}\int_\infty^{r'} \frac{1}{R^2}\, d\rho = \frac{I_0}{4\pi\sigma R} \tag{2.5}$$

This expression can also be found by solving the Poisson equation for $i_v(\vec{r'}) = I_0\delta(\vec{r}, \vec{r'})$.

Using the superposition principle, we find that the potential in a point $\vec{r'}$ generated by $N$ monopoles with strength $I_i$ and position $\vec{r}_i$ $(i = 1, \ldots, N)$ in an infinite, homogeneous, isotropic medium, is given by:

$$\Phi_\infty(\vec{r'}) = \frac{1}{4\pi\sigma}\sum_{i=1}^{N} \frac{I_i}{R_i} \tag{2.6}$$

In this case we speak about distributed sources.

If the impressed current sources are spread out in space, we take $dI = i_v\ dv$ and we integrate over the volume $V$ containing the impressed currents:

$$\Phi_\infty(\vec{r'}) = \frac{1}{4\pi\sigma}\int_V \frac{i_v(\vec{r})}{R}\, dv \tag{2.7}$$

Here we speak about continuous sources, within a certain volume.

*The Current Dipole as Distributed Source*

- Moments of a Current Source Distribution
  It is very useful to consider the moments of a distribution of current sources since this provide us with some basic insight in the nature of the potential field far away from all the impressed current sources.

  The starting point here will be expression (2.7), in which we replace $1/R$ by its Taylor expansion around the origin. Hence, we get:

$$4\pi\sigma\Phi_\infty(\vec{r'}) = \frac{1}{r'}\int_V i_v\, dv + \sum_{i=1}^{3}\Big(\frac{x_i'}{(r')^3}\int_V i_v x_i\, dv + \frac{1}{2}\frac{3(x_i')^2-(r')^2}{(r')^5}\int_V i_v x_i^2\, dV + \frac{3x_i'x_{(i+1)}'}{(r')^5}\int_V i_v x_i x_{(i+1)} dv + \ldots\Big) \tag{2.8}$$

  with $(x_1, x_2, x_3) = (x, y, z)$ and $x_{3+1} = x_1$.

  We now can define the moments of zero, first and second order corresponding with monopole, dipole and quadrupole potential terms (we ignore the higher order terms):

$$m = \int_V i_v\, dv \tag{2.9}$$

$$m_k = \int_V i_v k\, dv \quad k = x, y, z \tag{2.10}$$

$$m_{kl} = \int_V i_v kl\, dv \quad k, l = x, y, z \tag{2.11}$$

- The physical and mathematical dipole
  In heart tissue a single monopole cannot exists, since otherwise the medium would have an infinite charge. Therefore the total current must be zero. The simplest case, is the *physical dipole*: this configuration consists of a source with strength $I_0$ and a sink with strength $-I_0$, separated in space by a vector $\vec{a}$. The potential generated can be found by adding the contributions of the different terms of (2.8). For this configuration we have:

$$i_v = I_0\delta(\vec{x} - \frac{1}{2}\vec{a}) - I_0\delta(\vec{x} + \frac{1}{2}\vec{a}) \tag{2.12}$$

  The first term of (2.8) is then simply zero. The first order moment becomes:

$$m_x = \int_V i_v x\, dv = I_0 a_x \tag{2.13}$$

  In this way we can define the current dipole moment as $\vec{m} = I_0\vec{a}$.

  When we measure the potential at a distance that is much greater than $a$, we can neglect the higher order terms in (2.8), and we then get a good approximation for the *mathematical dipole*, for which the potential is given by:

$$\Phi_\infty(\vec{r'}) = \frac{1}{4\pi\sigma}\frac{\vec{m}\cdot\vec{R}}{R^3} \tag{2.14}$$

*Continuous Current Sources*

– Potential arising from a mono-layer
Consider the potential resulting from a surface $S$ at which a current density $J_S$ is fed into the medium.

By using the superposition theorem the infinite medium potential can be found by integration of the elementary monopoles $J_S dS$. We get:

$$\Phi_\infty(\vec{r'}) = \frac{1}{4\pi\sigma} \int_S \frac{J_S}{R}\, dS \tag{2.15}$$

Since current is leaving $S$ in both sides, we expect that there will be some discontinuity in the gradient of the potential, the electrical field. If we assume a closed surface $S$ with a constant $J_S$ along the whole surface, we can, using Gauss' theorem, easily find that the jump in $E$ is equal to $J_S/\sigma$.

– Potential arising from a double layer
A double layer is a surface $S_D$, at which elementary currents are generated such that each surface element $d\vec{S}$ carries an elementary dipole with moment $d\vec{m} = p(\vec{r})d\vec{S}$, with $p(\vec{r})$ the local current dipole per unit area.

By using the superposition theorem and (2.14) we the find that:

$$\Phi_\infty(\vec{r'}) = \frac{1}{4\pi\sigma} \int_S \frac{\vec{R} \cdot p(\vec{r})}{R^3}\, d\vec{S} \tag{2.16}$$

Now, we have that the solid angle $d\omega$ subtended by $dS$ at the field point, equals $\frac{\vec{R}\cdot d\vec{S}}{R^3}$, so equation (2.16) becomes an integration about the solid angle:

$$\Phi_\infty(\vec{r'}) = \frac{1}{4\pi\sigma} \int_S p(\vec{r})\, d\omega(\vec{r}) \tag{2.17}$$

The potential shows a discontinuity when crossing the double layer. This is the result from the jump in solid angle when going from the 'inside' to the 'outside' of the surface $S_D$. This jump equals $4\pi$.

## 2.2 Potential for a bounded medium

The first to obtain equations for spatially varying potential were Barr et al. [1966], using an approach based on Green's functions.

*General Formulation of the Potential in a Bounded Medium*

Consider a volume $V$ bounded by the surface $S$, and assume that the medium has a constant conductivity $\sigma$ within $V$. The region outside $S$ is left unspecified. We now apply the second theorem of Green on the functions $\Phi$ and $1/R$:

$$\int_V \Phi \triangle \frac{1}{R}\, dv - \int_V \frac{1}{R} \triangle \Phi\, dv = \int_S \Phi \nabla \frac{1}{R} \cdot d\vec{S} - \int_S \frac{1}{R} \nabla\Phi \cdot d\vec{S} \tag{2.18}$$

Now, using $\nabla\frac{1}{R} = \frac{\vec{R}}{R^3}$, $\triangle\frac{1}{R} = -4\pi\delta(\vec{r} - \vec{r'})$ and (2.2) we find :

$$\Phi(\vec{r'}) = \Phi_\infty(\vec{r'}) - \frac{1}{4\pi}\int_S \Phi(\vec{r})\, d\omega - \frac{1}{4\pi\sigma}\int_S \frac{J_n}{R}\, dS \tag{2.19}$$

With $\nabla\Phi \cdot d\vec{S} = -E_n dS = \frac{J_n}{\sigma} dS$. This means :
*The potential at an arbitrary point within a bounded medium is the sum of the infinite space potential at that point, a weighted integral of the potentials at the boundary and a weighted integral of the potential gradients at the boundary.*
The contributions of the two final terms are examples of virtual sources having the nature of a double layer and a mono layer.

*General formulation of the Boundary Element Method (BEM)*

In electrocardiography the external conductivity is assumed to be zero, so there are no currents leaving the volume. Hence, we get:

$$\Phi(\vec{r'}) = \Phi_\infty(\vec{r'}) - \frac{1}{4\pi}\int_S \Phi(\vec{r})\, d\omega \tag{2.20}$$

Now, it is clear that for practical situations we need to know what the potential is on the bounding surface $S$. When using (2.20) we encounter a singularity : if $\vec{r'}$ is lying on $S$, we can only integrate over the surface minus this point, because the solid angle becomes singular. We can deal with this problem by taking the limit for $\vec{r'}$ approaching the surface $S$ in point $\vec{r}_0$. Consider an infinitesimal area $\tau$ around $\vec{r}_0$; we can write that:

$$\lim_{\vec{r'}\to\vec{r}_0} \frac{1}{4\pi}\int_S \Phi(\vec{r})\, d\omega = \frac{1}{4\pi}\int_{S/\tau} \Phi(\vec{r})\, d\omega + \lim_{\vec{r'}\to\vec{r}_0} \frac{1}{4\pi}\int_\tau \Phi(\vec{r})\, d\omega \tag{2.21}$$

Since $\tau$ is very small, we can assume it is planar and that $\Phi(\vec{r})$ is constant. The limit for the solid angle of this planar part is than simply $-2\pi$ ('$-$' because we come from the inside of the surface).

We now can rearrange (2.20) in order to get the potential in a point $\vec{r}_0$ of the surface:

$$\Phi(\vec{r}_0) = 2\Phi_\infty(\vec{r}_0) - \frac{1}{2\pi}\oint_S \Phi(\vec{r})\, d\omega \tag{2.22}$$

Where $\oint$ stands for the exclusion of the singularity.

*The BEM-handling of inhomogeneities*

We will discuss the simple example of two nested conducting media and find an expression for the potential in those media.

Consider a medium $I$ bounded by a surface $S_1$ and having a conductivity $\sigma_1$. In this medium we consider an other conducting volume $II$ having a bounding surface $S_2$ and conductivity $\sigma_2$. We further assume that all current sources are within $I$ (outside $II$).

Assume $\vec{r'}$ is lying inside $I$ (but outside $II$). Application of Green's second theorem to $II$ gives:

$$\int_{II} \sigma_2\Phi\triangle\frac{1}{R}\, dv - \int_{II} \frac{1}{R}\triangle(\sigma_2\Phi)\, dv = \int_{S_2} \sigma_2\Phi\nabla\frac{1}{R}\cdot d\vec{S} - \int_{S_2} \frac{1}{R}\nabla(\sigma_2\Phi)\cdot d\vec{S} \tag{2.23}$$

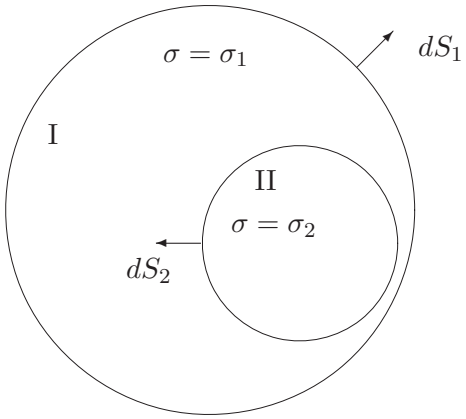


Figure II.2: Two nested media with different conductivities.

Since $\vec{r'}$ is lying outside $II$ and there are no current sources in $II$, the left hand side of (2.23) vanishes. We get:

$$0 = \int_{S_2} \sigma_2 \Phi \nabla \frac{1}{R} \cdot d\vec{S} - \int_{S_2} \frac{1}{R} \nabla(\sigma_2 \Phi) \cdot d\vec{S} \tag{2.24}$$

If we now apply Green's second theorem to $I$ we get ($I$ has $S_1$ and $-S_2$ as bounding surfaces):

$$\begin{aligned} &\int_I \sigma_1 \Phi \triangle \frac{1}{R}\, dv - \int_I \frac{1}{R} \triangle(\sigma_1 \Phi)\, dv \\ &= \int_{S_1} \sigma_1 \Phi \nabla \frac{1}{R} \cdot d\vec{S} - \int_{S_1} \frac{1}{R} \nabla(\sigma_1 \Phi) \cdot d\vec{S} - \int_{S_2} \sigma_1 \Phi \nabla \frac{1}{R} \cdot d\vec{S} + \int_{S_2} \frac{1}{R} \nabla(\sigma_1 \Phi) \cdot d\vec{S} \end{aligned} \tag{2.25}$$

Since there's no current across $S_1$ the second term on the right is zero and the fourth term on the right equals $-\int_{S_2} \frac{1}{R} \nabla(\sigma_2 \Phi) \cdot d\vec{S}$, since this expresses the current across $S_2$. By using (2.24) we finally get (after rearranging):

$$\Phi_1(\vec{r'}) = \frac{\sigma_s}{\sigma_1^-} \Phi_\infty(\vec{r'}) - \frac{1}{4\pi} \sum_{i=1}^{2} \frac{\sigma_i^- - \sigma_i^+}{\sigma_1^-} \int_{S_i} \Phi(\vec{r})\, d\omega \tag{2.26}$$

Where $\sigma_i^-$ is the conductivity inside $S_i$, $\sigma_i^+$ the conductivity outside $S_i$ and $\sigma_s$ the conductivity of the medium in which the current sources are. When $\vec{r'}$ is lying in $II$ we get an analogous expression for $\Phi_2$. Equation (2.26) can easily be generalised for the case of $N$ nested compartments of different conductivities. We then get:

$$\Phi_k(\vec{r'}) = \frac{\sigma_s}{\sigma_k^-} \Phi_\infty(\vec{r'}) - \frac{1}{4\pi} \sum_{i=1}^{N} \frac{\sigma_i^- - \sigma_i^+}{\sigma_k^-} \int_{S_i} \Phi(\vec{r})\, d\omega \tag{2.27}$$

In this expression a singularity occurs when $\vec{r'}$ lies on one of the surfaces. We can use the same procedure as for (2.22) and we obtain for the potential on $S_k$:

$$\Phi_k(\vec{r}_0) = 2\frac{\sigma_s}{\sigma_k^- + \sigma_k^+}\Phi_\infty(\vec{r}_0) - \frac{1}{2\pi}\sum_{i=1}^{N}\frac{\sigma_i^- - \sigma_i^+}{\sigma_k^-}\oint_{S_i}\Phi(\vec{r})\,d\omega \tag{2.28}$$

### 2.3 The equations for heart tissue

A review of the biophysical theory of action potential propagation in cardiac and nerve tissue can be found in [Malmivuo and Plonsey 1995] and [Gulrajani 1998]. In the monodomain approach, where extra- and intracellular media are lumped together, we have:

$$I_{ion} - C_m\frac{\partial V_m}{\partial t} = -\nabla\cdot(D\nabla V_m) \tag{2.29}$$

The left hand side is in fact the total impressed current density $i_v$. Substitution of this into (2.7) and (2.31), taking into account that the gradient in membrane potential is zero on the boundary (there are no currents leaking), we finally find:

$$\Phi_\infty(\vec{r}_0) = \frac{1}{4\pi\sigma}\int_H(\nabla V_m)\cdot D\cdot(\nabla\frac{1}{R})\,dv \tag{2.30}$$

for the potential in an infinite homogenous medium and

$$\Phi_k(\vec{r}_0) = \frac{1}{2\pi(\sigma_k^- + \sigma_k^+)}\int_H(\nabla V_m)\cdot D\cdot(\nabla\frac{1}{R})\,dv - \frac{1}{2\pi}\sum_{i=1}^{N}\frac{\sigma_i^- - \sigma_i^+}{\sigma_k^-}\oint_{S_i}\Phi(\vec{r})\,d\omega \tag{2.31}$$

for a bounded inhomogeneous medium, where $H$ stands for the volume occupied by the heart tissue.

In all subsequent simulations we used equation (2.30) for the calculation of the electrocardiogram in a given point.

## 3 The inverse problem

In most biomedical applications the major interest lies in determining the nature of the source from a set of potentials recorded at some distance from the heart. This is called the inverse problem. Unfortunately, in general this problem cannot be solved. It is only when source models are postulated that one may find its parameter values on the basis of recorded potentials. This section discuss briefly some different techniques used to tackle the inverse problem. More details can be found in [van Oosteroom 1996, van Oosteroom and Oostendorp 1999] and references therein.

### 3.1 The Gabor-Nelson equations

If we consider the electrical source as being a single current dipole, it is possible to calculate the strength and position of the dipole on the basis of the potential on the bounding surface. The theory for this was worked out by Gabor and Nelson [1954] and it also requires the knowledge of the geometry of the bounding surface.

**Theorem 3.1 (Gabor and Nelson, 1954).** *For a homogeneous conducting medium with conductivity $\sigma$ and bounding surface $S$, the dipole moment $\vec{p}$ of a current dipole in the medium is given by:*

$$\vec{p} = \sigma \int_S \Phi \, d\vec{S} \tag{3.32}$$

*Moreover, the position $(X, Y, Z)$ of the dipole is fully determined by $S$, $\sigma$ and $\Phi$ on $S$.*

*Proof.* – Strength: the starting point here is the expression (see 2.11):

$$\vec{p} = \int_V i_v \vec{r} \, dv \tag{3.33}$$

For a homogeneous medium we may write $i_v = -\sigma \triangle \Phi$. Hence

$$p_x = \int_V i_v x \, dv = -\sigma \int_V x \triangle \Phi \, dv \tag{3.34}$$

Applying Green's second theorem yields:

$$\int_V \Phi \triangle x \, dv - \int_V x \triangle \Phi \, dv = \int_S \Phi \nabla x \cdot d\vec{S} - \int_S x \nabla \Phi \cdot d\vec{S} \tag{3.35}$$

Since $\triangle x = 0$ and $\nabla \Phi \cdot d\vec{S} = 0$ (no current flowing out of medium), we obtain by combination of 3.34 and 3.35 :

$$p_x = \sigma \int_S \Phi \, dS_x \tag{3.36}$$

which can be generalised to

$$\vec{p} = \sigma \int_S \Phi \, d\vec{S} \tag{3.37}$$

– Position: consider two point sources $I_0$ and $-I_0$ with positions $\vec{X} + \frac{1}{2}\vec{a}$ and $\vec{X} - \frac{1}{2}\vec{a}$ ($\vec{X} = (X, Y, Z)$ and $a$ small). The impressed current density $i_v$ is then given by $I_0 \delta(\vec{x} - \vec{X} - \frac{1}{2}\vec{a}) - I_0 \delta(\vec{x} - \vec{X} + \frac{1}{2}\vec{a})$ and the first and second moment become :

$$\begin{cases} \int_V i_v x \, dv & = I_0 a_x = p_x \\ \int_V i_v x^2 \, dv & = 2X I_0 a_x = 2X p_x \end{cases} \tag{3.38}$$

Substitution of $i_v = -\sigma \triangle \Phi$ and applying Green's second theorem on the second equation, we find:

$$X p_x = \sigma \int_S x \Phi \, dS_x - \sigma \int_V \Phi \, dv \tag{3.39}$$

and similarly:

$$Y p_y = \sigma \int_S y \Phi \, dS_y - \sigma \int_V \Phi \, dv \tag{3.40}$$

$$Z p_z = \sigma \int_S z \Phi \, dS_z - \sigma \int_V \Phi \, dv \tag{3.41}$$

In these equations, the last term cannot be evaluated as we only have potential recordings on the bounding surface. After elimination of this term, only two independent equations remain, and the position cannot yet be established. Therefore, we derive in a similar way the following equation:

$$Xp_y + Yp_x = \int_V xy\, i_v\, dv = \sigma \int_S \Phi x\, dS_y + \sigma \int_S \Phi y\, dS_x \tag{3.42}$$

Performing the same calculations for other combinations of $(x, y, z)$ and adding the previously found equations, we end up with a system of 6 linear dependent equations for the computation of $(X, Y, Z)$ :

$$\begin{cases} Xp_x - Yp_y & = \sigma \int_S x\Phi\, dS_x - \sigma \int_S y\Phi\, dS_y \\ Xp_x - Zp_z & = \sigma \int_S x\Phi\, dS_x - \sigma \int_S z\Phi\, dS_z \\ Yp_y - Zp_z & = \sigma \int_S y\Phi\, dS_y - \sigma \int_S z\Phi\, dS_z \\ Xp_y + Yp_x & = \sigma \int_S \Phi x\, dS_y + \sigma \int_S \Phi y\, dS_x \\ Xp_z + Zp_x & = \sigma \int_S \Phi x\, dS_z + \sigma \int_S \Phi z\, dS_x \\ Yp_z + Zp_y & = \sigma \int_S \Phi y\, dS_z + \sigma \int_S \Phi z\, dS_y \end{cases} \tag{3.43}$$

In principle, any selection of three linear independent equations of 3.43 is sufficient to compute the position of the dipole. In practice however, numerical computation of some integrals might give singularities and hence reduce the choice of equations.

□

### 3.2 Correlation based methods

Simulated electrocardiograms $\tilde{E}(\vec{r}, t)$ may be characterised as being realistic or not, when compared to measured data $E(\vec{r}, t)$. Differences between the two data sets can be quantified by means of the relative difference $RD$, which is defined by:

$$RD = \sqrt{\frac{\sum_{i=1}^{P}\sum_{t=1}^{T}(\tilde{E}_{it} - E_{it})^2}{\sum_{i=1}^{P}\sum_{t=1}^{T} E_{it}^2}} \tag{3.44}$$

where $E_{it}$ and $\tilde{E}_{it}$ are the measured and simulated data at point $i$ at time $t$. Small values of $RD$ indicate a simulation of possibly high quality.

Alternatively, one can measure the scaled covariance $\rho$ as a measure for the quality of the simulated data. It can be shown that $\rho$ relates to $RD$ as

$$\rho \approx 1 - \frac{1}{2} RD^2 \tag{3.45}$$

for small values of $RD$.

### 3.3 Parameter estimation methods

Usually the parameters of the volume conductor are known and a priori chosen (and kept constant). The parameters describing the source may be varied such that simulated data

most closely resemble the observed data. Such inverse procedure is called a parameter estimation method, in which the free model parameters are varied until the squared RMS difference between simulated and observed data reaches a minimum. Over the last few decades several powerful numerical solution methods have been developed, which are now intensively used in the inverse problem in electrocardiography.

## 4 Measurement of the electric activity of the heart: lead systems

Bioelectric potentials are recorded by placing two or more electrodes on or inside the body and measuring the potential differences between these electrodes. By lead system we refer to the particular configuration used, with respect to the number and location of the electrodes.

Consider a dipole a at fixed location within a conducting medium. We introduce a coordinate system with the dipole in its origin and study the electrical potential in a point $P$ of the medium. Consider the dipole moment to equal $\vec{e}_x$ and the potential in $P$ to equal $c_x$. If we multiply the dipole moment by $p_x$, then, because of the linearity of $\Phi$ in $\vec{p}$ (see 2.14), the potential measured in $P$ will be given by $c_x p_x$. By similar considerations for the other coordinate axes, we can write the potential $\Phi_P$, generated by an arbitrary dipole at the origin, measured in point $P$ as:

$$\Phi_P = c_x p_x + c_y p_y + c_z p_z \tag{4.46}$$

The values $c_x$, $c_y$ and $c_z$ can be seen as the components of a vector $\vec{c}$, which we will call the *lead vector*. Since the potential was measured in a single point with respect to a reference point which was considered to have a zero potential, we speak of an unipolar recording or lead.
In practice, we mostly work with bipolar leads, by comparing the electrical potential between two different electrodes. The recoded voltage difference between a lead $i$ and $j$ is then given by:

$$V_{ij} = \Phi_i - \Phi_j = (\vec{c}_i - \vec{c}_j) \cdot \vec{p} = \vec{c}_{ij} \cdot \vec{p} \tag{4.47}$$

where $\vec{c}_{ij}$ is called the bipolar lead vector.

We now briefly discuss a few lead systems which form the basis of the standard 12-lead system in use in medicine.

### 4.1 Einthoven's triangle

Einthoven (1908) chose three points on the limbs, which formed an equilateral triangle [Einthoven 1908]. These points were located in the left and right wrist and on the left knee and he measured the electrical voltage between them (see Figure II.3). He assumed the heart to be a single dipole with fixed position, but with variable magnitude and orientation. If we chose a Cartesian reference system with the triangle lying within the $xy$-plane and the heart in its origin, then the bipolar leads can be written as:

$$\begin{cases} \vec{c}_I & = \vec{e}_x \\ \vec{c}_{II} & = 0.5\,\vec{e}_x - \frac{\sqrt{3}}{2}\,\vec{e}_y \\ \vec{c}_{III} & = -0.5\,\vec{e}_x - \frac{\sqrt{3}}{2}\,\vec{e}_y \end{cases} \tag{4.48}$$

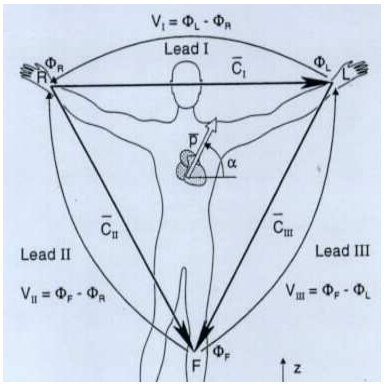


Figure II.3: Einthoven's triangle (taken from [Malmivuo and Plonsey 1995]).

### 4.2 Wilson's central terminal

F.N. Wilson investigated how unipolar recordings could be achieved in electrocardiography. Ideally, those should be measured with respect to a reference at infinity. He suggested to use a central terminal as reference, which was obtained by connecting from each electrode of Einthoven's triangle a 5 kΩ resistance to a central point, called the central terminal (Figure II.4) [Wilson et al. 1934]. It follows from Kirchoff's laws that the potential in the central terminal is given by the average of the potential in the three limb leads:

$$\Phi_{CT} = \frac{\Phi_R + \Phi_L + \Phi_F}{3} \tag{4.49}$$

Hence, we can add three recordings to the limb lead recordings of Einthoven:

$$\begin{cases} V_R &= \Phi_R - \Phi_{CT} = \frac{2\cdot\Phi_R+\Phi_L+\Phi_F}{3} \\ V_F &= \Phi_F - \Phi_{CT} = \frac{2\cdot\Phi_F+\Phi_L+\Phi_R}{3} \\ V_L &= \Phi_L - \Phi_{CT} = \frac{2\cdot\Phi_L+\Phi_R+\Phi_F}{3} \end{cases} \tag{4.50}$$

### 4.3 The augmented leads

In 1942 E. Goldberger observed that the recordings from Wilson's central terminal, could be enhanced by omitting the resistance connected to the measurement electrode [Goldberger 1942b,a]. In fact, doing so, one records the voltage between an electrode and the central terminal of the two others. In that way, the signal could be augmented by 50 %, which is the reason why they are called augmented leads. The voltages are given by:

$$\begin{cases} V_{aR} &= \Phi_R - \Phi_{CT} = \Phi_R - \frac{\Phi_L+\Phi_F}{2} \\ V_{aF} &= \Phi_F - \Phi_{CT} = \Phi_F - \frac{\Phi_L+\Phi_R}{2} \\ V_{aL} &= \Phi_L - \Phi_{CT} = \Phi_L - \frac{\Phi_R+\Phi_F}{2} \end{cases} \tag{4.51}$$

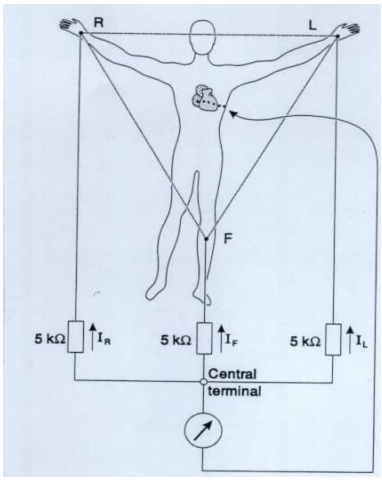


Figure II.4: Wilson's central terminal (taken from [Malmivuo and Plonsey 1995]).

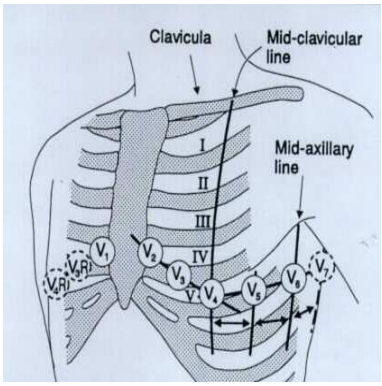


Figure II.5: Precordial leads (taken from [Malmivuo and Plonsey 1995]).

### 4.4 The standard 12-lead system

For measuring electrical activity close to the heart, F.N. Wilson introduced in 1944 six precordial leads [Wilson et al. 1944]. These leads, $V_1$ - $V_6$ are located over the left chest as denoted in Figure II.5. Together with Einthoven's limb leads and the augmented leads they form the 12-lead system which is the one with the greatest clinical use. Figure II.6 shows the recordings in the 12-lead system during the normal activation of the heart.

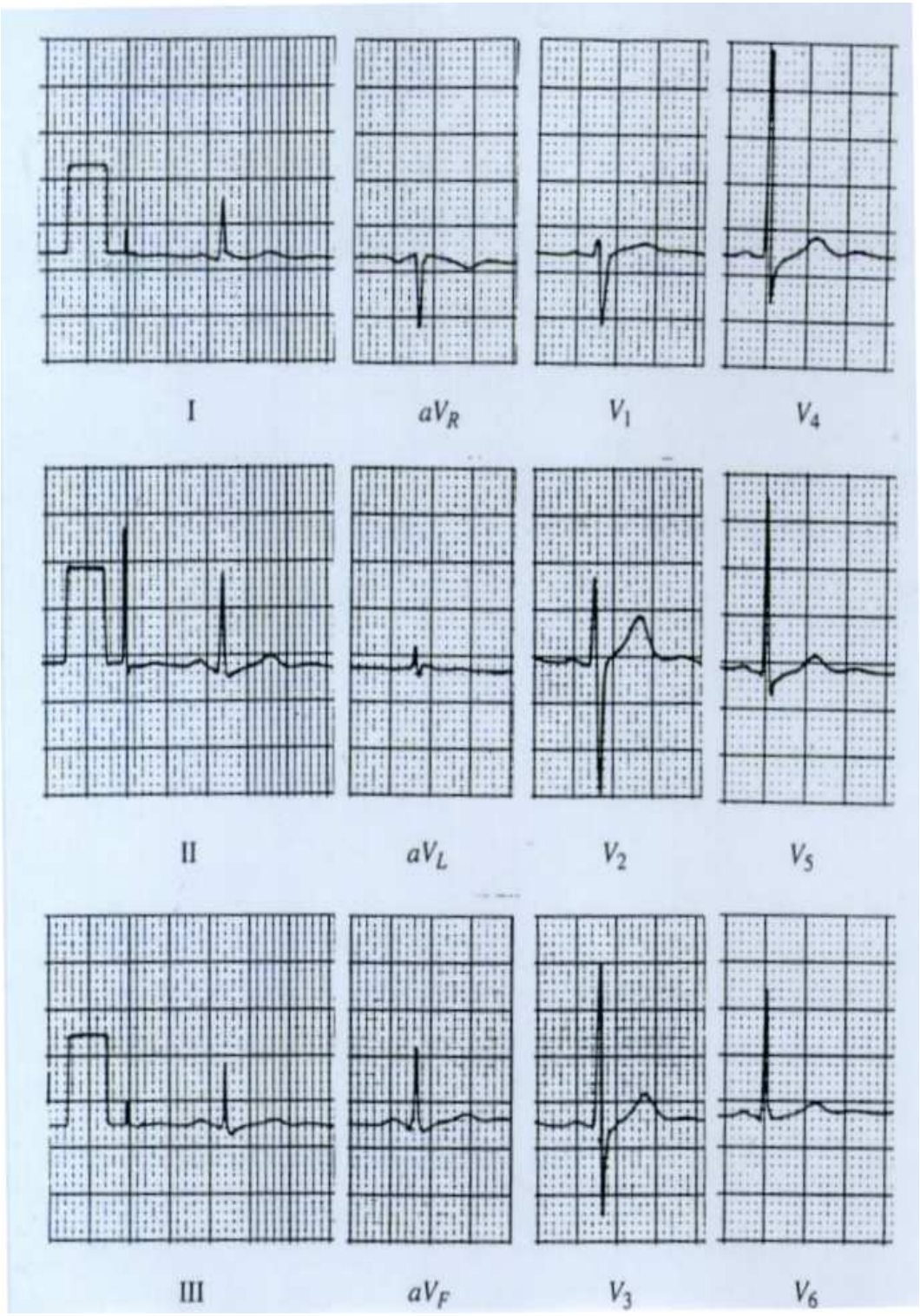


Figure II.6: Normal standard 12-lead ECG. The thick squares mark out 0.5 mV and 200 ms (taken from [Malmivuo and Plonsey 1995]).

# III

# Reentry and fibrillation in two-dimensional media

In this chapter, we study spiral waves in two-dimensional sheets of cardiac tissue, after a brief overview of the current hypothesises on ventricular tachycardia and its deterioration to ventricular fibrillation. We investigate their stability properties in the case of the normal parameter values and when simulating the effects of a specific drug, called cromakalim. We also simulate spiral waves in media with biphasic restitution curves and study how the biphasic bump can destabilise the reentrant source. Moreover, we show that a specific type of anti-arrhythmic drugs can prevent ventricular fibrillation or convert it to ventricular tachycardia.

## 1 Introduction

### 1.1 Spatial and temporal organisation during ventricular tachycardia and fibrillation

The mechanical contractions of the heart are triggered by electrical waves of excitation propagating through cardiac tissue from atria to ventricles, never exciting tissue twice. Abnormal propagation of excitation can result in life-threatening cardiac arrhythmias. Understanding the mechanisms of cardiac arrhythmias is extremely important for the development of new effective anti-arrhythmic drugs and clinical procedures of their management [Woosley 1999]. One of the most important types of cardiac arrhythmias, are so-called reentrant arrhythmias which occur as a result of recirculation of excitation along a closed anatomical path, or as spiral waves in thin (2D) slices of cardiac tissue [Allessie et al. 1973, Davidenko et al. 1991] or as scroll waves in thick (3D) slabs of myocardium [Frazier et al. 1989, Gray et al. 1995b, Janse 1998, Jalife 2000]. It is generally believed that the formation of rotating waves is the result of "wave breaks" of the propagating wavefront and that the dynamics of such broken wave fronts largely depends on the conditions of excitability and refractoriness of the tissue [Winfree 1994]. Stable spiral waves rotating around a circular core have been associated with monomorphic tachycardia, a rapid rhythm with a regular shape of the ECG [Gray et al. 1995b]. Experimental studies have however shown that vortices can drift throughout isolated pieces of thin ventricular epicardial tissue [Davidenko et al. 1991, Pertsov et al. 1993]. In the latter case, this drift was the result of intrinsic heterogeneities of the tissue. Using pseudo-ECG recordings, it was shown that drifting rotors can produce beat-to-beat changes in the QRS-complexes of the ECG (see Chapter II), resulting in a pattern that resembles recordings in patients during episode of polymorphic tachycardia and "torsades de pointes" [Davidenko et al. 1991, Pertsov et al. 1993, Davidenko 1993].

In some cases ventricular tachycardia (VT) can deteriorate in turbulent activation known as ventricular fibrillation (VF), which is the leading cause of death in the industrialised world [Myerburg et al. 1990]. For many years the most accepted hypothesis

for the mechanism of fibrillation was that anatomical and electrophysiological heterogeneities were the substrate for the development of many wavelets randomly propagating in cardiac tissue. Moe et al. [1964] were the first to test this hypothesis in a computer model of atrial fibrillation using a cellular automaton. They found that fibrillation occurred as a result of heterogeneity in the refractory period. It was initiated by a train of stimuli at high frequency, corresponding to cycle lengths of the order of the minimal refractory period of the medium. At such intervals, some cells fail to respond and the excitation front gets fragmented and multiple wavelets are formed. This work was further investigated by Krinsky [1966], who derived necessary conditions for self-sustained activity and demonstrated the existence of a critical mass for fibrillation depending on the extent of the heterogeneity. He also found that increased heterogeneity could have an opposite influence on fibrillation, by terminating it.
Experimental studies of such reentrant sources are difficult as they require simultaneous recordings of electrical activity in hundreds of points on the myocardium and in most cases activity can only be recorded from the heart surface. Such studies have however shown that ventricular fibrillation can differ from the multiple wavelet hypothesis, as it consists of a small number of wavelets with short lifespan [Gray et al. 1995b, 1998, Jalife et al. 1998b], which could indicate that fibrillation is generated by high-frequency intramural sources generating wave breaks at the heart surface. On the other hand, simulations have shown that the deterioration of tachycardia into disordered fibrillation can occur in homogeneous tissue, by the process of spiral wave break up. There are several mechanisms for spiral wave break up: some computations have shown that the anisotropy of ventricular tissue plays an important role in the dynamics of vortices [Fenton and Karma 1998, Qu et al. 2000b, Panfilov and Keener 1995b]. Spiral wave break up has also been observed in models of isotropic tissue and in those cases it was related to the restitution properties of the cells (see next section).
From all these possibilities, which mechanism is relevant for ventricular fibrillation ? Perhaps there's no single answer, as fibrillation may have different degrees of complexity and also different mechanisms (see [Jalife et al. 1998b, Panfilov and Pertsov 2001, Fenton et al. 2002] for reviews).

## 1.2 The restitution hypothesis as a mechanism for spiral wave break up

The restitution properties seem to play an important role in the stability of reentrant source and their eventual deterioration into ventricular fibrillation (VF): breakup of the wave will occur if the slope of the $APD$ curve is larger than 1 or less than $-1$ over a large range of diastolic intervals [Guevara et al. 1984, Karma 1994, Qu et al. 1999]. New reentrant sources are created via the breakup process and a complex pattern of activation sets in and the normal pumping of blood ceases. The restitution hypothesis, like it is commonly called, can be understood from basic stability analysis in one cell. Say we pace a cell at a constant rate, often referred to as basic cycle length ($BCL$). Due to $APD$ restitution we have for the $(n+1)$-th pulse:

$$BCL = APD_{n+1} + DI_{n+1} = APD(DI_n) + DI_{n+1} \tag{1.1}$$

The cell will tend to go towards the steady state given by:

$$BCL = APD(DI^*) + DI^* \tag{1.2}$$

We can now study the stability of this steady state, by assuming that after the $n$-th pulse $DI$ is $\epsilon_n$ away from $DI^*$ with $\epsilon_n$ very small. We will have a stable equilibrium only if the deviation from $DI^*$ disappears with time. By substitution of $DI_n = DI^* - \epsilon_n$ in (1.1), we find:

$$BCL = APD(DI^* - \epsilon_n) + DI^* + \epsilon_{n+1} \tag{1.3}$$

Since $\epsilon_n$ was assumed to be small, we can perform a first order Taylor expansion, and find using (1.2):

$$|\epsilon_{n+1}| = |\epsilon_n| \cdot |\frac{dAPD}{dDI}(DI^*)| \tag{1.4}$$

Hence, the steady state will only be stable if $|\frac{dAPD}{dDI}(DI^*)| < 1$.

This condition was also derived analytically for a pulse propagating in a one-dimensional ring [Courtemanche et al. 1993, Karma 1994, Courtemanche et al. 1996]. In more-dimensional media it is impossible to derive stability conditions for spiral waves or scroll waves analytically, unless making some approximations. The main problems are the anisotropic and heterogeneous properties of tissue, as well as the curvature effects of wave fronts on the conduction velocity, which can all by themselves destabilise reentrant source. Moreover, it has been shown in numerical simulations that the restitution of $CV$ might play a non-negligible role in the formation of wave breaks where new reentrant sources could be formed [Qu et al. 1999]. Several computations and experiments have shown directly or indirectly the importance of the restitution properties of cardiac tissue for the stability of reentrant arrhythmias [Qu et al. 2000b,a, Fenton et al. 2002, Koller et al. 1998, Riccio et al. 1999], but other causes for spiral wave breakup have also been observed [Panfilov and Keener 1995b, Fenton and Karma 1998, Bub et al. 2002].

## 2 Arrhythmias in the rPB model [Bernus et al. 2002a,b,c]

### 2.1 Mathematical and numerical approach

The cardiac tissue was described using the isotropic two-dimensional cable equation for the reduced PB model:

$$C_m \frac{\partial V_m}{\partial t} = -I_{ion} + \frac{1}{S \cdot \rho}\frac{\partial^2 V_m}{\partial x^2} + \frac{1}{S \cdot \rho}\frac{\partial^2 V_m}{\partial y^2} \tag{2.5}$$

with the same parameter values as in section 3.2 of Chapter I.

We used the operator-splitting method to split (2.5) into an ordinary differential equation (ODE) for reaction ($I_{ion}$) and a partial differential equation (PDE) for diffusion. The PDE was solved using an alternating-direction implicit scheme [Press et al. 1992], whereas for the ODE we used a time-adaptive forward Euler scheme with two possible time steps, $\Delta t_{min} = 0.02$ ms and $\Delta t_{max} = 0.1$ ms. In this scheme, for each point of the medium the ODE is solved with $\Delta t_{max}$; if $dV_m/dt < 1$ V/s we move on to the next point, otherwise we integrate the ODE at that point 5 times with $\Delta t_{min}$ from its initial value (see section 3.2 of Chapter I for an analysis of the stability of the numerical scheme). The relaxation equations for the gating variables were integrated using a technique presented by Rush and Larsen [1978] (Appendix B). All simulations were coded

in C++ and run either on a Compaq AlphaServer DS20E with a 666 Mhz Alpha 21264 CPU or a Dell 530 Precision Workstation with two Intel Xeon 2.0 GHz processors.

We obtained spiral waves using an S1-S2 protocol. We first paced one side of the tissue (S1) producing a plane wave propagating in one direction. When the refractory tail of this wave crossed the middle of the medium, we moved our pacing electrode to that site and applied a single stimulus (S2) parallel to the S1 wave front but not over the whole width of the medium. Stimulus currents lasted for 2 ms (S1) and 5 ms (S2) and their strength was two times threshold for both. The S2 wave front curled around its free end and produced a spiral wave. We calculated the trajectory of the spiral tip using an algorithm presented by Fenton and Karma [1998] along an isopotential line of 60 mV. We simulated electrograms of the spiral wave activity in 2D by calculating the dipole source density of the membrane potential $V_m$ in each element, assuming an infinite volume conductor [Plonsey and Barr 1988]. We recorded the electrogram with a single electrode located 10 cm above the center of the sheet of ventricular tissue.

## 2.2 Reentry under normal electrophysiological conditions

The 2D simulations were performed on a 700×700 square lattice with $\Delta x = 0.25$ mm. The results of these computations are shown in Fig. III.1. After application of the S2 stimulus (Fig. III.1A) the spiral tip drifts along the refractory tail of the wave (Fig. III.1B) before curling back (clockwise) and stabilising approximately at the middle of the medium (Fig. III.1C). Figure III.1D shows the trajectory of the tip after stabilisation. The tip motion occurs along lines that are ended by a quick turn through approximately 180°. The linear part of the trajectory rotates counterclockwise in space at an angular velocity of approximately 0.62 rad/s. This tip motion is characteristic of spiral waves with a linear core observed in experiments on thin slices of myocardium [Davidenko et al. 1991], in the whole heart [Efimov et al. 1999, Frazier et al. 1989] as well as in mathematical models of cardiac tissue [Efimov et al. 1995, Fast et al. 1990].

Figure III.2A shows a record of membrane potential in a point far from the spiral core (Fig. III.1C, asterisk) during 10 s after S1. Due to restitution the $APD$ changes from approximately 350 ms to approximately 280 ms. The average period of the spiral wave is 304.48 ± 3.09 ms (mean ± SD). Figure III.2B shows the ECG associated with the spiral wave. It is similar to ECGs obtained during polymorphic ventricular tachycardia. The Fourier transform of the ECG shows a dominant frequency around 3.29 Hz (not shown), which is comparable to the value of 3.65 ± 0.46 Hz obtained in clinical studies [Clayton et al. 1995].

## 2.3 Spiral wave breakup due to potassium channel-openers

Experimental studies have shown that the ATP-sensitive potassium channel openers are pro-arrhythmic as they reduce the refractory period and hence accelerate the heart rate during reentrant arrhythmias [Uchida et al. 1999]. We investigated the influence of this type of drugs, e.g. cromakalim, on the spiral wave dynamics in the reduced PB model. Since a potassium channel opener increases the conductance of the potassium channel and hence the efflux of potassium ions, we raised the potassium conductances $g_K$ and $g_{K1}$ from 0.019 nS/pF to 0.05 nS/pF, resp. 3.9 nS/pF to 9.75 nS/pF, and set

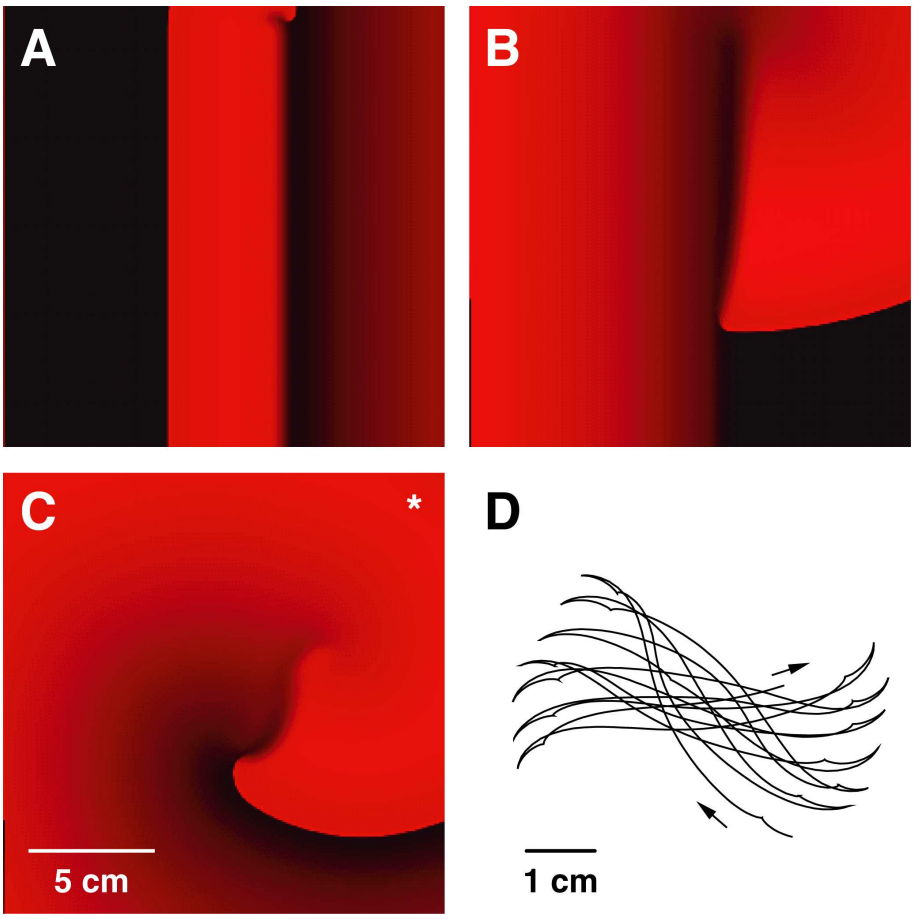


Figure III.1: Spiral wave activity in a 2D representation of the reformulated model. (A-C) Formation of spiral wave by an S1-S2 protocol. (D) Trajectory of spiral tip during 2 s after stabilisation. See text for details.

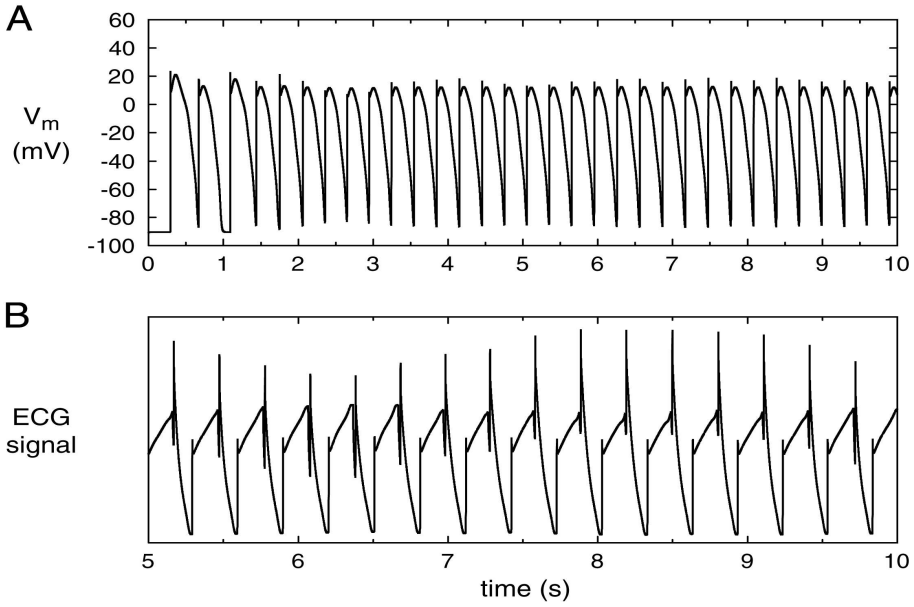


Figure III.2: Membrane potential and ECG during spiral wave activity of Fig.7. Note different time scales. (A) Membrane potential record at point (650,650) during 10 s after S1. (B) Non-scaled ECG (time zero at S1 delivery).

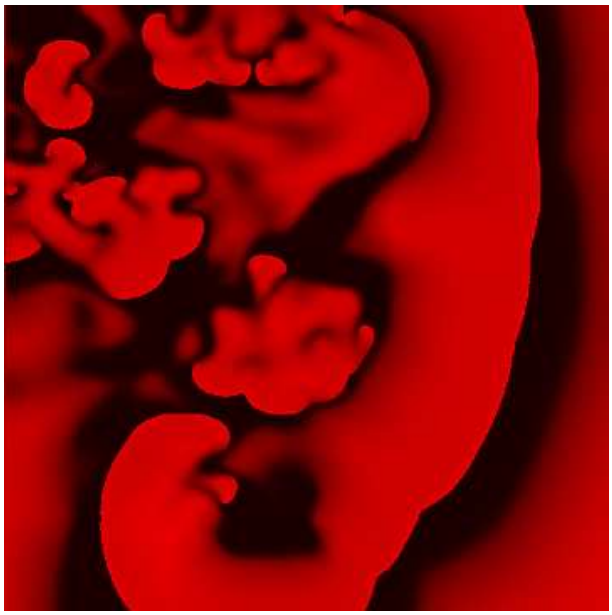

Figure III.3: complex activation due to spiral breakup 4s after initiation of spiral by S1-S2 protocol in a 2D sheet of ventricular tissue (25 cm $\times$ 25 cm), where red denotes activated cells ($V_m > -70$ mV), black quiescent cells.

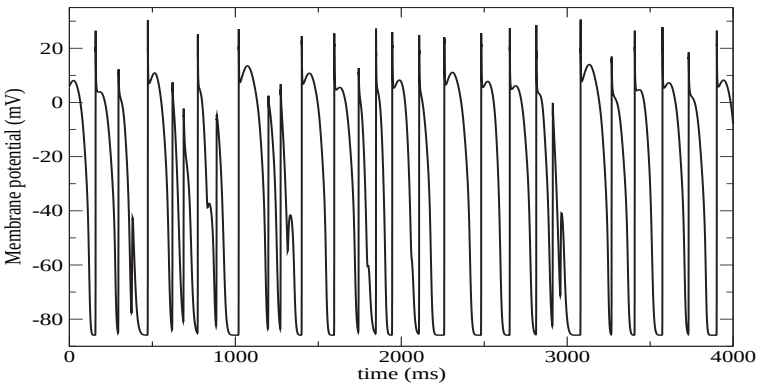


Figure III.4: Membrane potential recorded at the middle of the 2D sheet during VF-like activity.

the external potassium concentration to 5.4 mM. All other parameter values remained unchanged.

A complex activation pattern develops from an initial spiral wave, obtained by an S1-S2 protocol, as a result of the spiral breakup process. Figure III.3 shows the wave pattern 4 seconds after application of the S2 stimulus, while the electrical activity in a single cell at the middle of the sheet is shown in Figure III.4. We see multiple wavelets forming a turbulent activation pattern similar to those observed during VF in experimental studies [Garfinkel et al. 2000]. We studied VF for both the no-flux and periodic boundary conditions, in order to investigate the influence of boundaries on VF. In Figures III.5A and III.5B we show the computed ECGs for the no-flux and periodic boundary conditions. In both cases the ECG is irregular and has large variations in amplitude, similar to ECG recordings during VF. The Fourier transform of these ECG-signals has dominant frequencies at 2.8, 4.6 and 5.8 Hz for the no-flux boundary conditions (Figure III.5C), and at 4.4 and 6.0 Hz for the periodic boundaries (Figure III.5D). The evolution of the number of spiral tips is plotted in Figures III.5E and III.5F, for the no-flux, respectively periodic boundary conditions. We see that for the periodic boundary conditions the number of tips varies between 8 and 70, whereas for the no-flux boundaries it varies between 2 and 40. This difference is because spiral waves can disappear at boundaries in the no-flux case, resulting in smaller total number of wavelets.

We believe that the main mechanism for the break up of the spiral wave is the steep restitution curve, as we found the $APD$ restitution slope to be steeper than 1 for $DI$ going from 0 to 30 ms (see section 2.4).

### 2.4 A transition from complex patterns to organised activation by blocking the calcium channel

During the last decades, the only effective therapy for fighting VF was electrical defibrillation: the application of a strong electrical shock to the heart, which can restore the normal cardiac rhythm by eliminating abnormal sources of cardiac activation

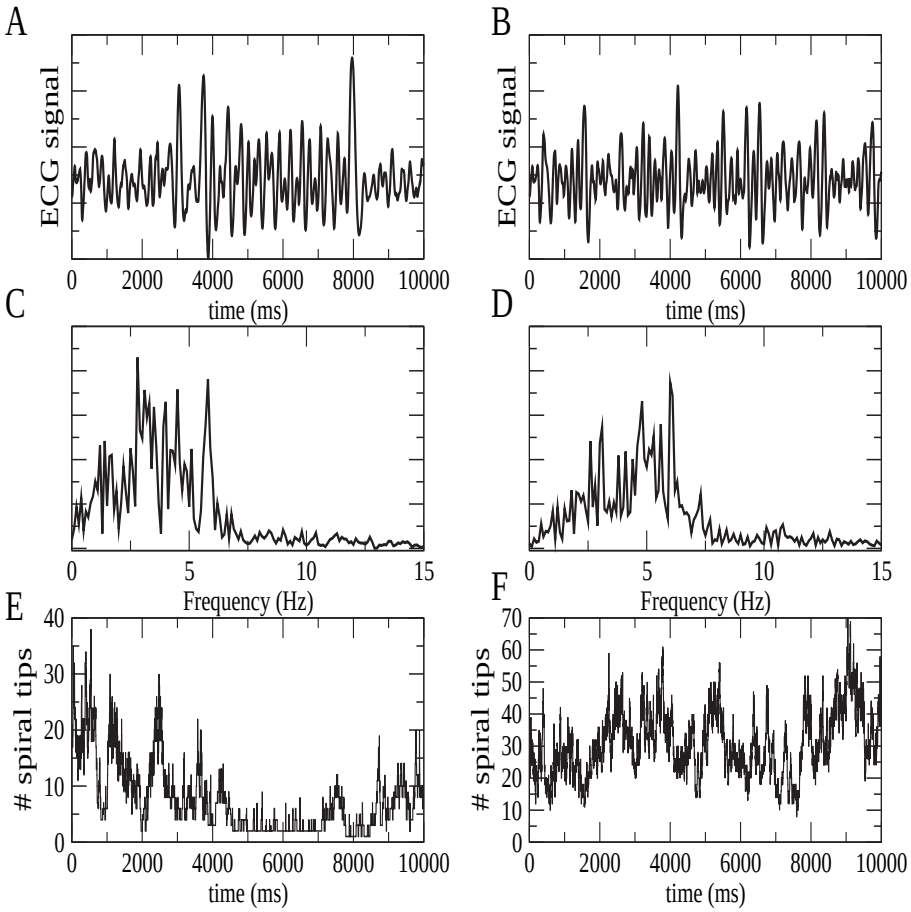


Figure III.5: ECG and evolution of the number of spiral waves in the 2D sheets of ventricular tissue. (A) ECG signal recorded 10 cm above the 2D sheet in the no-flux boundary case and (B) the periodic boundary case, (C) Fourier transforms of the ECGs in the no-flux boundary case and (D) periodic boundary case, and (E) number of spirals as a function of time in the no-flux boundary case and (F) periodic boundary case.

[Trayanova 2001]. Recent studies have however shown that not only electrical defibrillation, but also the administration of certain drugs can either reduce the complexity of wave patterns during VF [Chorro et al. 2000a,b, Samie et al. 2001], or even terminate VF, by converting it into ventricular tachycardia [Garfinkel et al. 2000]. Samie et al. showed that verapamil, a calcium-channel blocker, could convert VF into VT in experimental studies in rabbit hearts and in simulations of two-dimensional (2D) sheets of cardiac tissue [Samie et al. 2001]. In studies on dog hearts performed by Riccio et al., verapamil prevented the onset of VF [Riccio et al. 1999]. Garfinkel et al. showed that the drug bretylium, could convert VF to stable activity in experiments on pig hearts and in 2D or three-dimensional (3D) simulations [Garfinkel et al. 2000] using the guinea pig phase I Luo-Rudy model [Luo and Rudy 1991].

Despite a progress in understanding the mechanisms underlying the pharmacological management of VF, many questions remain unstudied. From the modeling side, for example, mechanisms and dynamics of the reduction of the number of abnormal sources of excitation are unclear. Recently, simulation studies on the evolution and interactions of reentrant sources of excitation have been performed by Clayton and Holden [2002] during VF-like activity, but not yet when simulating the effects of antifibrillatory drugs. The VF-to-VT transition was never modeled in cardiac tissue with realistic size, geometry or anisotropy. It would also be important to study this process in models which include ionic currents typical for human cardiac tissue.

In this section we investigate the transition from VF to VT after administration of a drug which was shown to be effective in preventing VF: the calcium-channel blocker verapamil.

*Methods*

In our computations we obtained a VF-like activation pattern by simulating the effects of cromakalim, like discussed in section 2.3, and waiting for 5s model time for a turbulent pattern to develop.

We simulated the effects of verapamil by blocking the calcium current, i.e. reducing its maximum conductance. We used following equation, similar to Qu et al. [1999] :

$$g'_{Ca} = g_{Ca} \cdot \left[(1-p) + p \cdot e^{-\frac{t-t_0}{\tau}}\right], \quad t \geq t_0 \tag{2.6}$$

where $g'_{Ca}$ denotes the calcium conductance under influence of the drug, $g_{Ca}$ is the conductance in normal situation, $p$ is the maximal block of the current (percent), $t$ is time, $t_0$ is the time at which drug is applied and $\tau$ is the relaxation time for the drug action.

*Results*

We used (2.6) with $\tau = 1$ s, and different values of $p$ to study different extends of reduction of the L-type calcium conductance $g_{Ca}$. We found that if we blocked the calcium current less than 70 percent the VF patterns persisted and even more wavelets were created than in the control situation. For $p \geq 0.75$, we observed a clear transition from turbulent activation to organised activation, where no further wave breaks

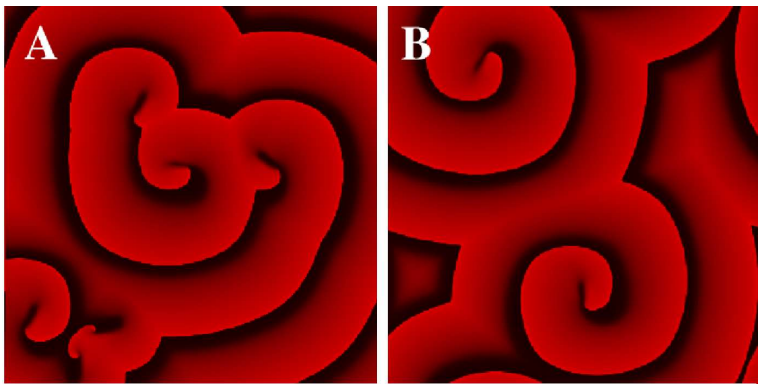


Figure III.6: Simulating the effects of a $Ca^{2+}$-channel blocker on complex activation: (A) in the 2D sheet with no-flux boundary 10 s after application of the drug, (B) in the 2D sheet with periodic boundary 10 s after application of the drug.

occurred and the number of spiral waves remained constant. Figures III.6A and III.6B show the activation pattern 5 s after 75% blockade of Ca current ($p = 0.75$), for the no-flux and periodic boundary conditions. We see that the patterns became spatially regular and consisted of 6 spiral waves for the no-flux boundary conditions and only 2 for the periodic boundary conditions. The associated ECGs show a clear transition from a VF-like state to PVT or Torsades de Pointes (Figures III.7A and III.7B). The dominant frequency after the stable patterns set in, is at 10.3 Hz, about 2 times higher than during the VF-like episode (Figure III.7C). The average number of spiral tips (Figure III.7D) decreased by over a factor 4 during the first second of drug action. It took another second for the periodic boundary conditions and two seconds for the no-flux boundary conditions to reach the steady state.

In our simulations, we found two main mechanisms responsible for the reduction of the total number of spiral waves: annihilation of counter-rotating spiral waves and collisions with no-flux boundaries. Figure III.8A shows how the tip of a spiral wave approaches a no-flux boundary of the medium (left side) and disappears. The annihilation of four spiral waves is shown in Figure III.8B. We see the formation of a single wavefront after the tips have coalesced. Note that similar processes occur during sustained VF as well [Gray et al. 1998, Clayton and Holden 2002, Lee et al. 2002], but during VF new sources of excitation are continuously formed and the system remains in a dynamical equilibrium.

We also investigated if a $Ca^{2+}$-channel blocker could prevent the transition from VT to VF, by applying the drug before the first wave break occurred in the control situation (no-flux boundary) and we obtained a single spiral wave, rotating at a frequency of 10.1 Hz in a stable manner around a linear core of about 1 cm (data not shown). Therefore, a block of the $Ca^{2+}$-channel can convert VF into VT, if it is applied during VF, or prevent the onset of VF, if it is applied during the preceding phase of tachycardia.

In order to identify the mechanism of this effect we studied how blocks of the $Ca^{2+}$-channel affected the properties of cardiac tissue, important for the development of VF. In order to test whether the restitution played a role in our case we computed $APD$ restitution curves in single cells, in the control situation and with a 75 % block of the L-type calcium channel. As can be inferred from Figure III.9A, a block of $I_{Ca}$

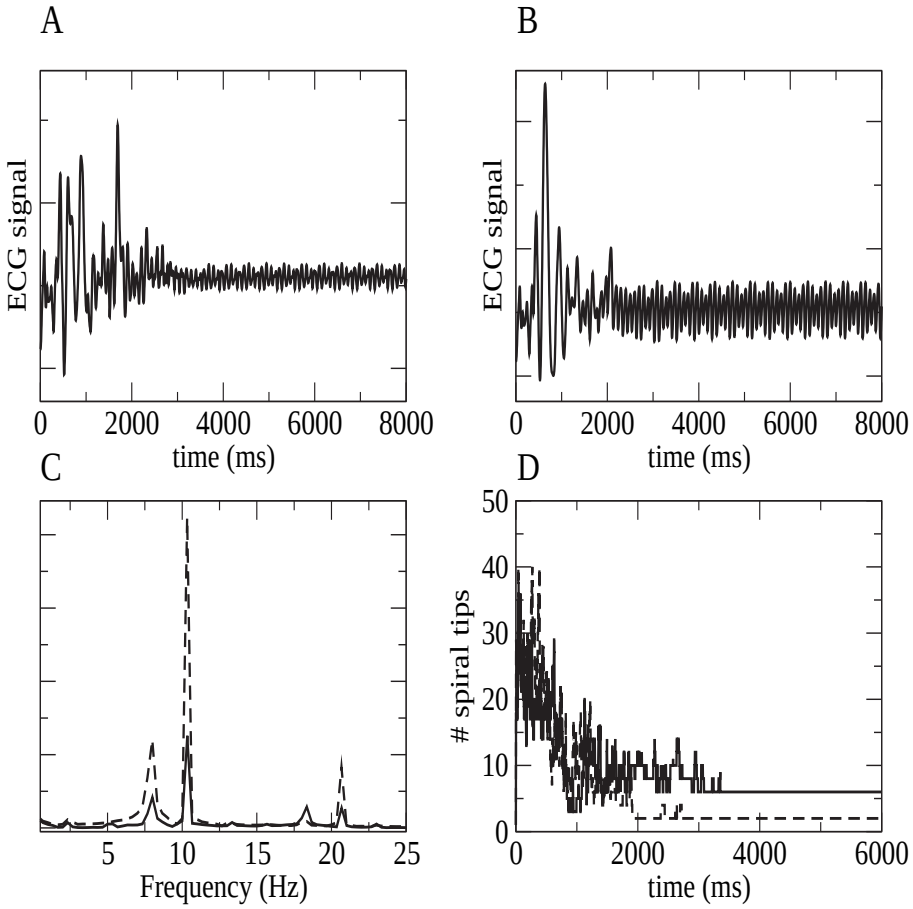


Figure III.7: Simulating the effects of a $Ca^{2+}$-channel blocker on complex activation in a 2D sheet of ventricular tissue. (A) ECG signal recorded 10 cm above the 2D sheet in the no-flux boundary case and (B) the periodic boundary case. (C) Fourier transforms of the ECGs during stable activity and (D) number of spirals as a function of time, where solid lines denote the no-flux boundary case and dashed lines the periodic boundary case.

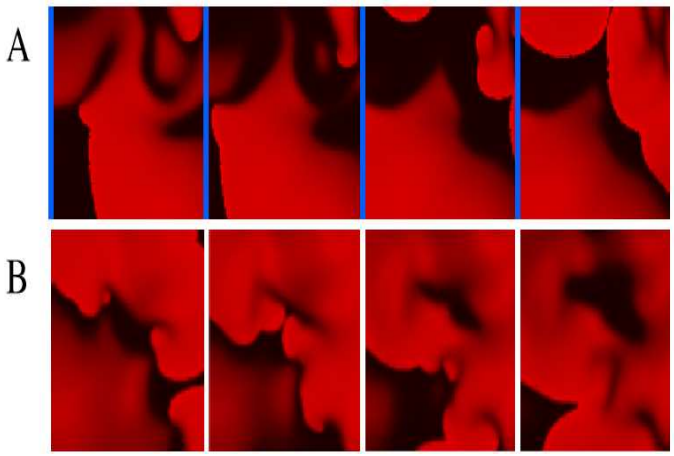


Figure III.8: Close-up on 2 mechanisms of death of spiral waves (red denotes activated cells, black quiescent cells): (A) collision with a no-flux boundary indicated in blue, (B) several spiral waves coalescing. The frames are 2.5×2.5 cm large and separated by time steps of 20 ms.

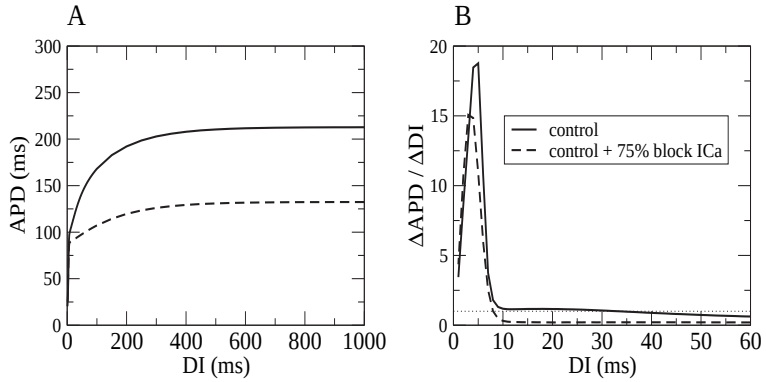


Figure III.9: (A) Action potential duration ($APD$) restitution curves in the control situation and in the control situation with 75 % block of $I_{Ca}$ and (B) their slopes, where the value of 1 is indicated by a dotted line.

| | set 1 | set 2 | set 3 | set 4 |
|---|---|---|---|---|
| $d_-$ | 125 | 125 | 100 | 95 |
| $d_+$ | 35 | -25 | 10 | 30 |
| $a_+$ | 0.025 | 0.025 | 0.125 | 0.175 |
| $a_-$ | 0.04 | 0.016 | 0.016 | 0.016 |

Table III.1: Different parameters sets for biphasic restitution.

reduces the $APD$ and decreases the overall slope of the restitution curve. This is further demonstrated in Figure III.9B, where $\Delta APD/\Delta DI$ is plotted against $DI$. In the control situation the slope is larger than 1, for $DI$ going from 0 to 30 ms, whereas with a 75 % block of the L-type calcium channel this range is reduced to the interval [0 ms , 8 ms]. Hence, the mechanism of stabilisation of wave patterns in our simulations is also due to a flattening of the restitution curve.

## 3 Spiral wave behaviour in the biphasic rPB model [Bernus et al. 2003b]

We investigated the influence of different biphasic restitution curves on spiral waves in 2D, by using four different setting of the parameters ($d_-$,$d_+$,$a_-$,$a_+$) shown in Table III.1, where set 1 corresponds with the fit of the experimental data of Morgan et al. [1992b] as described in section 4 of Chapter 1 ($A$=0.32 in all cases). Using set 2 we obtained the same curve as in the case of set 1, except for the positive slope at low $DI$, which steepness was reduced below 1 (Figure. 1b). For parameter sets 3 and 4 the steepness of the negatively slope region of parameter set 2 was increased, with a region of $\frac{dAPD}{dDI} < -1$ in both cases (Figure III.10A-D).

We started our study with parameter set 1 corresponding to the best fit of the experimentally measured restitution curve. We found that for that case spiral waves are unstable and break down in multiple daughter wavelets after the 4th rotation. From then on a complex activation pattern sets in, where new spiral waves are formed via the breakup process and other disappears at boundaries or when coalescing (similar to Figure III.3). It is reasonable to assume that in this case the breakup is due to a steep restitution curve, as the slope of the restitution curve exceeds unity at short diastolic intervals (Figure III.10A, right). This type of unstable behaviour resulting in breakup of the wavefront corresponds to spiral wave breakup observed in models of monotonous increasing restitution curves with a steep slope [Garfinkel et al. 2000, Qu et al. 1999, Bernus et al. 2002a].

In order to check this hypothesis we have studied a spiral wave in the case of set 2, where the magnitude of the positive slope at low $DI$ was reduced below 1 (Figure III.10B). We found that in this case the spiral wave remained stably rotating without any breakup. The period of spiral wave was about 230 ms and it had a $DI$ of 22 ms. The core was linear and had a diameter of about 5cm (Figure III.12A). The wavelength (the product of the period and conduction velocity) was approximately 11.5 cm.

Note that, for both sets 1 and 2 the slope of the negatively sloped part of the restitution curve was never lower than the critical value -1, for which one could expect the onset of instabilities [Zemlin and Panfilov 2001]. Therefore we used parameter set 3 which has

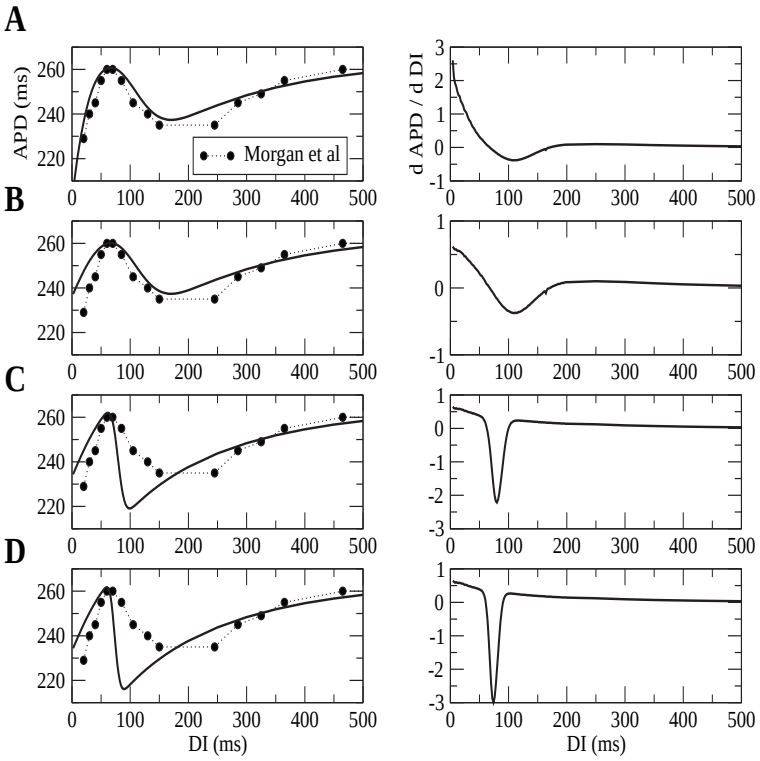


Figure III.10: Restitution curves for the different parameter sets compared to experimental data obtained by Morgan et al. [1992b]: (a) set 1, (b) set 2, (c) set 3 and (d) set 4.

Figure III.11: Spiral breakup using parameter set 3. Snapshot of electrical activity at 8.5s model time (red denotes activated cells, black quiescent cells).

a minimal negative slope of about -2, while the maximal positive slope is below one. We found that in this case the rotation of spiral became more instable. We repeatedly observed areas of conduction block forming close to the spiral tip and obtained, as a result, a complex meandering pattern which consisted of two processes: rotation along a linear core, which in this case is about 50 % percent longer than for set 2, and a drift of the spiral over a substantial distance (due to the conduction block). Ineffective breaks of spiral formed in the spiral arm starting from approximately 5th rotation, but they were not successful in creating new spiral waves, and a single spiral wave persisted for as long as 8.3s (or about 30 rotations). It rotated with an average period of 230ms (the same as for set 2) but the $DI$ was increased to the value of about 35 ms. At 8.3s we observed an effective breakup and afterwards a complex activation pattern set in, like illustrated by Figure III.11. We investigated the break up process occurring at 8.3s, by recording membrane potentials in points near the site of interest. We found that the break up was preceded by a period of alternans between short and long $APD$, before conduction block occurred in some points and new spiral wave could be formed (Figure III.13). This is similar to break up observed in media with steep positive slopes (see Figure III.4). The main difference lies however in the time needed by the spiral wave to develop break up.

In order to study the role of the magnitude of the negative slope in the dynamics of the spiral wave, we used parameter set 4 where the steepness of the negative restitution was further increased (Figure III.10D). We found an increased instable behaviour of the spiral wave: tip motion became more complex and the spiral wave showed a substantial drift in space (Figure III.12C). However, effective breakup here required a longer time and occurred around 10s. Afterwards a complex pattern similar to that of Figure III.11 was formed. We also found that the average $DI$ of the spiral wave was further increased to 50 ms. This seems to be correlated with observations made by Zemlin and Panfilov [2001] who showed that spiral wave with more negative slope have longer $DI$. In our case, as in [Zemlin and Panfilov 2001], the increase of $DI$ was achieved by a larger tip

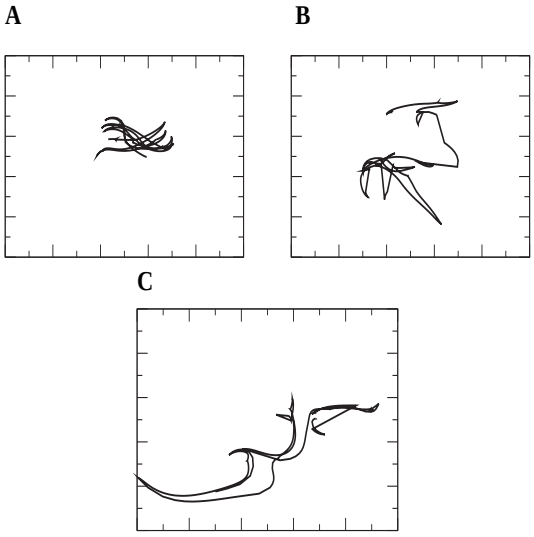


Figure III.12: Trajectory of the spiral wave tips in the case of parameter sets 2 (a), 3 (b) and 4 (c) during the interval [1000ms,2000ms]. The graphs have dimensions 12.5cm × 12.5cm.

motion.

In order to check whether the tip motion is important for the deterioration into a complex pattern, we initiated a spiral wave circulating around an unexcitable circular hole for parameter set 3. We chose the radius of the hole to be 2.5 cm in order to have a spiral wave rotating with a $DI$= 37 ms, comparable to the unbroken spiral wave in previous simulation with the same parameter set. We found that the reentrant wave remained stable and rotated at a constant $DI$ of 37 ms.

## 4 Discussion

### 4.1 Spiral waves under normal electrophysiological conditions

The spiral waves generated with the reformulated PB model show meandering dynamics, preceded by a short transient drift, and have a period of approximately 300 ms. The ECG of the 2D spiral waves is polymorphic and supports the idea that meandering reentrant arrhythmias underlie polymorphic ventricular tachycardias [Gray et al. 1998, Jalife et al. 1998b, Witkowsky et al. 1998]. We are aware of the quantitative limitations of 2D simulations of spiral waves and associated ECGs: the geometry and anisotropy of the ventricles can have an important influence on the dynamics of vortices and the electrical properties of the human body have to be taken into account. The AP heterogeneity addressed in the first chapter is also important for a correct description of heart repolarisation, e.g., in modeling the J and T waves of the ECG. The 2D spatial domain in which we study spiral waves is quite large compared to the size of the human heart (17.5 cm  17.5 cm). However, our computations show that once a spiral is formed, it can rotate in a medium as small as 8.2 cm × 8.2 cm. In the whole heart, spiral waves may be formed because of geometry and anisotropy.

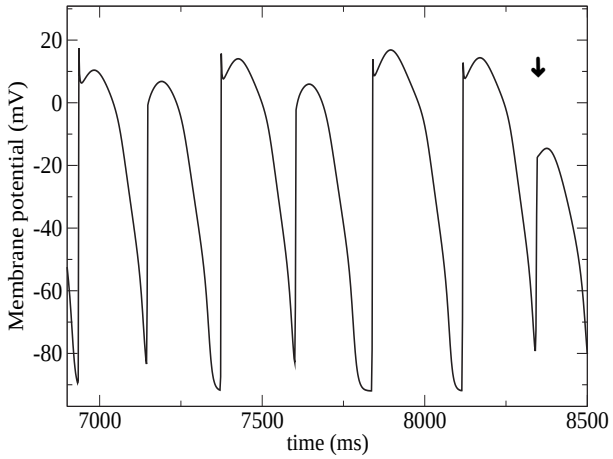


Figure III.13: Membrane potential recorded in the the point (325,325) near the site of the first effective wave break in the case of parameter set 3. Alternans between short and long $APD$ is observed before the wave break, indicated by an arrow.

### 4.2 Spiral wave breakup due to cromakalim

We obtained a complex activation pattern resembling VF and consisting of a varying number of chaotically wandering wavelets, by simulating the effects of an ATP-sensitive potassium channel opener, e.g. cromakalim. Uchida et al. showed that cromakalim shortened the refractory period and increased the rate of reentry in isolated canine hearts [Uchida et al. 1999]. It is well known that a shortening of the refractory period increases the ventricular vulnerability of reentry and our simulation results show that it can even destabilise reentry and cause VF.

The Fourier transforms show a broad peak with dominant frequencies around 5 Hz (Figure III.5). Experimental studies have however shown that the Fourier transforms of ECG during VF, have a well defined peak [Clayton et al. 1995, Jalife et al. 1998b]. We believe that this difference can be attributed to the effects of geometry and the relatively large size of the 2D medium, as simulations of complex activation in the human ventricular model gave well defined peaks in the Fourier spectrum (see chapter V).

### 4.3 A transition from complex patterns to organised activation

In the 2D simulations the application of a calcium channel blocker stabilised the wave pattern, however increasing the average frequency of activation from 6.0 Hz to 10.3 Hz. These simulation results qualitatively agree with several experimental and clinical studies on the effects of the class IV anti-arrhythmic drug verapamil : Chorro et al. found in Langendorff-perfused rabbit hearts that verapamil reduces the activation pattern complexity, despite an increase in dominant frequency from 14.4 Hz to 20.4 Hz [Chorro et al. 2000a,b]. Stewart et al. showed in vivo pig hearts that verapamil produced a significantly higher dominant frequency of fibrillation [Stewart et al. 1996],

while one case of near doubling of heart rate after intravenous verapamil was reported in a patient showing atrial fibrillation by Orlov et al. [1997].

We believe that the main mechanism for the reduction of the number of spiral waves, is the flattening of the electrical restitution curve as shown in Fig. III.9. During VF new spirals are formed via wave breaks, while spiral die when colliding with borders or coalescing [Qu et al. 1999]. By flattening the restitution curve, we gradually decrease the birth rate of spirals to a point where no new spirals are formed anymore, without affecting the process of "spiral death", until a steady state is reached. This was further supported by the observation that smaller blocks of $I_{Ca}$ that did not flatten $APD$ restitution enough, were not sufficient to stabilise the activation patterns (data not shown). The mechanism of preventing VF by flattening the restitution curve was also shown in experimental studies on dog hearts using verapamil by Riccio et al. [1999]. Garfinkel et al. studied the effects of bretylium on VF in pig hearts in experiment and in simulations in 3D slabs of cardiac tissue [Garfinkel et al. 2000]. They found that besides a significant increase of $APD$, bretylium flattens the slope of the restitution curve and can successfully either prevent VF or convert VF to VT. Since an increase in $APD$ is on itself considered to be antia-rrhythmic, they combined bretylium with an $APD$-decreasing drug and showed that this combination still could convert VF to VT, assessing the fundamental role of flattening the restitution curve. In our case, we have a similar situation: the block of $I_{Ca}$ decreases $APD$, which can be considered as proarrhythmic, and we do see an increased VF activity, if the reduction of $g_{Ca}$ is relatively small. If the block of $I_{Ca}$ becomes large enough, it flattens the $APD$ restitution curve, which overcomes the effect of $APD$ shortening and results in a stabilisation of the activation patterns.

Our results also show that the final number of spiral waves after the block of $I_{Ca}$ might depend on the boundary conditions: for periodic boundary conditions we obtained 2 spirals while for the no-flux boundaries there were 6 spirals (Figures III.6A and III.6B). In our view, this can be explained by the stabilising role of boundaries on spiral wave rotation. In fact, for the periodic boundary conditions the waves generated by each spiral can propagate in all directions and can therefore affect other spiral waves from all sides, while for the no-flux boundary conditions no waves are emitted by the boundaries and spiral waves interact with each other just from one side. This reduced interactivity can decrease the drift of spiral waves and therefore diminish their death rate via the annihilation route (Figure III.8B). It can also result in the formation of stationary rotating spiral waves close to the boundary, as we see in Figure III.6A. Note, however, that we did not study this process in details because of the limited applications of periodic boundary conditions in practice.

### 4.4 The influence of biphasic restitution

We found two types of spiral breakup in a model of human ventricular tissue with biphasic $APD$ restitution. The first type corresponds to previously studied breakup, where the positive slope of the restitution curve exceeds unity at low $DI$ [Qu et al. 1999]. The second type of breakup was observed when the negative slope became less than -1. In that case the breakup took a longer time to develop (up to 30 spiral wave rotations compared to 4 for the first type), which is similar to results obtained by Zemlin and Panfilov [2001]. We found that this second type of breakup was mainly due to a

substantial perturbation of the motion of the tip, when the steepness of the negatively sloped part of the restitution curve gets below -1. This irregular motion enhanced irregularities along the spiral arm via the Doppler-effect and eventually caused the wave breaks, similar to results obtained by Qu et al. [2000c] and Fenton et al. [2002] in models with monotonous restitution curves. The role of the tip motion was further confirmed by the lack of spiral breakup when a spiral wave was pinned around an unexcitable circular hole in the case of parameter set 3.

# IV

# Modified ionic models of cardiac tissue [Bernus et al. 2002b]

We have already discussed the advantages of FHN-like models. An important factor is the numerical efficiency. Obviously, the low number of state variables (two or three in FHN-models compared to 7-60 state variables in ionic models) allows faster simulations. However, there is another reason which becomes much more significant in 2D and 3D computations: in most FHN-models the ratio of the upstroke to the action potential duration is much smaller than in ionic models. Therefore, when FHN-models are scaled to reproduce propagating APs in cardiac tissue, their upstroke is longer in space and time. The consequence of a longer upstroke is clear from the following consideration: the computational time in 3D is inversely proportional to the 3rd power of the space step $\Delta x$ and to the first power of the time step $\Delta t$. Moreover, if one uses explicit numerical scheme for the evaluation of spatial derivatives there is another constraint, as the maximal $\Delta t$ is proportional to $(\Delta x)^2$ . Hence, the total numerical efficiency in 3D can be up to the 5th power of the spatial scaling. Because the main factor which determines $\Delta t$ and $\Delta x$ is the upstroke length, longer upstrokes in FHN-models allow to perform computations for space steps up to 1 mm and time steps up to 0.3 ms [Panfilov 1999], while the maximal acceptable scales in ionic models are of the order of 0.2 mm and 0.02 ms [Qu and Garfinkel 1999]. Increasing the maximal allowed space step in ionic models from 0.2 mm till for example 0.5 mm would have a lot of important consequences for possible use of these models in large scale computations.

In this chapter we investigate the possibility of using an intermediate class of models which, on one hand, retain a detailed description of ionic currents, but, on the other hand, have a longer upstroke, close to that of FHN-models. We start from the observation that in most ionic models the upstroke of the action potential is produced by the fast inward sodium current ($I_{Na}$). This current plays a key role in the transmission of excitation, while it has almost no influence on other important properties of cardiac tissue such as the shape of AP and the restitution of action potential duration. We present a method to modify $I_{Na}$ in such a way that it preserves its main properties, but reduces the steepness of the upstroke. We show that using such a procedure, a good numerical accuracy can be obtained at space steps up to 0.5 mm and more, keeping intact almost all properties of cardiac tissue, such as AP shape, restitution of $APD$ and of the conduction velocity. The description of all other ionic currents is unaltered. The presented technique is general and can be applied to any ionic model.

## 1 Modification of the fast sodium current dynamics

In general, we can say that ionic models of cardiac tissue consist of one partial differential equation for the transmembrane potential $V_m$, $N$ ordinary differential equations for gating variables and $M$ differential equations for ionic concentrations (e.g. [Luo and

Rudy 1994, Noble et al. 1998]). If we subdivide the gating variables into fast gates $f_i$ and slow gates $s_j$, we can write a typical ionic model for 1D cardiac tissue as:

$$\begin{cases} C_m \frac{\partial V_m}{\partial t} & = D \frac{\partial^2 V_m}{\partial x^2} - I_{fast}(V_m, f_i, C_k) - I_{slow}(V_m, s_j, C_k) \\ \frac{df_i}{dt} & = \frac{f_{i\infty}(V_m) - f_i}{\tau_{f_i}(V_m)} \\ \frac{ds_i}{dt} & = \frac{s_{i\infty}(V_m) - s_i}{\tau_{s_i}(V_m)} \\ \frac{dC_k}{dt} & = I_{ck}(V_m, C_k) \end{cases} \tag{1.1}$$

in which $C_m$ stands for the cellular capacitance per surface unit, $D$ for the diffusion coëfficient of the medium ($= \frac{1}{\rho \cdot S}$ with $\rho$ the cellular resistivity and $S$ the surface to volume ratio), $I_{fast}$ for the fast transmembrane currents active during upstroke (e.g. fast sodium current), $I_{slow}$ for the remaining transmembrane currents, $I_{ck}$ for the sum of the currents carrying a specific ion $k$, which concentration is denoted by $C_k$.

Our main aim is to slow down the dynamics of the fast processes of the model, while preserving the slow processes. Note, that because in most ionic models changes of concentration $C_k$ are slow, we will treat them in exactly the same way as slow gating variables and will omit these equations from our further considerations.

Let us introduce a parameter $\gamma_0$ in the following way :

$$\begin{cases} C_m \frac{\partial V_m}{\partial t} & = \frac{D}{\gamma_0} \frac{\partial^2 V_m}{\partial x^2} - \gamma_0 \cdot I_{fast}(V_m, f_i, C_k) - I_{slow}(V_m, s_j, C_k) \\ \frac{df_i}{dt} & = \gamma_0 \cdot \frac{f_{i\infty}(V_m) - f_i}{\tau_{f_i}(V_m)} \\ \frac{ds_i}{dt} & = \frac{s_{i\infty}(V_m) - s_i}{\tau_{s_i}(V_m)} \end{cases} \tag{1.2}$$

with $0 < \gamma_0 < 1$. We will further refer to (1.2) as the $\gamma$-model.

It is easy to see that if we consider system (1.2) during the upstroke ( the slow components of (1.1) and (1.2) will be inactive, i.e. $I_{slow} \sim 0$ and $\dot{s_j} \sim 0$), it can be rescaled to (1.1) by the simple transformations $T = \gamma_0 \, t$ and $X = \gamma_0 \, x$. Hence, the conduction velocity of a propagating pulse will be independent of $\gamma_0$, although the temporal and spatial duration of the wavefront will be longer in the $\gamma$-model than in the original. Note that during the upstroke, the $\gamma$-model is just a rescaling of the original model. All currents have exactly the same dynamics as in the original model, but with different time scales. For example, the net charge carried out by $I_{Na}$ during upstroke will be the same in both models.

The description of the fast currents (generally $I_{Na}$) also involves slower processes of inactivation and reactivation of the currents. In order to keep the dynamics uniformly scaled at the wavefront, we need to slow down these gate variables as well. However, keeping this slowed dynamics during the whole AP will affect the restitution properties of the fast currents and consequently, the restitution of conduction velocity. In order to avoid that, we slightly modify (1.2) as follows :

$$\begin{cases} C_m \frac{\partial V_m}{\partial t} & = \frac{D}{\gamma_0} \frac{\partial^2 V_m}{\partial x^2} - \gamma(t) \cdot I_{fast}(V_m, f_i, C_k) - I_{slow}(V_m, s_j, C_k) \\ \frac{df_i}{dt} & = \gamma(t) \cdot \frac{f_{i\infty}(V_m) - f_i}{\tau_{f_i}(V_m)} \\ \frac{ds_i}{dt} & = \frac{s_{i\infty}(V_m) - s_i}{\tau_{s_i}(V_m)} \end{cases} \tag{1.3}$$

with

$$\gamma(t) = \begin{cases} \gamma_0 & \text{during upstroke} \\ 1 & \text{at any other time} \end{cases} \tag{1.4}$$

The numerical implementation of this rule is trivial and will be discussed later.

We can now estimate the gain in computer efficiency obtained by introducing $\gamma_0$: if we use an explicit Euler scheme to evaluate the laplacian in (1.1), the accuracy of the numerical approximation depends on a factor $\frac{D}{C_m \cdot \Delta x^2}$, where $\Delta x$ is the space step. Because in (1.2) this factor becomes $\frac{D}{C_m \cdot \gamma_0 \Delta x^2}$ we can safely increase the space step by a factor $(\frac{1}{\gamma_0})^{1/2}$. Combining it with an increase in the time step $\Delta t$ by a factor $\frac{1}{\gamma_0}$ due to the slower dynamics, we obtain speedup factors $(\frac{1}{\gamma_0})^{3/2}$,$(\frac{1}{\gamma_0})^2$ and $(\frac{1}{\gamma_0})^{5/2}$, in 1D, 2D and 3D simulations. For $\gamma = 0.3$ this yields factors 6.08, 11.11 and 20.28. These theoretical predictions don't take the additional calculations due to $\gamma$ into account. We will however show, that the resulting speeding up is still considerable.

We introduced $\gamma$ in the reduced PB model for human ventricular tissue, with $I_{fast} = I_{Na}$, the fast sodium current, $f_i$ $(i = 1, 2)$ are the fast activation $m$ and inactivation $v$ of the sodium current. $I_{slow}$ denotes all the remaining currents.

## 2 Numerical approach

We performed simulations in 1 cell, a 1D cable, a 2D sheet of tissue (no-flux boundaries) and a 3D slab of cardiac tissue. We used the forward Euler method to integrate the set of equations at the cellular level. In 1D, 2D and 3D computations we used the operator splitting method to split the first equation of (1.1) into an ordinary differential equation (ODE) for the reaction part (transmembrane currents) and a partial differential equation (PDE) for diffusion. The PDE was solved using the forward Euler scheme, whereas for the ODE we used a time-adaptive forward Euler scheme with two possible time steps $\Delta t_{min} = 0.01$ ms and $\Delta t_{max} = 0.05$ ms. In this scheme, for each point of the medium the ODE is solved with $\Delta t_{max}$; if $\frac{dV_m}{dt} \leq 1$ V/s we move on to the next point, otherwise we integrate the ODE at that point 5 times with $\Delta t_{min}$ from its initial value. In the $\gamma$-model, we rescaled $\Delta t_{min}$ and $\Delta t_{max}$ by a factor $\frac{1}{\gamma_0}$. The relaxation equations for the gating variables were integrated using a technique presented by Rush and Larsen [1978] (Appendix B).
In 3D we introduced rotational anisotropy along the $z$-axis by assuming the fibers to lie in the $xy$-planes and rotating as a linear function of $z$. Note that, the divergence term $D\partial^2 V_m/\partial x^2$ in (1.1) and subsequent equations, becomes in three dimensions $\nabla D \nabla V_m$. We denote by $\theta(z')$ the angle between the fiber direction and the (fixed) $x$-axis in the $xy$-plane $z = z'$. We chose the ratio of the diffusion coefficient in the fiber direction $D_1$ to the diffusion coefficient in the transverse direction $D_2$ to be 9, in order to yield action potentials propagating three times faster along the fibers ($D_1 = \frac{1}{\rho S}$). By a rotation in the $xy$-plane of the coordinate system over an angle $\theta(z)$, we easily find the divergence term:

$$\begin{aligned}\nabla D \nabla V_m =& (D_1 \cos^2\theta(z) + D_2 \sin^2\theta(z))\frac{\partial^2 V_m}{\partial x^2} + 2(D_1 - D_2)\cos\theta(z)\sin\theta(z)\frac{\partial V_m}{\partial x}\frac{\partial V_m}{\partial y} \\ &+ (D_2 \cos^2\theta(z) + D_1 \sin^2\theta(z))\frac{\partial^2 V_m}{\partial y^2} + D_2 \frac{\partial^2 V_m}{\partial z^2}\end{aligned} \tag{2.5}$$

| Original model ($\Delta t = 0.01$ ms) | | $\gamma$-model ($\gamma_0 = 0.5$, $\Delta t = 0.02$ ms) | | $\gamma$-model ($\gamma_0 = 0.3$, $\Delta t = 0.033$ ms) | |
|---|---|---|---|---|---|
| $\Delta x$ (cm) | $CV$ (cm/s) | $\Delta x$ (cm) | $CV$ (cm/s) | $\Delta x$ (cm) | $CV$ (cm/s) |
| 0.009 | 70.0 | 0.013 | 70.0 | 0.017 | 70.0 |
| 0.010 | 69.5 | 0.015 | 69.5 | 0.020 | 69.7 |
| 0.015 | 67.9 | 0.020 | 68.2 | 0.025 | 69.1 |
| 0.020 | 65.8 | 0.025 | 66.9 | 0.030 | 68.5 |
| 0.025 | 63.4 | 0.030 | 65.6 | 0.035 | 67.9 |
| 0.030 | 60.8 | 0.035 | 64.1 | 0.040 | 67.3 |
| 0.035 | 56.2 | 0.040 | 62.8 | 0.045 | 66.5 |
| 0.040 | 52.7 | 0.045 | 60.2 | 0.050 | 65.5 |
| 0.045 | 49.3 | 0.050 | 57.2 | 0.055 | 64.9 |

Table IV.1: Numerical accuracy on the conduction velocity $CV$ in the original model and the $\gamma$-model.

Rotational anisotropy was achieved by following equation:

$$\theta(z) = \theta_0 + \frac{z}{z_{max}}(\theta_{max} - \theta_0) \tag{2.6}$$

where $\theta_0$ is the fiber angle in the plane $z = 0$, $z_{max}$ denotes the thickness of the slab and $\theta_{max}$ is the fiber angle in the plane $z = z_{max}$.
We used the normal value of $\rho = 180$ Ωcm, yielding a conduction velocity of 70 cm/s (in the longitudinal direction for the 3D simulations). For the $\gamma$-model, we obtained $\rho = 91$ Ωcm, for $\gamma_0 = 0.5$, and $\rho = 55$ Ωcm, for $\gamma_0 = 0.3$.

We implemented (1.4) by defining the upstroke as starting when $V_m$ crosses -30 mV ($dV_m/dt > 0$) and finishing when $I_{Na}$ is almost fully inactivated (inactivation variable $v < 0.0001$). The reactivation of $I_{Na}$ was therefore unaltered. In all simulations the space step was 0.025 cm in the original model and $\frac{0.025}{\sqrt{\gamma_0}}$ cm in the $\gamma$-models. The simulations were coded in C++ and ran on a Dell Precision Workstation 530 with two Intel Xeon 2.0 Ghz processors.

## 3 Numerical accuracy and action potential properties

### 3.1 Improvement of the numerical accuracy

The main reason for slowing down the dynamics of the upstroke, is to increase the numerical accuracy of cardiac ionic models or, in other words, to obtain the same degree of accuracy at larger step sizes. We investigated the numerical accuracy, by measuring the speed of a propagating pulse in a 1D cable at different step sizes. The results are shown in Table IV.1. We see that using a space step of 0.025 cm yields an error of about 10 % in the original model, while in the $\gamma$-models we have a 5 %, and 2 % error , for $\gamma_0 = 0.5$, $\gamma_0 = 0.3$ respectively. At a space step of 0.04 cm the original model shows an error of more than 25 %, while both $\gamma$-models have a deviation less than 10 %. It should be clear from these results, that the numerical accuracy has considerably been increased.

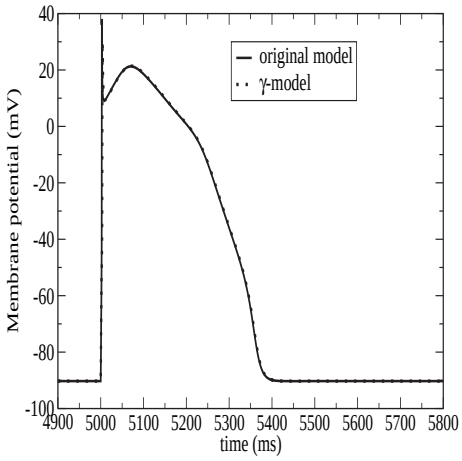


Figure IV.1: AP at 1Hz $BCL$ in the original model and the $\gamma$-model.

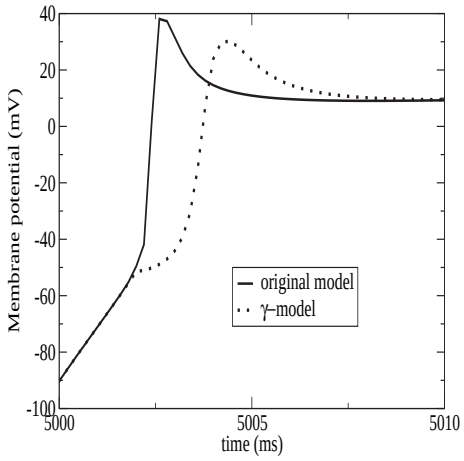


Figure IV.2: Upstroke of AP at 1Hz $BCL$ in the original model and the $\gamma$-model.

### 3.2 Action potential shape and restitution properties

First, we compared the AP shape in the original model and its $\gamma$-variant, by pacing a cell at a $BCL$ of 1 s with a stimulating current of 3 nA lasting for 2 ms. Figure IV.1 shows a superposition of the fifth AP in each model, while in Figure IV.2 a close-up on the upstrokes in each AP can be seen. The global shape of the AP is the same in the two models, whereas the upstroke has been slowed down in the $\gamma$-model, as expected. We obtained $APD$ restitution curve using the same S1-S2 protocol as in previous chapters. As can be inferred from Figure IV.3, it is clear that $\gamma$ has no influence on the $APD$ restitution properties of the cell. Note, that the same $APD$ restitution curve was obtained if $\gamma(t)$ was set to the constant value $\gamma_0$ (not shown).

$CV$ restitution was obtained by pacing one end of a cable of 20 cm at a gradually decreasing cycle length starting from 1 s down to conduction failure. We measured the speed of the pulses at the opposite side and plotted it against $BCL$. Figure IV.4 shows that the $\gamma$-model gives a close match with the original model, when (1.4) is taken into account. If $\gamma(t) = \gamma_0$ at all $t$, we see a large deviation at $BCL$ less than 500 ms, typical of cardiac arrhythmias. This deviation is due to the slowed reactivation of the fast sodium current, making it less available for a next activation. Hence, the propagation velocity decreases and conduction failure occurs at larger $BCL$. This result readily explains why we introduced (1.4).

### 3.3 The fast sodium current and wave propagation

We tested the influence of $I_{Na}$ on wave propagation in both models, by simulating a propagating pulse in a 20 cm long cable that was divided in two halfs: one consisting of normal tissue with sodium channel conductance $g_{Na}$= 16.0 nS/pF where the pulse was initiated, and the other consisting of tissue with reduced excitability ($g_{Na} < 16.0$ nS/pF). We ran several simulation, where $g_{Na}$ was gradually decreased in the second

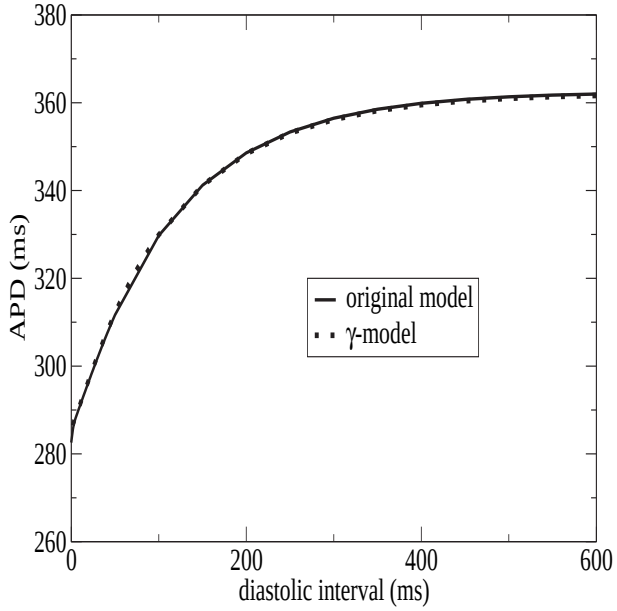


Figure IV.3: APD restitution in the original model and the $\gamma$-model.

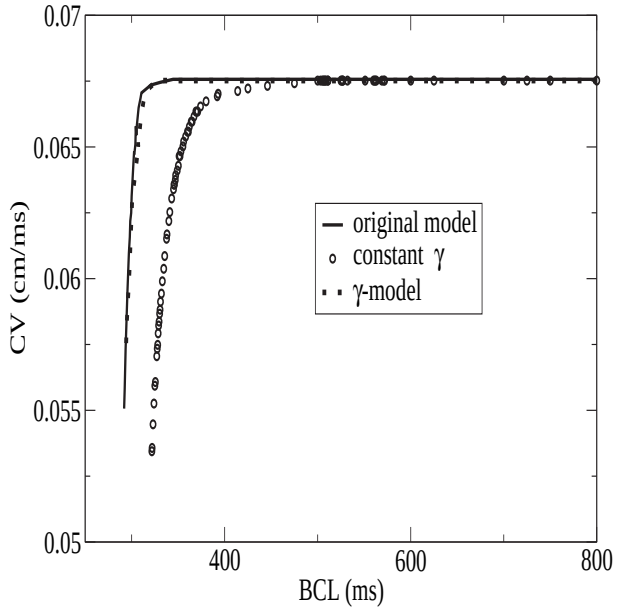


Figure IV.4: CV restitution in the original model, the model with $\gamma(t) = \gamma_0$ at all $t$ and the $\gamma$-model

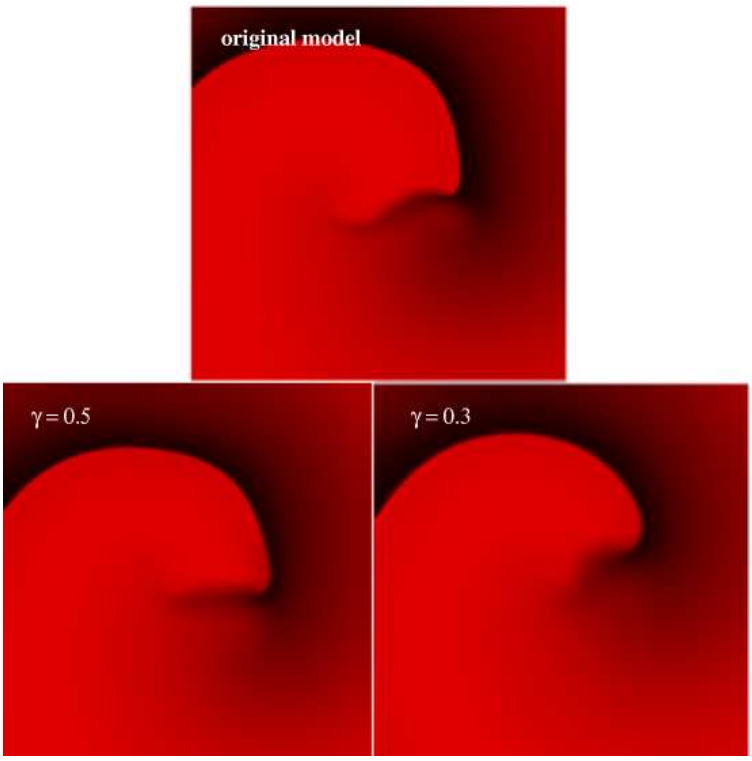


Figure IV.5: Stable spiral waves. Upper panel: original model. Lower panels : $\gamma$-model.

half of the cable (by steps of 0.1 nS/pF), until the AP failed to reach the other end of the cable. In the original model, this occurred for $g_{Na}$= 2.1 nS/pF, while in the $\gamma$-model conduction failure occurred at $g_{Na}$= 2.2 nS/pF, for $\gamma_0 = 0.3$. Below $\gamma_0 = 0.3$ the critical value for $g_{Na}$ increased, as it was 2.4 nS/pF for $\gamma_0 = 0.2$ and 2.7 nS/pF for $\gamma_0 = 0.1$. These results suggest that although the upstroke is slowed down, it has no significant influence on the excitation strength of the wave front for values of $\gamma_0 \geq 0.3$.

## 4 Dynamics of spiral waves in two-dimensional isotropic sheets

### 4.1 Spiral waves under normal electrophysiological conditions

We obtained spiral waves using an S1-S2 protocol in a two-dimensional 400 × 400 lattice (17.5cm × 17.5 cm), on which the model equations were integrated using methods discussed in previous sections.

As we showed in Chapter III spiral waves in the original model are stable and have a core with a diameter of about 5 cm and a period of 304 ± 3.1 ms (mean ± SD). The associated ECG has a similar period and shows a slight modulation of amplitude characteristic for polymorphic ventricular tachycardia.

We simulated spiral waves with the $\gamma$-model, for $\gamma_0 = 0.3$ and 0.5. In all simulations we obtained stable spiral waves with qualitatively similar dynamics and ECG. There were,

| | Original Model | $\gamma$-model | |
|---|---|---|---|
| | | $\gamma_0 = 0.5$ | $\gamma_0 = 0.3$ |
| core size (cm) | 4.8 | 4.4 | 3.2 |
| average period (ms) | 305.1 | 305.3 | 303.6 |
| ECG amplitude | 1.0 | 0.91 | 0.93 |

Table IV.2: Spiral wave properties in the original model and the $\gamma$-model

however, some quantitative differences compared to the original model, depending on the value of $\gamma_0$. Table IV.2 shows the core size, rotation period and ECG amplitude (scaled to 1 for the original model) of the simulated spiral waves in the different models. For $\gamma_0 = 0.3$ the $\gamma$-model has a comparable amplitude and time course of the ECG (not shown), the period of a spiral wave is close to that in the original model. The core size was decreased by 30 %, while for $\gamma_0 = 0.5$ the $\gamma$-model shows a close match with respect to all characteristics.

### 4.2 Spiral wave breakup in a 2D sheet of tissue

We investigated the role of $\gamma$ on the underlying electrophysiology during arrhythmias, by simulating the effects of cromakalim in a 2D medium with no-flux boundary conditions, like discussed in previous chapter. In the original model the spiral wave is destabilised and breaks up after a few rotations into multiple daughter spiral waves. We performed similar simulations with the $\gamma$-model, for $\gamma_0 = 0.3$ and 0.5. In both cases, the unstable behaviour of the original model could be reproduced in a qualitative way (Figure IV.6) Note, that although the wave patterns in Figure IV.6 look different, they do not indicate that differences between the models are large. As it was shown in [Panfilov and Holden 1991], the breakup patterns can differ substantially even in the same model due to the minor changes in the initial conditions, which is just an indication of the sensitivity of chaotic systems to the initial conditions. Therefore, it is natural to expect that the introduction of $\gamma$ will influence the chaotic patterns as well. More important for us, is that for studied $\gamma_0$ values we observed the breakup of spiral waves in the same parameter range. For $\gamma_0$ =0.5 the process of fragmentation and the ECG were very close to those in the original model. For $\gamma_0 = 0.3$, however, the initial fragmentation took a bit longer and the resulting ECG was slightly more regular (not shown).

## 5 Vortices in three-dimensional anisotropic media

We obtained vortices using an S1-S2 protocol in a three-dimensional 17.5cm $\times$ 17.5 cm $\times$ 0.5 cm lattice, on which the model equations were integrated, with $\theta_0 = 0$ and $\theta_{max} = \pi/6$.

We simulated vortices in the original model as well as in the $\gamma$-model with $\gamma_0 = 0.5$ and 0.3. In the three cases the vortices rotated with a period of approximately 300 ms. We plotted the trajectory of the filament in the planes $z = 0$ and $z = z_{max}$ for the three cases, during the first 4 rotations of the vortices. As can be inferred from Figure IV.7 the patterns are qualitatively similar, all showing a typical linear core. There were however some quantitative difference that became more pronounced as $\gamma_0$ decreased:

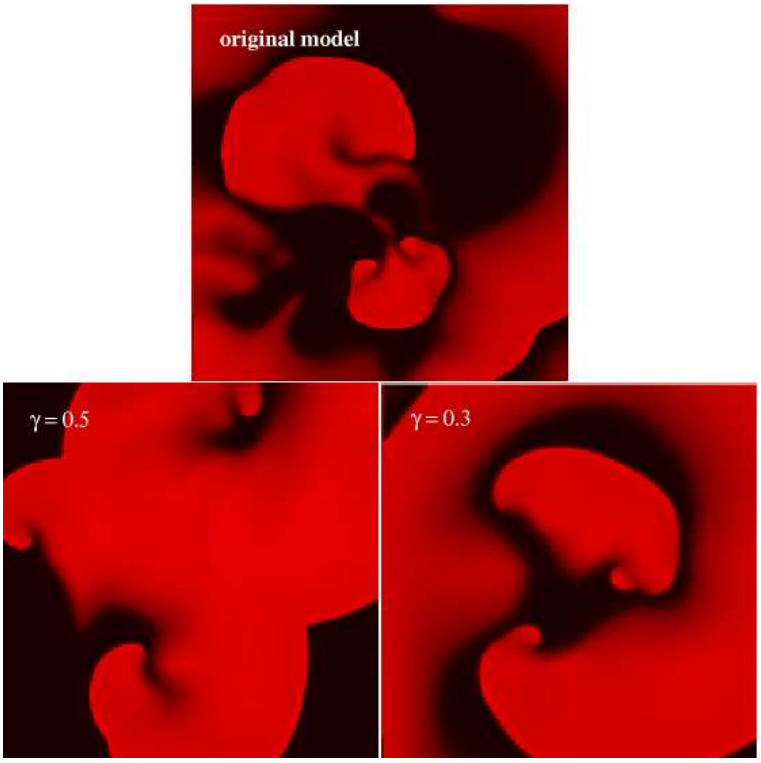


Figure IV.6: Spiral wave breakup due to cromakalim. Upper panel: original model. Lower panels : $\gamma$-model.

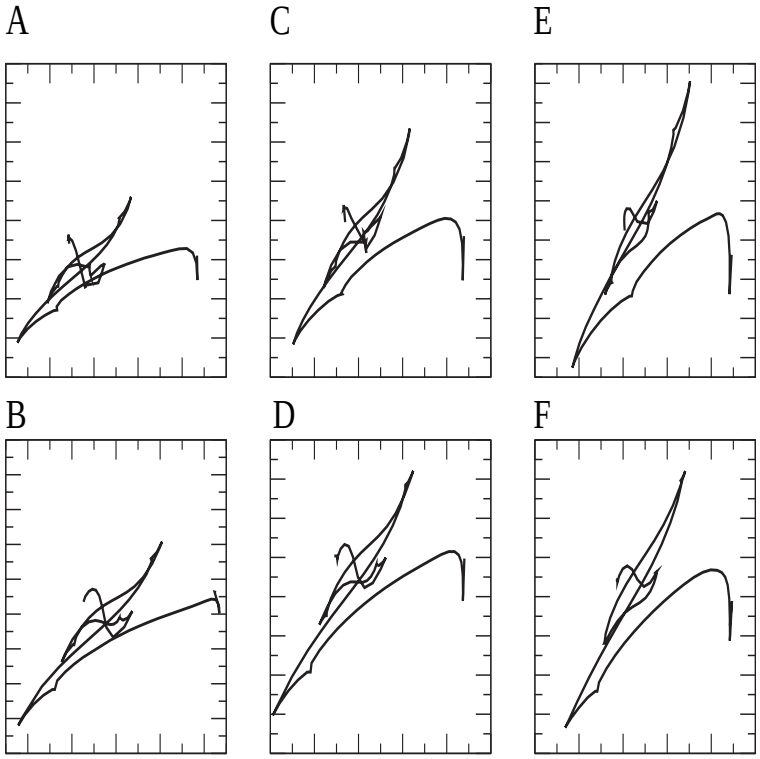


Figure IV.7: Intersection of the filament with the planes $z = 0$ (upper panels) and $z = z_{max}$ (lower panels) for the original model (A,B) and the $\gamma$-model with $\gamma_0 = 0.5$ (C,D) and $\gamma_0 = 0.3$ (E,F). The frames are 12.5cm by 2cm.

(1) the complexity of the pattern decreased as $\gamma_0$ decreased, where less sharp turns could be observed at the end of the linear parts of the core and (2) after the second rotation, the length of the linear part of the core becomes smaller as $\gamma_0$ became smaller, in the same amount as we observed in the 2D computations.

## 6 Computational time

We compared the computational time required for the simulation of 100 ms of a stable spiral wave in the original model and the variable $\gamma$-model with $\gamma_0 = 0.5$ and $\gamma_0 = 0.3$ in both 2D and 3D simulations. In the original model the 2D simulation finished in 653 seconds, while in the $\gamma$-model it took 190 seconds ($\gamma_0$=0.5) and 67 seconds ($\gamma_0 = 0.3$) of computational time. The calculations have been sped up by factors 3.4 and 9.7 for $\gamma_0$ = 0.5, respectively 0.3. In 3D the simulations required 48350, 9670 and 2686 seconds respectively, which yields speeding up factors of 5 and 18.1 for $\gamma_0 = 0.5$, respectively 0.3. These are slightly less than the predicted values in section 1 , but considerable, keeping in mind that the $\gamma$-model has one extra variable. Moreover, since the number of grid points involved has been reduced, the demand for computer memory has also decreased (by a factor $\frac{1}{\gamma_0}$ in 2D, and a factor $(\frac{1}{\gamma_0})^{3/2}$ in 3D).

# 7 Discussion

We have developed a model of cardiac tissue combining the advantages of the detailed ionic models and efficient FHN-like models. This was achieved by slowing down the dynamics of the wavefront in ionic models by a factor $\gamma_0$. As a result, we were able to rescale time and space steps used in simulations by factors $\frac{1}{\gamma_0}$ and $\frac{1}{\sqrt{\gamma_0}}$ respectively, without any loss in the description of the ionic machinery of cardiac cells.

We demonstrated the application of our method on a particular model of human ventricular tissue. However, because the description of the fast sodium current is similar in most ionic models, our method can be applied to all these models without any modification. Note that, the presented technique can be also applied to all models of excitable media which have fast and slow variables, for example to models of the Belousov-Zhabotinsky reaction [Jahnke et al. 1988].

We showed that modifying an ionic model with the presented method, doesn't affect the global shape of the action potential. The restitution properties, both with respect to action potential duration and conduction velocity, are preserved, as long as condition (1.4) is taken into account. Since the fast sodium current is the only current being reformulated, we investigated its property of sustaining wave propagation through tissue, in both models. Therefore, we measured the critical value for its conductance $g_{Na}$ below which conduction failure occurred in a cable. We found no significant difference between the original and the $\gamma$-model as long as $\gamma_0 \geq 0.3$. Note that, further decrease of $\gamma_0$ did affect the critical value of $g_{Na}$, which may indicate that too small values for $\gamma_0$ may decrease the reliability of cardiac propagation.

We investigated spiral waves in 2D simulations, comparing the original model with the $\gamma$-model. We obtained similar results, both for stable spiral waves as for spiral wave breakup. We found that the stable spiral waves behaved similarly in both the original model and in the $\gamma$-model, for $\gamma_0$ as low as 0.3. The only noticeable effect was a decrease in core size when decreasing $\gamma_0$. The ECG and period of the spiral waves were however almost unchanged. In the case of simulating the effects of cromakalim, we observed breakup of spiral waves in both models, although we found some minor qualitative differences in breakup patterns. We therefore believe that the $\gamma$-models are suitable for simulations of reentrant arrhythmias, as well as for simulating the effects of specific drugs on the stability of reentry in myocardium.

In 3D simulations of anisotropic slabs of cardiac tissue we found that the vortices rotated at similar pace. The meandering patterns obtained by taking the intersection of the filament with the outer $xy$-planes of the slab, were also similar with respect to shape in the original model compared to the $\gamma$-models with $\gamma_0$= 0.5 and 0.3. Again, we observed a decrease of the core size as $\gamma_0$ decreased.

Recently, several numerical methods have been developed to speed up computations of cardiac ionic models [Qu et al. 1999, Cherry et al. 2000]. These methods involve an adaptive discretisation of space and time, using small step sizes at upstroke and larger step sizes at other places and times. We used a time-adaptive method similar to the one developed by Qu et al. [1999], in the 1D, 2D and 3D simulations. Space-adaptive methods are however less straightforward to implement and still need to be developed for the complex geometrical structure of the human heart. Starting from any ionic model, a $\gamma$-model can easily be derived and a speedup of 10 in 2D computations (twice

as much as in [Cherry et al. 2000]) can be achieved, without modifying the numerical scheme. However, it should be worth investigating the use of $\gamma$-models in combination with space-adaptive schemes.

# V

# An anatomical model of the human ventricles

The human ventricular myocardium consists of interconnected cylinder shaped cardiac muscle cells, with a diameter of 10 to 20 $\mu$m and a length of 80 to 100 $\mu$m. These cardiac cells were shown to have more end-to-end connections than side-to-side connections [Hoyt et al. 1989], forming the so-called muscle fibers. As a result, the orientation of the cardiac muscle can be defined at any point as the local fiber direction. The fibers show a typical spiral arrangement throughout the ventricles from apex to base, with a counterclockwise rotation of the fiber direction from the epicardial to the endocardial surface. Moreover, the electrical conductivity is much higher along than across the fibers, making the myocardium highly anisotropic. Hence, the ventricular fibrous structure largely determines the pattern of electrical activation of the ventricles. Accurate reconstructions of both the ventricular geometry and fiber field orientation are therefore required for realistic modeling of the ventricular function.

The general features of the human ventricular fibrous structure are known since the 17th century [Lower 1669, Ludwig 1849], but it was only in the 1950s that quantitative studies of the fiber orientation were performed by Hort [1957], Thomas [1957]. Reviews of these studies can be found in Streeter [1979]. Several studies were also performed in different animal hearts [Streeter et al. 1969, Armour and Randall 1970, Greenbaum et al. 1981] and in general the following observations were made: a counterclockwise rotation of about 120° of the fibers through the ventricular wall. They also reported that the fiber orientation changed smoothly through the ventricular wall (compacta), but changed abruptly at the border between the compacta and the endocardial layer consisting of the trabecular tissue and papillary muscle.

Recently, [Nielson et al. 1991] developed a mathematical model of the canine ventricles based on the finite element method and including an accurate description of the fiber field, obtained by systematic measurements of the fiber orientation in the canine heart. This model was primarily developed for mechanical studies of the ventricles (contraction of the ventricles) and therefore, the geometry was idealised in order to reduce the number of parameters needed for the description of the model. This model has however successfully been used by several groups to study wave propagation during normal activation and reentrant arrhythmias in the canine ventricles [Panfilov and Keener 1995a, Panfilov 1998, Trayanova 2001].

In 1996 a computer model of the human ventricles was constructed by Hren [1996]. To our knowledge, it is to date the only model consisting of an accurate geometrical description of the *human* ventricles and showing a fibrous structure in agreement with the scarce experimental data available. Hren developed his model for the application to the study of ectopic activation by means of electrocardiographic recordings. As a model for the electrophysiological properties of the human ventricular tissue he used a hybrid type of equations consisting of a partial differential equation for the diffusion and a cellular automaton for the reaction (transmembrane currents). We wanted to

improve this model by using the ionic model we developed (see Chapter I) in order to be able to study reentrant arrhythmias and the influence of drugs thereon. R. Hren kindly provided us with his computer model of the anatomy and fibrous structure of the human ventricles, which is described throughout this chapter. We then incorporated the rPB model for the epicardial cells (isotropic ventricles) into the anatomical model and we validated the whole model by simulating normal activation patterns using the rPB tissue model and compared them with experimental data. Simulation results on reentrant arrhythmias using this ventricular model are discussed in the next chapter.

## 1 Surface harmonic expansion

Until today, there exist no accurate measurements of the local fiber orientation in the human ventricles. Therefore, Hren based his model on the canine model of the ventricular myocardium developed by Nielson et al. [1991], as the fibrous structure shows the same features as in the human heart, at least qualitatively. The problem of matching the human and canine ventricles, two highly complex objects, proved to be quite difficult. The approach followed by Hren to solve this problem consisted in reconstructing the principal surfaces that enclose the volume occupied by the myocardium from digitised anatomical data and by an appropriate matching procedure, to assign fiber orientation on these surfaces. The intramural fibrous structure can then be obtained as a function of the fiber orientation on the principal surfaces. The ventricular myocardium is however composed of two distinct structures: the compacta, with highly organised fibrous structure showing pronounced local changes (transmural rotation), and the trabeculata, whose fibers are arranged in a more uniform way and are independent of the organisation in the compacta. Moreover, the surfaces bounding the compacta are quite smooth, whereas they are quite complex for the trabeculata. Hren reconstructed the principal surfaces enclosing the compacta by means of the surface harmonic expansion, whereas the trabeculata were reconstructed by interpolation of the digitised data on the endocardial surface.

In general, a ventricular surface can be described by a vector $\vec{X}(\theta,\phi)$:

$$\vec{X}(\theta,\phi) = \vec{X}_0 + r(\theta,\phi)\begin{pmatrix}\cos\phi\sin\theta\\ \sin\phi\sin\theta\\ \cos\theta\end{pmatrix} \tag{1.1}$$

where $\vec{X}_0$ is the origin of expansion and the angles $\theta$ and $\phi$ are defined as in Figure V.1. The radial coordinate $r(\theta,\phi)$ of a point on a non-spherical surface can be represented using the spherical harmonic expansion [MacRobert 1967]:

$$r(\theta,\phi) = \sum_{n=0}^{\infty}\left\{a_n P_n(\cos\theta) + \sum_{m=1}^{n}(a_{nm}\cos m\phi + b_{nm}\sin m\phi)P_n^m(\cos\theta)\right\} \tag{1.2}$$

where $0 \le \theta \le \pi$ and $0 \le \phi \le 2\pi$. $P^n$ is the Legendre function of degree $n$ and $P_n^m$ is the associated Legendre function of degree $n$ and order $m$.

In numerical calculations of (1.2), the series is truncated at $n = N$. The ventricular surface is then uniquely determined by the origin of expansion and the set of coefficients $a_m, a_{nm}, b_{nm}$. The total number of parameters is $(N+1)^2+3$. These can be determined

by means of a least-squares fitting, once the ventricular surface is sampled at specific points, obtained from experimental techniques [Press et al. 1992]: for a given set of measured coordinates $\vec{X}_i$, $i = 1, \ldots, N_p$, the parameters can be obtained by minimising the quantity:

$$\sigma^2(\vec{X}_0, a_m, a_{nm}, b_{nm}) = \sum_{i=1}^{N_p} \left| \vec{X}_i - \vec{X}(\theta_i, \phi_i) \right|^2 \tag{1.3}$$

where

$$\theta_i = \arctan \frac{\sqrt{(x_i - x_0)^2 + (y_i - y_0)^2}}{z_i - z_0}$$
$$\phi_i = \arctan \frac{y_i - y_0}{x_i - x_0}$$

Hren used the Levenberg-Marquardt algorithm to minimise $\sigma$ in function of the parameters [Hren 1996, Marquardt 1963].

Using this method, one can smoothly fit the given surfaces to any desired degree of accuracy by choosing the number of parameters that characterise them. Finally, the tangential and normal vectors can be derived directly from equation (1.1), which will further be needed.

## 2 Construction of the ventricular model by Hren [1996]

The reconstruction of the human ventricular architecture can be described in several steps, in such a way that every new step added more details to the model without affecting the results of preceding step. The first step consisted in the accurate reconstruction of the principal surfaces. The second step was to identify the tangential planes to the fiber in each point of the volume bounded by the principal surfaces. In the third step the angle of fiber rotation $\alpha$ was assigned to each point of the principal human ventricular surfaces according to the corresponding angle on the principal surfaces in the canine ventricular model. In the next step the angle $\alpha$ was defined as a function of the depth (wall thickness) in consecutive layers between the principal surfaces. Finally, the trabeculata were added to the model. We now discuss in more details each of these steps (see also [Hren 1996]).

– **Assignment of the principal surfaces:** the volume occupied by compacta is bounded by four principal surfaces: 1) an epicardial surface separating the ventricular myocardium from the surrounding volume conductor, 2) a surface separating the compacta from the trabeculata or blood masses in the left ventricle, 3) a surface separating the compacta from the trabeculata or blood masses in the right ventricle and 4) a basal plane perpendicular to the long axis of the ventricles at the level of the mitral valve. The parameters of the surface harmonic expansion were evaluated for each surface separately. Using these parameters, the principal surfaces were reconstructed on a cartesian grid and represented as shells in the volume element (voxel) representation. Each voxel was allocated a byte in the memory storage and it was assigned a flag to identify on which surface it lied. The normals to the principal surfaces were calculated analytically in each voxel,

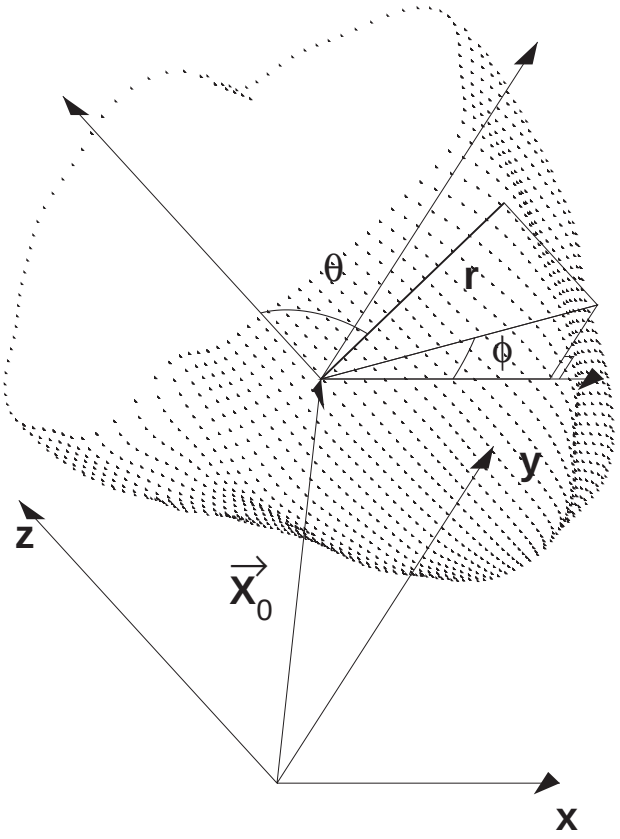


Figure V.1: Coordinate system for the surface harmonic expansion (taken from [Hren 1996]).

defining the local tangential plane to the surface. The normal to this plane was identified by spherical angles $\zeta$ and $\eta$ and stored in a byte format, with the angle $\zeta$ mapped into a byte from 0 to 127 and the angle $\eta$ from -127 to 127.

- **Assignment of tangential planes for intramural voxels:** the intramural voxels between principal surfaces were identified using a raster-filling algorithm, and then assigned their own $\zeta$ and $\eta$ as follows. The normals on the principal surfaces were calculated using lower-order harmonics to attain smoother surfaces. Then an iterative procedure was followed along the direction of the normal derived from the lower-order fit on the principal surfaces, with every subsequent iteration propagating deeper into the wall simultaneously from the endo- and epicardial principal surfaces. All voxels encountered along a given path were coded so that each voxel corresponded to a single voxel on the principal surface. The used algorithm is similar to a solution to the problem of finding the shortest path between the given voxel on the endocardial and epicardial surface, known from graph theory [Hadlock 1977].
- **Assignment of fiber direction on the principal surfaces:** the distribution of the fiber angles $\alpha$ on the principal surfaces of the canine ventricular model [Nielson et al. 1991] were mapped onto the principal surfaces of the human model using seven anatomical landmarks: 1) the left-ventricular epicardial apex, 2) the left-ventricular endocardial apex, 3) the right-ventricular epicardial apex, 4) the left-ventricular anterior papillary muscle, 5) the pulmonary outflow tract, 6) the anterior ventricular sulcus and 7) the posterior ventricular sulcus. The principal surfaces of the canine model were transformed into the principal surfaces of the human model by successively scaling the canine ventricles, first along the long axis and then in each short-axis slices. Scaling along the long axis was performed piecewise: the ventricular models were subdivided into four vertical sectors using the first five landmarks, after which the height of each sector in the canine model was scaled to match the height of the corresponding sector in the human ventricles. Scaling in the short-axis slices was performed by matching the axial positions of the ventricular sulci relative to the geometric center of each slice of the given principal surface.
- **Assignment of intramural fiber direction:** once the fiber orientation has been completely determined on the principal surfaces by the angle $\zeta$, $\eta$ and $\alpha$, the angle $\alpha$ can be assigned for the intramural voxels. To accomplish that, we assume that the transmural fiber rotation between the principal ventricular surfaces can be described by a smooth function $\alpha = f_{ijk}(\mu, e)$, where $e$ corresponds to the wall thickness. The endocardial voxel identified by the indices $(i, j, k)$ represents the origin of a piecewise-linear path $\mu$ that was defined along the vectors normal to the local tangential planes lying between the endo- and epicardial voxels. The distance $e$ between these two voxels and measured along the path $\mu$ represented the local wall thickness. Since the epicardium and endocardium are irregularly shaped, the distance $e$ varied through the ventricles and was a function of the starting endocardial voxel determined by the coordinate $(i, j, k)$. The function $f$ of transmural rotation can vary for different region of the ventricles, if required.
- **Incorporation of trabeculata:** since the bounding surfaces of the trabeculata on the interface with the blood masses can have very complex shapes, the bilinear interpolation method was used to reconstruct these surfaces. The tangential

Table V.1: **Fit of Principal Surfaces by Surface Harmonic Expansion**

| | rms Error [mm] | | | | Maximum Error [mm] | | | |
|---|---|---|---|---|---|---|---|---|
| *N* | EP | LE | SP | RE | EP | LE | SP | RE |
| 0 | 4.46 | 4.27 | 3.89 | 4.35 | 12.28 | 12.49 | 10.78 | 11.97 |
| 4 | 1.63 | 1.16 | 0.98 | 1.79 | 6.43 | 6.54 | 5.65 | 6.72 |
| 8 | 0.87 | 0.69 | 0.68 | 1.02 | 4.30 | 3.90 | 3.88 | 4.90 |
| 12 | 0.63 | 0.52 | 0.50 | 0.69 | 3.33 | 3.48 | 2.99 | 3.34 |
| 16 | 0.54 | 0.47 | 0.43 | 0.55 | 3.01 | 3.04 | 2.59 | 3.02 |
| 20 | 0.47 | 0.41 | 0.38 | 0.48 | 2.86 | 2.64 | 2.45 | 2.94 |

N, order of approximation

EP, epicardial surface

LE, LV endocardial surface

SP, RV septal surface

RE, RV free-wall endocardial surface

planes in the trabecular voxels were assigned by the algorithm propagating into the trabeculata along the directions determined by normals on the principal surfaces. The tangential planes thus defined may differ from the actual tangential planes of the voxels lining the right-ventricular and left-ventricular cavities. However, since the fibers in the trabeculata are oriented primarily in the apico-basal direction, the resulting imbrication angle should be very small.

The fiber rotation angle $\alpha$ of the trabecular voxels in the left-ventricular cavity were obtained as in Step 3, by the axial matching of canine and human ventricular models. This matching is an approximation as the trabecular surface was much more detailed in the human model than in the canine model. Since the trabecular structures were largely excluded from the right-ventricular reconstruction of the right ventricle in the canine model, the fiber orientation angle $\alpha$ was assumed to be 90° throughout the trabeculata.

## 3 Implementation of the ventricular model

The techniques presented in the previous section, were applied to anatomical data obtained from an excised structurally normal human heart. The procedures involved in preparing an anatomical specimen of the human heart have been described in detail elsewhere [Eifler et al. 1981]. The heart was positioned as in the thorax and sectioned transaxially at 1-mm slices; next, the boundary lines of the ventricular myocardium were carefully identified. In addition, the border between the compacta and trabeculata was determined by eye. The digitised data were then rotated into the coordinate system, with the $z$ axis coinciding with the ventricular long axis, defined as in Durrer et al. [1970]. The epicardial, LV endocardial, RV septal, and RV free-wall endocardial surfaces were represented by, respectively, 16872, 7310, 4348, and 3926 nonequidistantly distributed data points $(x_i,y_i,z_i)$.

The surface harmonic expansion method was then used to reconstruct the principal surfaces from these anatomical data. The accuracy of the approximation of the principal

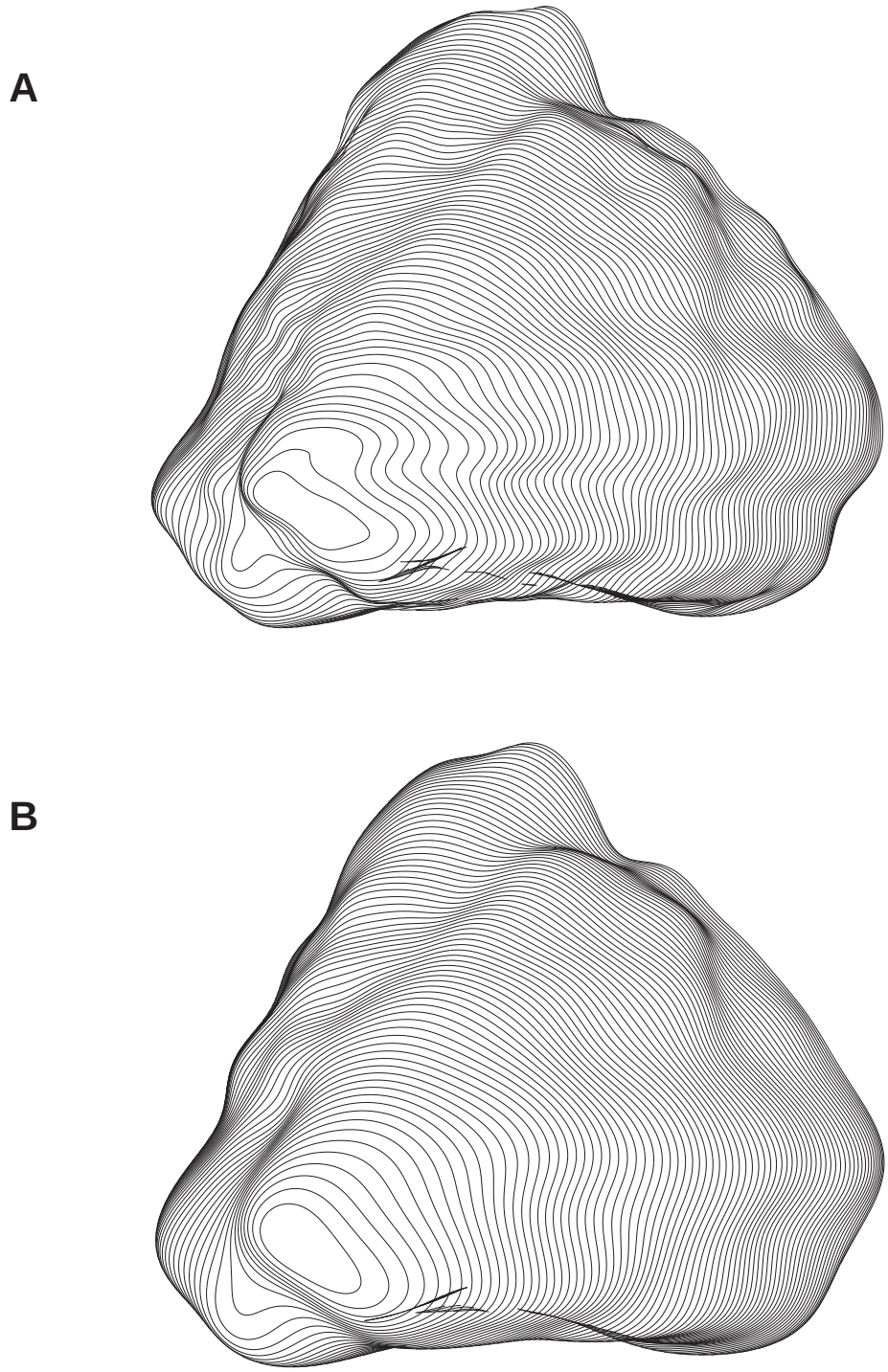


Figure V.2: The epicardial surface described by means of surface harmonic expansion for orders of expansion $N = 20$ (A) and $N = 12$ (B) (taken from [Hren 1996]).

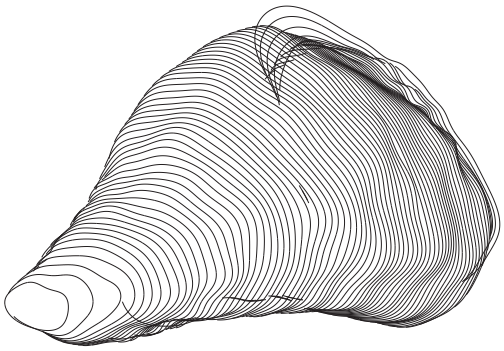

Figure V.3: The LV endocardial surface described by means of surface harmonic expansion ($N = 16$). Taken from [Hren 1996]

surfaces was quantitatively assessed by the root-mean-square (rms) error. Table V.1 shows the change of the rms error and maximum error with the order of approximation $N$ for the epicardial, LV endocardial, RV septal, and RV free-wall endocardial surfaces. The rms error decreased rapidly with the increasing number of lower-order harmonics, but this decrease eventually slowed down for higher-order harmonics ($N > 16$). There was almost no improvement in the solution (improvement in the rms error $< 0.1$ mm) beyond $N = 24$. With $N = 16$ or $N = 20$ (292 or 423 parameters, respectively), each surface could be described with an rms error $< 0.5$ mm; this error was acceptable for a model with a spatial resolution of 0.5 mm. Examples of the reconstructed epicardial and LV endocardial surfaces are shown in Figs. V.2 and V.3.

The reconstruction of the principal surfaces was performed as described in the previous section. The resolution of the model was 0.5 mm, so the volume of each voxel was 0.125 mm$^3$. During the construction of the model, the voxels were stored in a $220 \times 220 \times 220$ cube. The reconstructed epicardial, LV endocardial, RV septal, and RV free-wall endocardial surfaces consisted of, respectively, 106971, 46340, 23883, and 23903 voxels. The voxels on the epicardium were distinguished as RV and LV according to their location relative to the anterior and posterior ventricular sulci; 60088 voxels represented the LV epicardium and 46883 voxels represented the RV epicardium.

Figures V.4 to V.6 show epicardial views of the fiber orientation after matching the canine and human ventricular model as described in Step 3 of previous section.

The most important part of Step 4 was to make an appropriate choice of the function $f$. However, no quantitative study of the intramural fiber rotation in the ventricles of human hearts has as yet been reported. For these reasons, in the construction of the present model, the linear function $f$ was assigned for changes of the angle $\alpha$ in all intramural voxels, as was found by Nielson et al. [1991] for the dog heart. Figure V.7 shows the fiber orientation field in 18 Durrer's cross sections.

Finally, the incorporation of trabeculata was carried out as specified in Step 5 and where additional refinements of the model were performed, particularly when reconstructing the ridge-like structure of the basal part of the ventricles, which consists of the mitral,

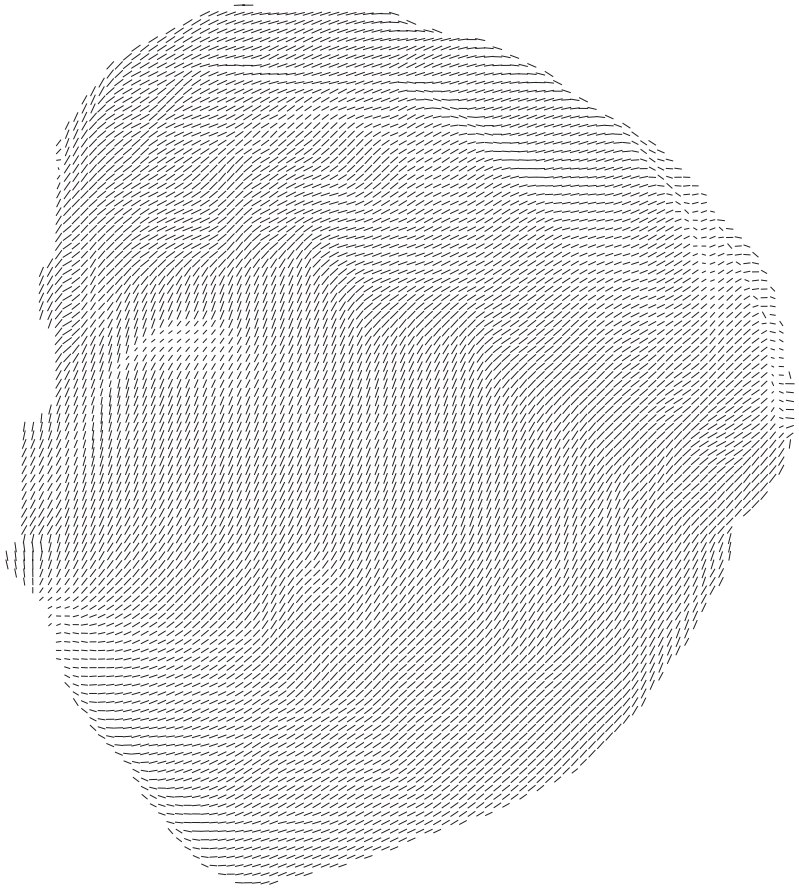

Figure V.4: Anterior view of the model of the human ventricular myocardium. The fiber direction is shown only in every second voxel along each axis (taken from [Hren 1996]).

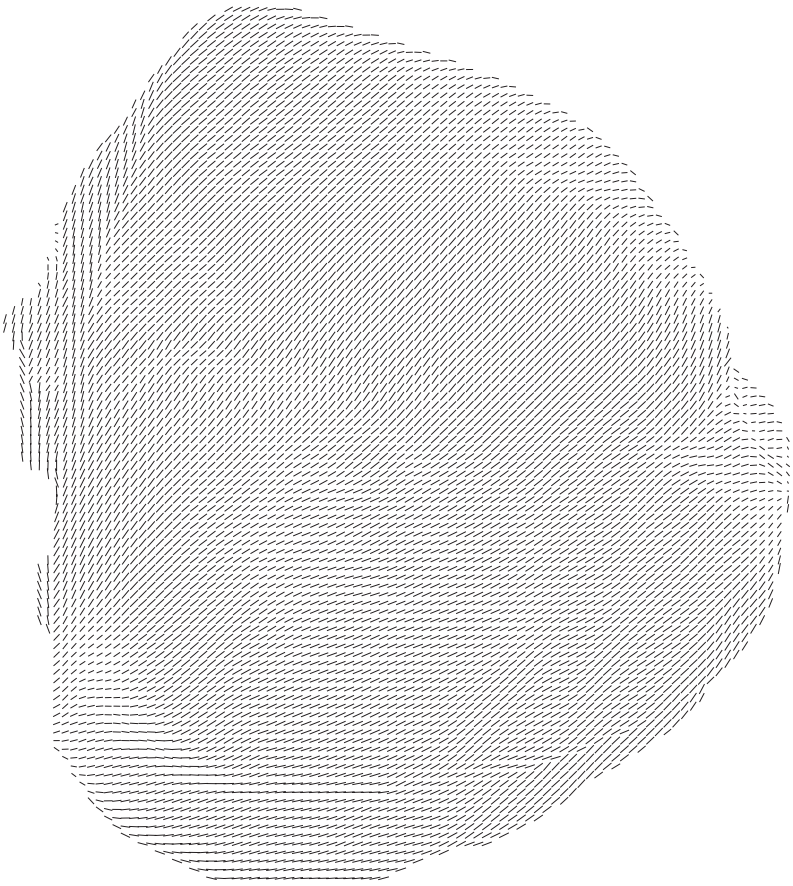

Figure V.5: Posterior view of the model of the human ventricular myocardium. The fiber direction is displayed only in every second voxel along each axis (taken from [Hren 1996]).

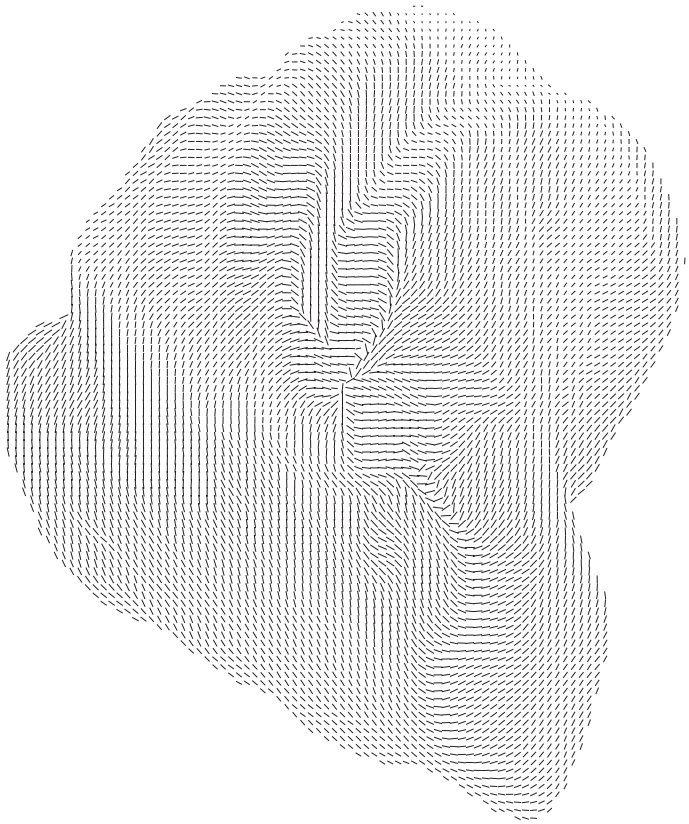

Figure V.6: Apical view of the model of the human ventricular myocardium. Only every second voxel along each axis is displayed (taken from [Hren 1996]).

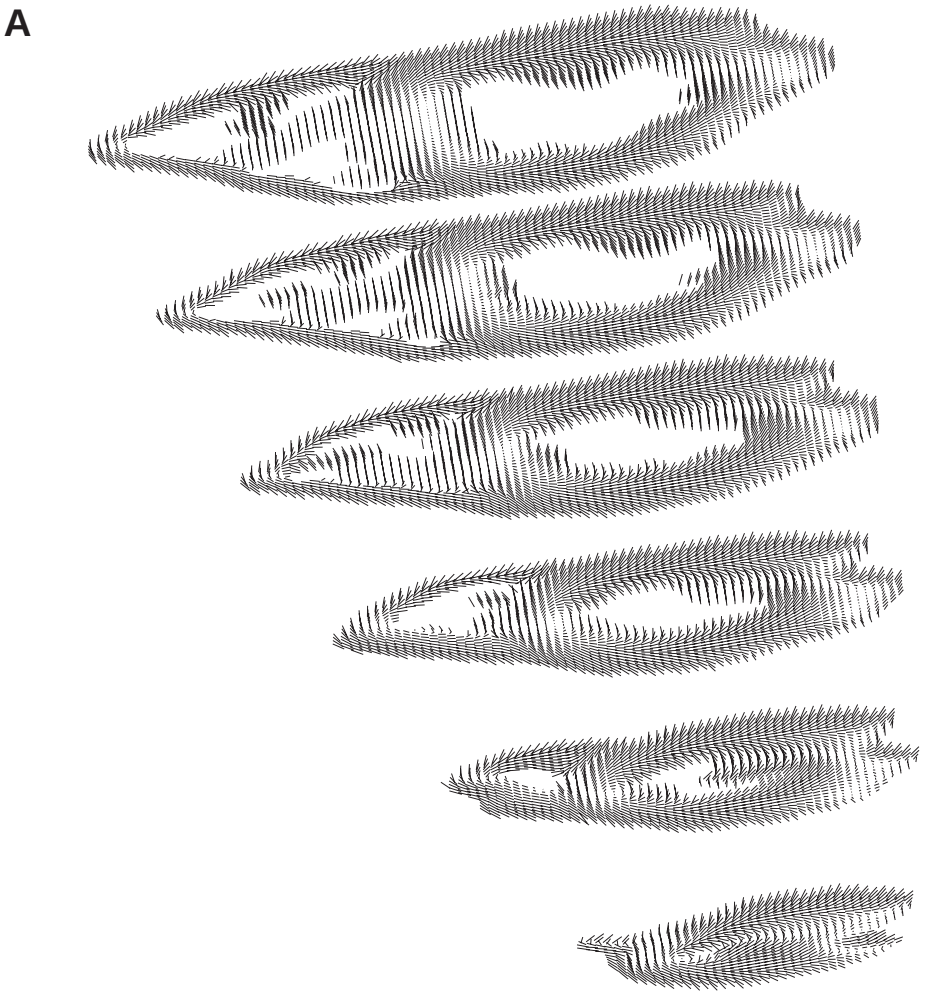


Figure V.7: Durrer's cross sections taken through the model of the human ventricular myocardium. The sections are 5-mm apart and perpendicular to the anatomical axis of the heart, as defined by Durrer *et al.*(1970); although the model's resolution is 0.5 mm, local vectors of principal fiber direction are shown on 1-mm grid to make the display clearer. (A) Apical sections are (from top to bottom) 32.5, 27.5, 22.5, 17.5, 12.5, and 7.5 mm above the left-ventricular apex. (B) Medial sections are (from top to bottom) 57.5, 52.5, 47.5, 42.5, and 37.5 mm above the left-ventricular apex. (C) Basal sections are (from top to bottom) 82.5, 77.5, 72.5, 67.5, and 62.5 mm above the left-ventricular apex. Taken from [Hren 1996].

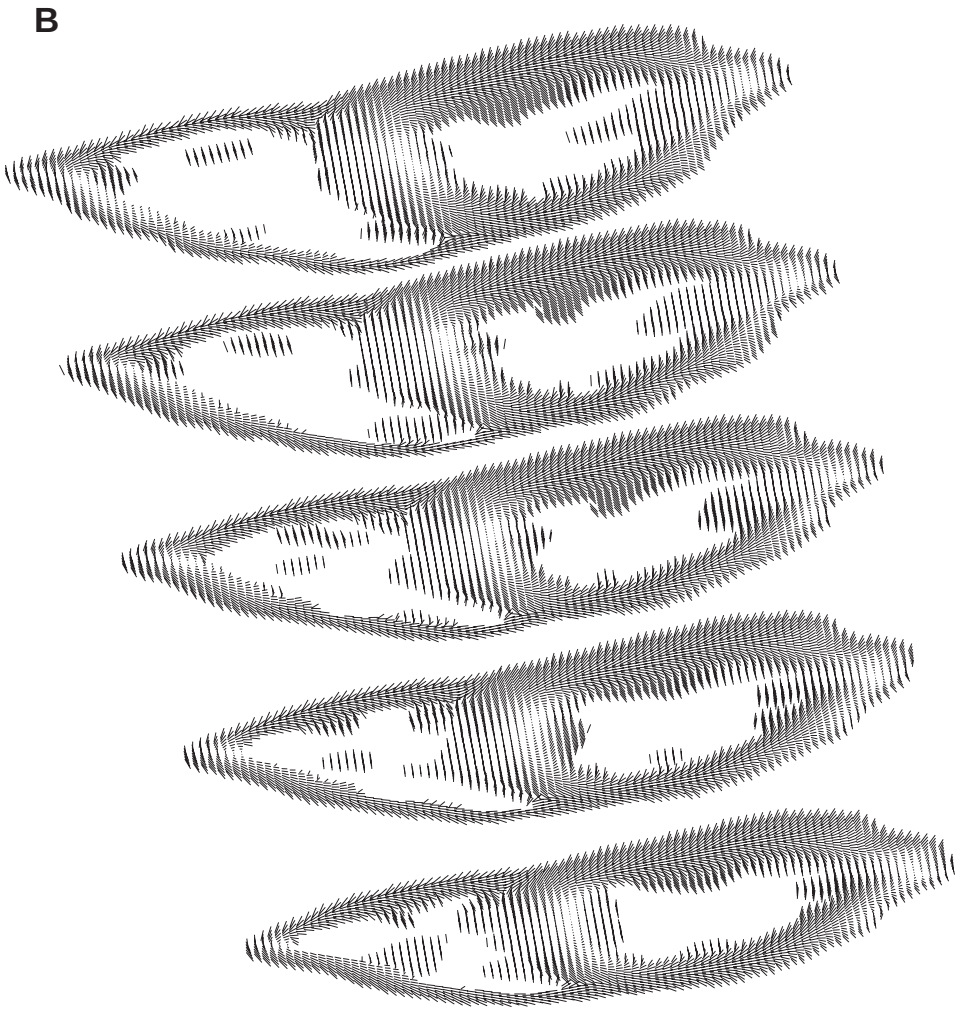
B

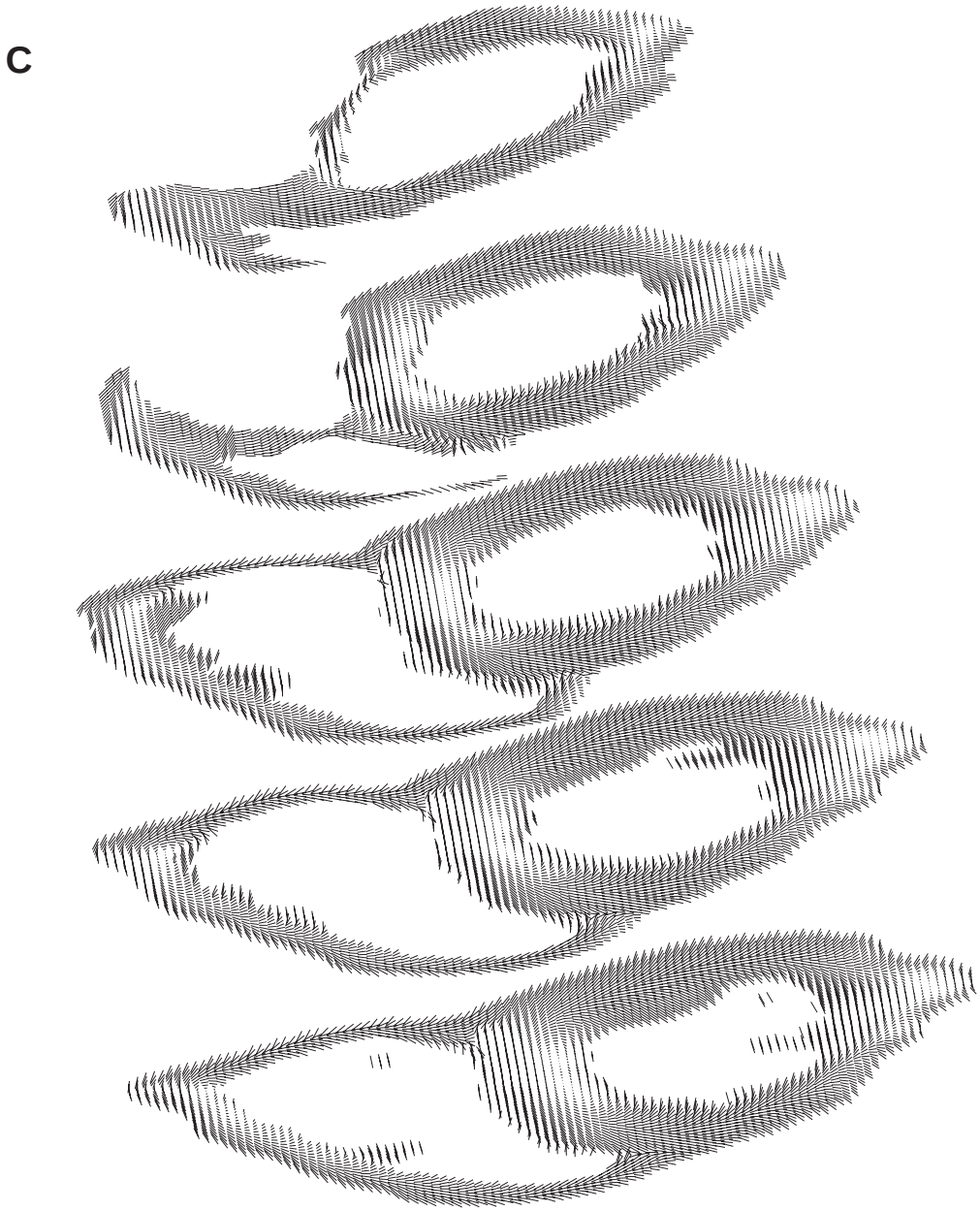
C

aortic, and pulmonary coni and has a complex shape.

## 4 Validation of the model by simulation of the normal activation pattern

In order to validate our model of the human ventricles, we wish to simulate normal activation of the ventricles and compare it to experimental studies [Durrer et al. 1970, Wyndham et al. 1979a,b, 1980]. Electrical impulses enter the ventricles via the atrioventricular node and are then conducted along the specialised His-Purkinje system to several sites in the ventricular endocardium. Hence, the simulation of the normal activation of the ventricles would require the incorporation of the His-Purkinje system into the anatomical model. Although Hren developed a simplified version of it [Hren 1996], we didn't implement such a conduction system and preferred to wait until more experimental data on the structure of the His-Purkinje system in the human ventricles become available. Normal activation patterns can, in this case, be obtained by stimulating simultaneously the connection sites (*insertion sites*) of the Purkinje fibers with the endocardial tissue.

The insertion sites were chosen by Hren in accordance with the experimental work of Durrer et al. [1970], Dam [1976], Wyndham et al. [1979a,b, 1980], Cassidy et al. [1984] and Vassalo et al. [1984]. In the left ventricle, the insertion sites were located in the high anterior paraseptal region, in the midseptum and middle anterior paraseptal region and in the lower posterior paraseptal region. In the right ventricle the insertion sites were selected at the base of the right-ventricular papillary muscle, at the midseptum opposite to the base of the right-ventricular anterior papillary muscle and at the base of the right-ventricular posterior papillary muscle.

Figure V.9 shows epicardial activation maps when simulating activation from the insertion site. We see that the bulk of the ventricles was activated within 100 ms (dark blue). The excitation pattern shows early breakthroughs on the right ventricular epicardium occurring at approximately 20 ms (Figure V.9A). On the left ventricular epicardium the earliest activation occurs in the paraseptal region at about 40ms (Figure V.9B). From these areas of early activation, a more or less radial spread of excitation was observed with the latest activation occurring in the basal regions, both for the right and left ventricle (Figure V.9A and Figure V.9C). These observations are in close agreement with experimental recordings of Durrer et al. [1970] and Wyndham et al. [1979a,b, 1980], in which the following general picture of normal activation was postulated: the epicardial activation starts with breakthroughs occurring at the anterior right ventricle about 20-25ms after the onset of activation. Then, three early areas of epicardial activation emerge in the left ventricle at about 30-35 ms and located on the anterior left ventricle close to the atrioventricular sulcus, on the anterior left ventricle halfway base to apex and on a posterior area in the lower middle of the left ventricles. The latest parts to be activated were mainly located at the base of the ventricles. With that respect, one can compare Figure V.9 with Figure V.10 taken from [Durrer et al. 1970] and see the close match.

The associated electrocardiogram of a single activation sequence is displayed in Figure V.11. It was recorded at 10 cm from the center of the ventricle in the transverse plane in the anterior direction. The QRS morphology resembles recordings from patients in lead

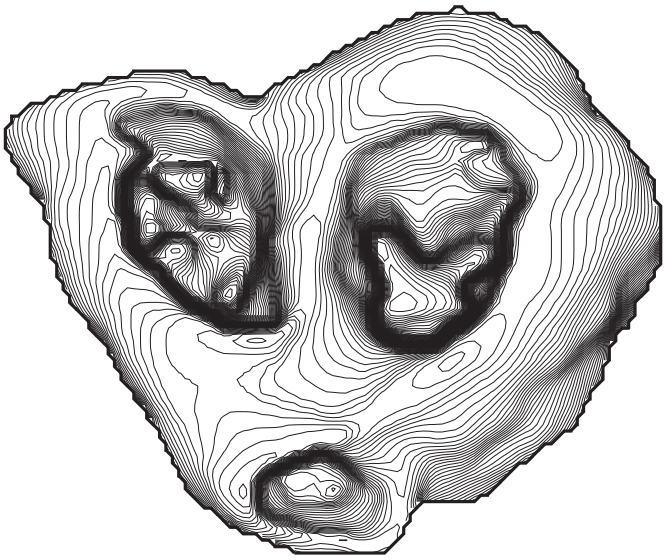

Figure V.8: Basal view of the geometry of the human ventricular model. Sections are 1 mm apart, and each is represented by smoothed contour lines ($z$ = const.). Taken from [Hren 1996].

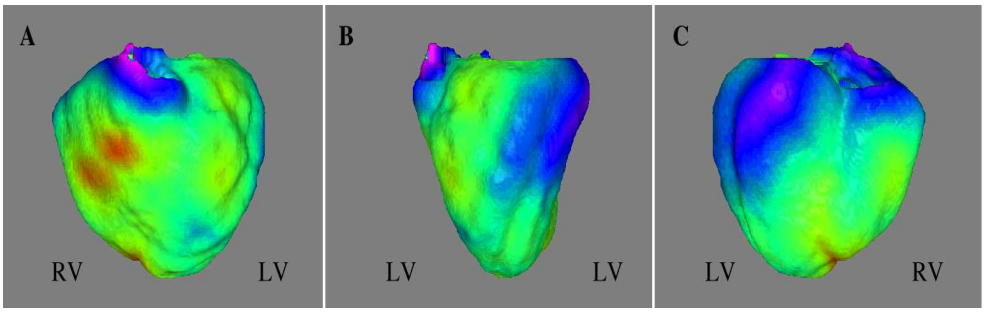


Figure V.9: Epicardial isochronal maps of activation of the ventricles from the insertion sites. Red denotes early activation (0 ms), while violet denotes latest activation (120 ms): (A) anterior view, (B) left lateral view and (C) posterior view.

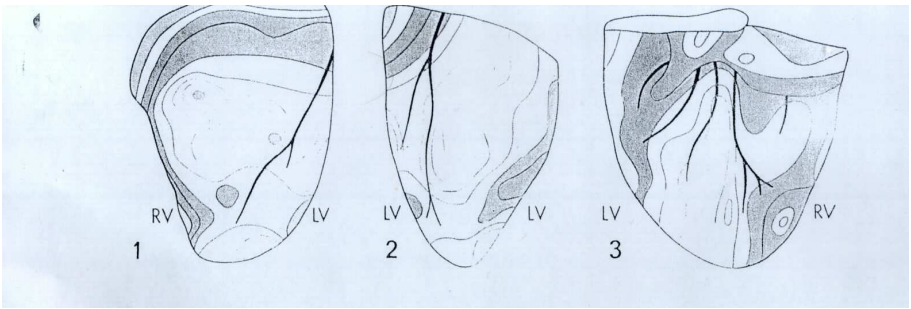


Figure V.10: Epicardial isochronal maps of activation of the ventricles from the insertion sites taken from [Durrer et al. 1970]: (A) anterior view, (B) left lateral view and (C) posterior view.

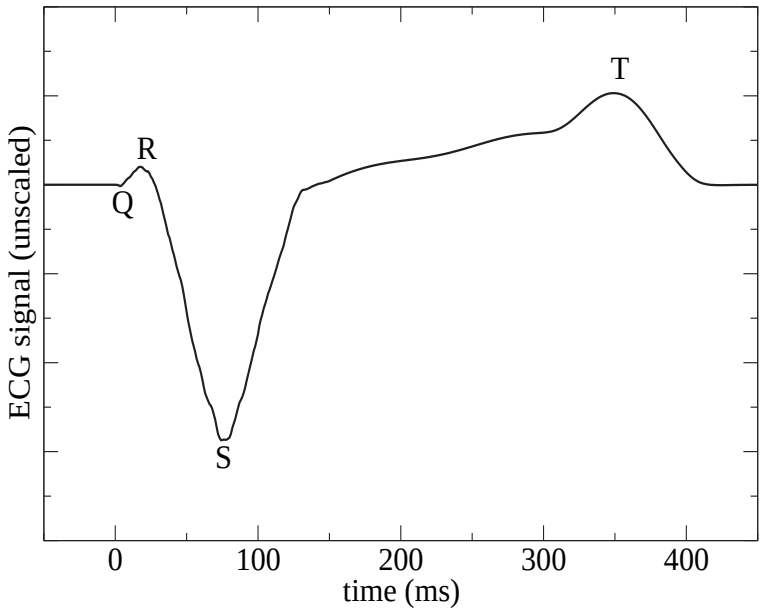


Figure V.11: ECG signal over one activation sequence of the ventricles. The Q, R, S and T waves are indicated.

V1 and V2 of a standard 12-lead ECG, with a pronounced S wave and a QT duration of about 350 ms.

## 5 Discussion

The model of the human ventricular myocardium features a very accurate description of the ventricular anatomy and fibrous architecture. In the absence of quantitative data on the human heart, Hren used as the source for local fiber direction a highly reliable model of the canine ventricular myocardium [Nielson et al. 1991]. The principal ventricular surfaces were accurately and efficiently parameterised by the surface harmonic expansion method, which provided a robust and compact basis for constructing the tangential sheets throughout the ventricles. The transformation between the principal surfaces of the canine and human models was guided by a set of anatomical landmarks.

Since the tangential planes were defined in the model of the human ventricular myocardium for any point between the epicardial and endocardial surfaces, the electrical and mechanical properties of the ventricular myocardium can also be assigned to vary with respect to the direction perpendicular to the tangential plane of fibers (i.e., the anisotropy can be defined as not axially symmetric). LeGrice et al. [1994] suggested that the ventricular myocardium is a discrete laminar structure with distinct anisotropic features in all three directions in space, i.e., in the direction along the fiber, in the direction perpendicular to the fiber in its tangential plane, and in the direction perpendicular to the tangential plane of the fiber.

Another issue in the accurate modeling of a fibrous structure such as the ventricles

is the selection of the function $f$ for the transmural rotation of the angle $\alpha$. Our model incorporates the feature that any smooth function $f$ can be defined between the endocardial and epicardial principal surfaces. However, to actually use such a feature in the model, we would need quantitative data collected transmurally in the ventricles of human hearts.

Although Hren's method of constructing the fibrous structure of human ventricles is simple, fast, and easy to implement, it has its limitations as well. First, the principal ventricular surfaces in the model are described by more parameters than in the model constructed by Nielson et al. [1991]. On the other hand, Hren's method combines the local and global features in the hierarchically organised model; in that way, depending on the given application, the amount of detail and specific ventricular structures may be included or excluded as desired. Secondly, the fibrous structure of the trabeculata and the most basal parts of the ventricles were reconstructed by means of rather heuristic *ad hoc* algorithms, and no attempt has been made to include a detailed description of the intramural rotation of fibers within the trabeculata. Such simplifications, however, may not be very important in light of considerable intersubject variability. Finally, the model can be improved by incorporating a small correction to account for the tipping of the fibers in the free wall out of the tangential planes ("imbrication" angle), provided the necessary anatomical data are available.

A major caveat of the anatomical model as presented here, is the absence of a conduction system, consisting of the His-bundle and the specialised Purkinje fibers network. Such a conduction system is important for the normal activation sequence of the ventricles, as its primary function is to spread activation over large portions of the ventricular endocardium simultaneously. We have however shown that we were able to reproduce normal activation patterns of experimental studies [Durrer et al. 1970, Wyndham et al. 1979a,b, 1980], by stimulating the insertion sites simultaneously, hence simulating the effects of a conduction system. This is also an indirect evidence for a realistic fiber field orientation throughout the ventricles. The conduction system has however been shown to play a non-negligible role during reentrant arrhythmias [Berenfeld and Jalife 1998]. We plan to investigate the influence of the conduction system on reentrant arrhythmias in a near future, by extending the model of Hren [1996] using a method developed by [Lieburg 1997].

# VI

# Reentry and fibrillation in the human ventricles

In this chapter we extend the results of chapter III to the anatomical model of the human ventricles. We begin by studying the stability of three-dimensional scroll waves induced at three distinct places in the ventricles. We then investigate the deterioration of stable scroll waves to turbulent patterns in the right ventricle by simulating the effects of a potassium-channel opener. Finally, we study the conversion from VF to VT by gradually blocking the calcium-channel in the model equations. The computations were performed using the $\gamma$-model (see chapter IV) with $\gamma_0 = 0.3$ and were run on a Dell Precision Workstation with 2 Intel 2.0 GHz processors. Comparable results were obtained with $\gamma_0 = 1.0$ (no $\gamma$ dependence) ran at the Netherlands National Computer Facilities in Amsterdam on grant SG-095.

## 1 Reentry at different locations in the human ventricles [Bernus et al. 2003a]

### 1.1 Reentry in the right ventricular free wall

In our first simulation we generated a single scroll wave in the right ventricular wall, using an S1-S2 protocol. Figures VI.1A-C show the different stages in the formation of the reentrant pattern. First, the S1-stimulus was applied in the posterior part of the right ventricle (Fig. VI.1A). Then we applied a S2-stimulus to the refractory tail of the S1-wave, in order to obtain a vast area of unidirectional block at a predefined site in the right lateral ventricular wall, parallel to the S1 wave back and with the base of the ventricles as a boundary (Fig. VI.1B). We see, that the S2-wave "curled" around this

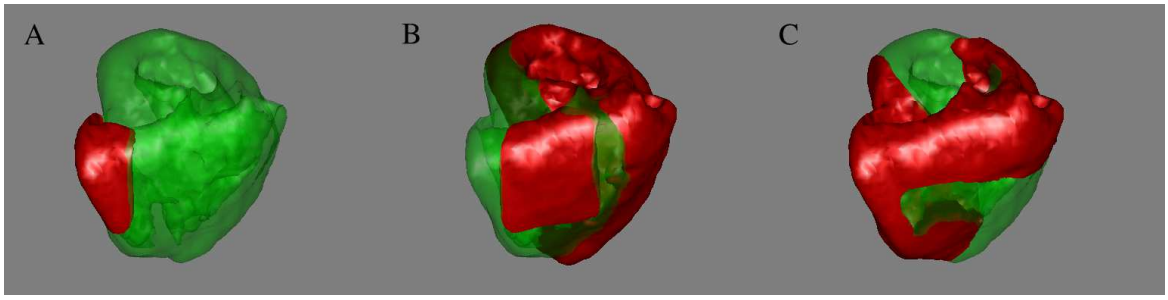


Figure VI.1: Formation of a simulated scroll wave in the right ventricular wall (right lateral view). Red denotes active cells, green quiescent cells defined at a threshold of -40 mV. (A) S1-stimulus, (B) S2-stimulus and (C) scroll wave.

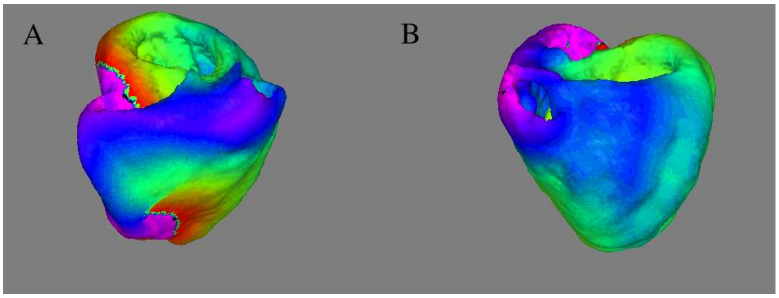


Figure VI.2: Isochronal maps of a simulated scroll wave in the right ventricular wall. Red denotes early arrival time (0 ms) and purple late arrival time (200 ms). (A) Spiral wave pattern on the right epicardial surface and (B) V-shaped collision area in the anterior left ventricle.

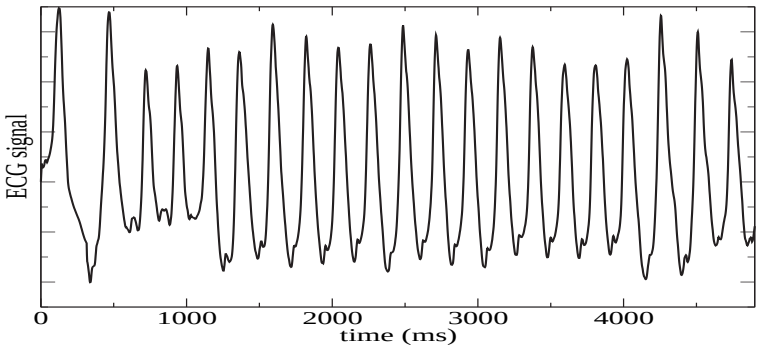


Figure VI.3: ECG of a single scroll wave in the right ventricular wall.

area of unidirectional block and formed a scroll wave in the right lateral ventricular wall (Fig. VI.1C).

We generated epicardial activation maps of this reentrant source from recordings of the arrival time of the wavefront in each point of the ventricles, during a time window of 200 ms (which is about the vortex rotational period). Figure VI.2A shows a right lateral view of epicardial activation. We see a reentrant source located in the free wall of the right ventricle close to the apex of the heart. The surface activation pattern has the shape of a spiral wave indicating that the source of excitation is a scroll wave. On the opposite side we see a typical V-shaped collision pattern (Fig. VI.2B). The ECG of this reentrant source shows a regular frequency of 4.5 Hz, with variations in amplitude and shape, typical of polymorphic ventricular tachycardia (Fig. VI.3). These amplitude variations are due to the meandering of the scroll filament within the ventricular wall [Bernus et al. 2002c,b].

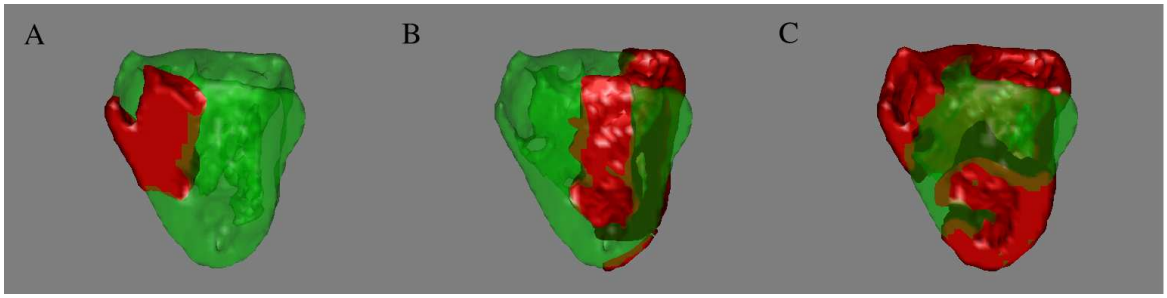


Figure VI.4: Formation of a simulated scroll wave in the septum (cross-section through septum). Red denotes active cells, green quiescent cells defined at a threshold of -40 mV. (A) S1-stimulus, (B) S2-stimulus and (C) scroll wave.

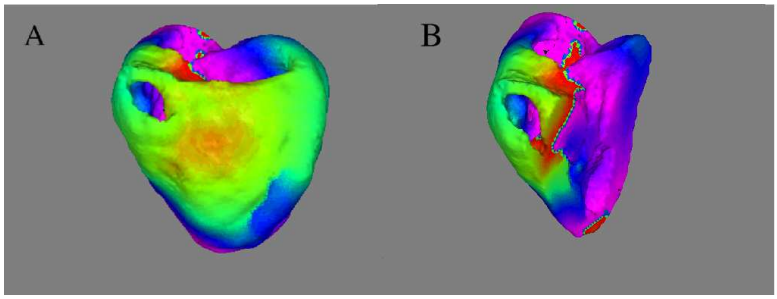


Figure VI.5: Isochronal maps of a simulated scroll wave in the septum. Red denotes early arrival time (0 ms) and purple late arrival time (200 ms). (A) Epicardial breakthrough in the anterior paraseptal region and (B) spiral wave pattern in a cross-section of the septum.

### 1.2 Reentry in the interventricular septum

In the next simulation we moved the stimulating electrodes to the septal region in order to initiate a vortex within the ventricular septum. We delivered an S1-stimulus in the anterior paraseptal region below the ridge-like structure around the pulmonary and mitral valve (Fig. VI.4A). The S1-wave propagated via the septum and the ventricular walls to the posterior side. We applied an S2-stimulus in the refractory tail of this wave, when it was halfway the anterior and posterior paraseptal regions (Fig. VI.4B). Just as in the previous simulation, a reentrant source formed and started activating the ventricles in a stable manner (Fig. VI.4C).

The epicardial activation map, obtained in the same way as in Fig. VI.2, displays a new feature: epicardial breakthrough patterns in the paraseptal region (Fig. VI.5A). These are the result of the waves emanated by the vortex in the septum, emerging on the epicardial surface. An activation pattern of the septum is also shown in a cross-section in Fig. VI.5B. The reentrant source was located near the anterior paraseptal region and the septal surface shows a spiral wave shaped activation pattern, indicating the presence of a 3D scroll wave. It showed almost no meandering, which could explain

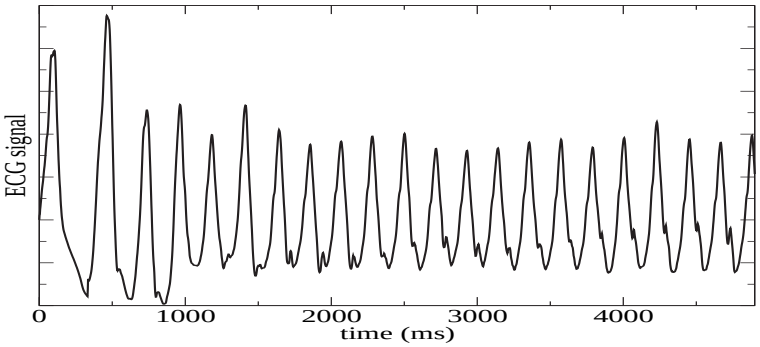


Figure VI.6: ECG of a single scroll wave in the septum.

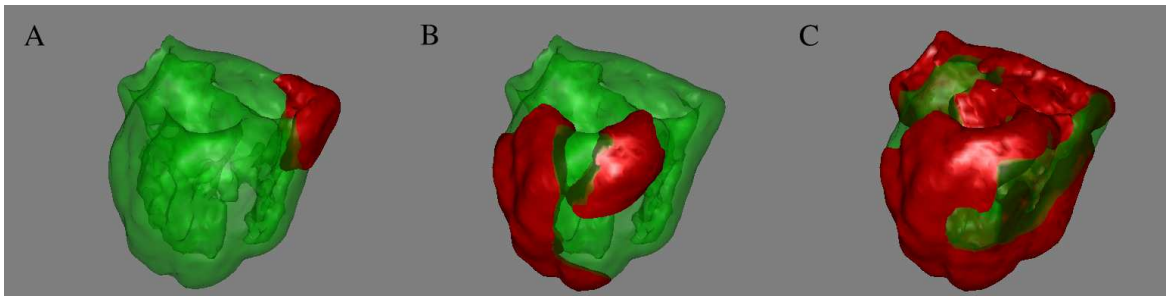


Figure VI.7: Formation of a simulated scroll wave in the left ventricular wall. Red denotes active cells, green quiescent cells defined at a threshold of -40 mV. (A) S1-stimulus, (B) S2-stimulus and (C) scroll wave.

the more regular ECG, which resembles monomorphic tachycardia. The period of this source was about 215 ms, which is the same as for the vortex in the RV.

### 1.3 Reentry in the left ventricular free wall

By applying an S1-stimulus at the posterior side of the ventricles (Figure VI.7A) and an S2-stimulus in the left lateral ventricular wall (Figure VI.7B), we obtained a vortex in the left ventricular wall (Figure VI.7C). This reentrant source showed however a complex drifting behaviour and occasional breakups were observed. This is illustrated in Figure VI.8 were isochronal maps are shown 2.5 seconds after initiation of the vortex. In Figure VI.8A we can clearly see that the spiral wave has drifted towards the paraseptal region and shows a broken wavefront. Figure VI.8B shows a cross section through the septum at the same moment, and illustrates the formation of a new scroll wave in the septum.

The recorded ECG shows a quite irregular shape (Figure VI.9) more typical of ventricular fibrillation than ventricular tachycardia.

We hypothesised that the unstable behaviour of the scroll wave in the left ventricle

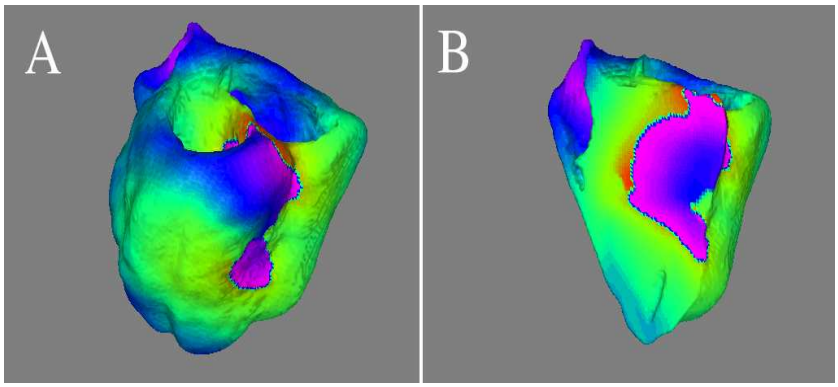


Figure VI.8: Isochronal maps of the simulated scroll wave initiated in the left ventricular free wall. Red denotes early arrival time (0 ms) and purple late arrival time (200 ms). (A) Epicardial view of the left ventricle and (B) cut-away section through the interventricular septum

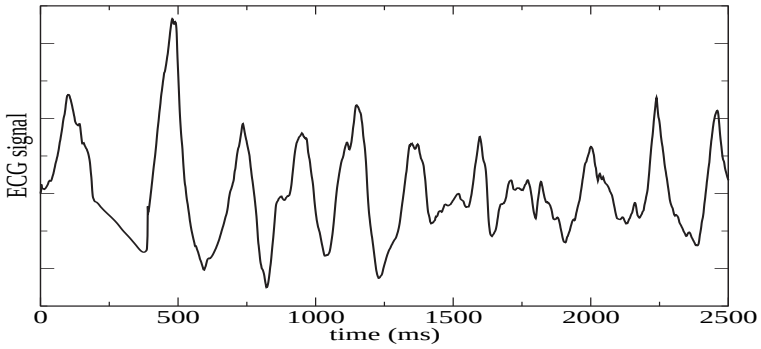


Figure VI.9: ECG of a single scroll wave in the left ventricular free wall.

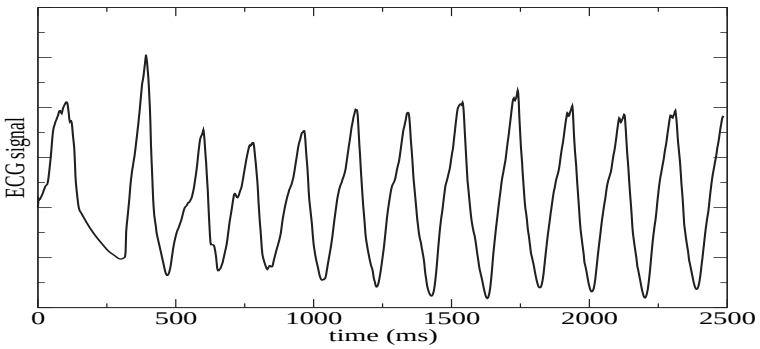


Figure VI.10: ECG of a single scroll wave in the left ventricular free wall in the isotropic case.

was due to the thicker left ventricular wall and hence to the more pronounced effect of rotational anisotropy, as was observed in previous simulation studies [Fenton and Karma 1998, Panfilov and Keener 1995b]. In order to check this hypothesis we performed the same simulation, but for the case of an isotropic heart, with a conduction velocity of 70 cm/s in all directions. In this case the scroll wave was very stable and rotated at a frequency of about 5Hz (Figure VI.10). We therefore believe that rotational anisotropy makes reentrant arrhythmias more prone to instabilities in the thicker left ventricular free wall than in the septum or the right ventricular free wall.

## 2 Complex activation due to a potassium-channel opener

In order to investigate the complex activation patterns during VF, we simulated the effects of an ATP-sensitive potassium channel opener (e.g. cromakalim) by increasing the extracellular potassium concentration to 5.4 mM and the conductances $g_K$ and $g_{K1}$ to 0.04 and 7.75 nS/pF respectively, as in the two-dimensional simulations of Chapter III. We generated a reentrant pattern by using the S1-S2 protocol in the right ventricle as described in previous section, and obtained an unstable vortex that broke down at several places, creating a complex activation pattern consisting of multiple wavelets (Figure VI.11). We showed in Chapter III that this breakup was due to a steep restitution over a large interval of DIs. After a few rotations breakup of the vortex occurred near the organising center in the right ventricular wall and as much as 6 daughter vortices were created by this process (Figure VI.12A). After 3 s the number of vortices was reduced to 3 (by coalescing spirals and collisions with the base of the ventricles). At that time 1 vortex was located in the paraseptal region of the left ventricular wall (Figure VI.12C) and the two others were in the right lateral wall (Figure VI.12B). Further wave breaks were unsuccessful in creating new vortices, as the free ends rapidly coalesced, but the vortices showed irregular meandering dynamics and activated the ventricles in a complex way.

The ECG signal computed for that case is shown in Fig.VI.13A. We see rapid changes of QRS morphology and amplitude of the signal, which are typical of clinical ECGs of VF. Fig. VI.13B shows the Fourier transform of the ECG. We see a well defined peak

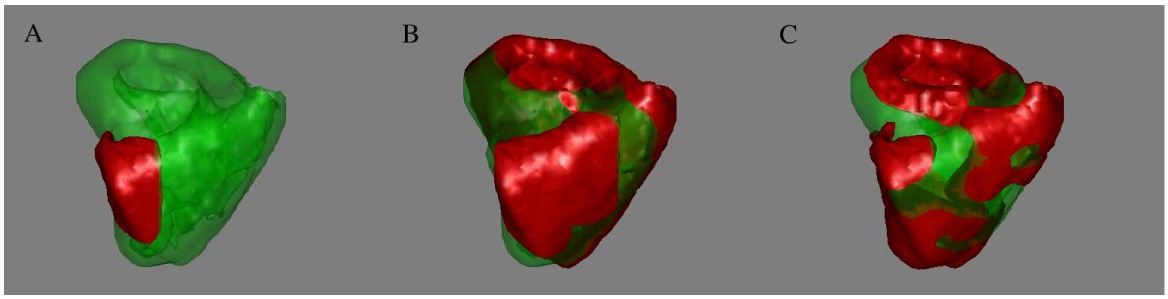


Figure VI.11: Simulated complex activity due to cromakalim induced by an S1-S2 protocol in the right ventricle. Red denotes active cells, green quiescent cells defined at a threshold of -40 mV. (A) S1-stimulus, (B) S2-stimulus and (C) complex activity.

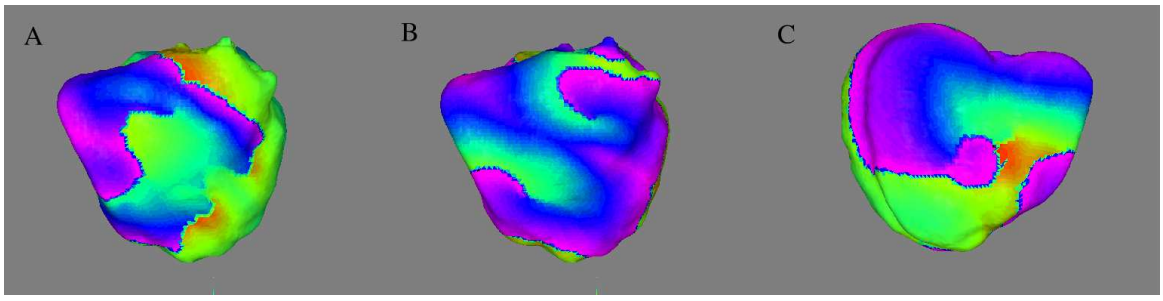


Figure VI.12: Isochronal maps of complex activity due to cromakalim. Red denotes early arrival time (0 ms) and purple late arrival time (200 ms). (A) Breakup of spiral wave on the right ventricular epicardial surface. (B) Right lateral and (C) posterior view of the heart epicardial surface 4s after S1-stimulus was delivered. Two spiral waves on the right ventricular epicardial surface (B) and a single spiral wave on left ventricular epicardial surface (C) can be clearly seen.

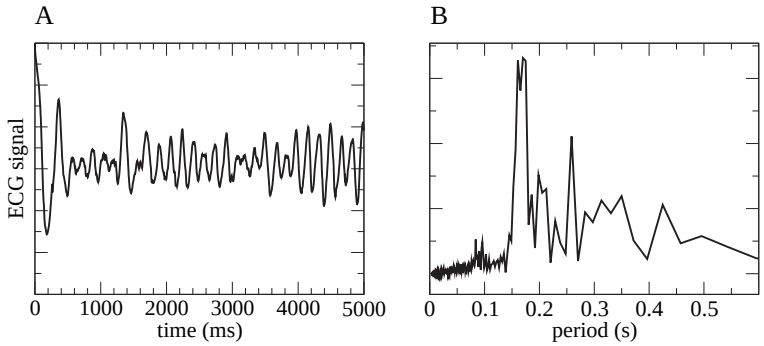


Figure VI.13: (A) ECG of the complex activity and (B) Fourier transform thereof.

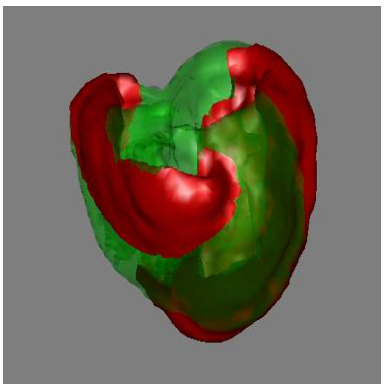

Figure VI.14: Electrical activity (red denotes activated cells) in the human ventricular model 5s after the application of a $Ca^{2+}$-channel blocker.

at approximately 180 ms. This is similar to the recordings observed in clinical studies by Clayton et al. [1995] and Jalife et al. [1998b].

## 3 Transition from ventricular fibrillation to ventricular tachycardia [Bernus et al. 2002a]

In this section we investigate how a calcium-channel blocker can convert turbulent activity in the human ventricles to organised patterns of activation. We performed simulations using methods described in detail in Chapter III. Four seconds after initiation of VF by simulating the effects of cromakalim, as discussed in previous section, we blocked 75 % of the calcium current (see (2.6) in Chapter 3 with $\tau = 1$ s and $p = 0.75$). After approximately 2.5 seconds the electrical activity became regular and a single spiral wave formed in the right ventricle. The spiral wave showed a transient drift and finally anchored to the basal ridge-like structure around the pulmonary valve. The electrical activity in the model of the human ventricles is shown at that moment in Figure VI.14. From then, excitation started circulating in a stable manner around

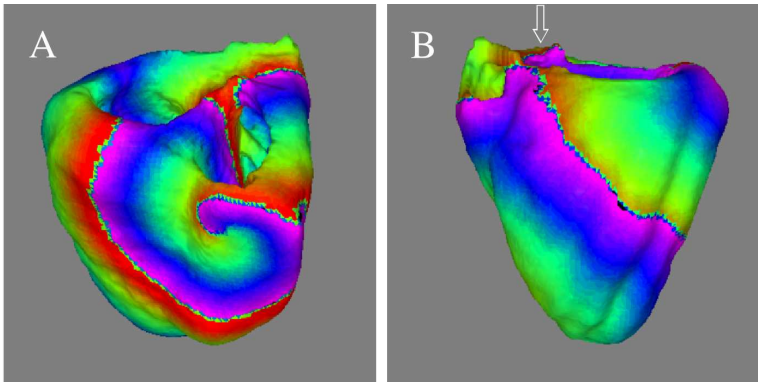


Figure VI.15: Simulating the effects of a $Ca^{2+}$-channel blocker on complex activation. Isochronal maps in the anatomical model of the human ventricles (A) 2.5s after application of the drug, where red denotes early arrival times (0 ms), violet late arrival times (150 ms) and (B) 5s after application of the drug, where red denotes early arrival times (0 ms), violet late arrival times (200 ms). An arrow indicates the basal ridge-like structure around the pulmonary valve.

it and the pattern persisted as long as the simulation ran. The dominant frequency at that time was reduced to 5.0 Hz. Isochronal maps of the electrical activity 2 seconds and 10 seconds after application of the drug are shown in Figures VI.15.

The recorded ECG is shown in Figure VI.16 where the different stages in the transition from VF to VT can be seen.

## 4 Discussion

We generated single and multiple reentrant activity by S1-S2 stimulation protocols at different locations in an anatomical model of the human ventricles.

We showed that single scroll waves can generate several features on the epicardial surface, such as V-shaped collision areas which were observed in theoretical [Panfilov and Marée 1997] and experimental studies as well [Jalife et al. 1998b]. When the source of excitation was located in the ventricular septum, we observed epicardial breakthroughs and no spiral patterns on the surface. These differences in activation patterns (V-shaped and breakthroughs) are general topological properties of the heart and can be potentially used to identify the location of the source of excitation in the heart, which is important for many clinical applications, e.g. for ablation of cardiac arrhythmias.

Single scroll waves have been associated with monomorphic ventricular tachycardia during which the heart is activated in a regular way, but at a high rate. Some simulations have shown that polymorphic ventricular tachycardia or Torsades de Pointes could be the result of drifting or hypermeandering scrolls in the ventricular wall [Winfree 1989, Gray et al. 1995b, Qu et al. 1999]. Our simulation results support this idea as we see that the ECG becomes more irregular when the meandering of spiral wave becomes more pronounced. This was especially observed in the case of a spiral wave in the left

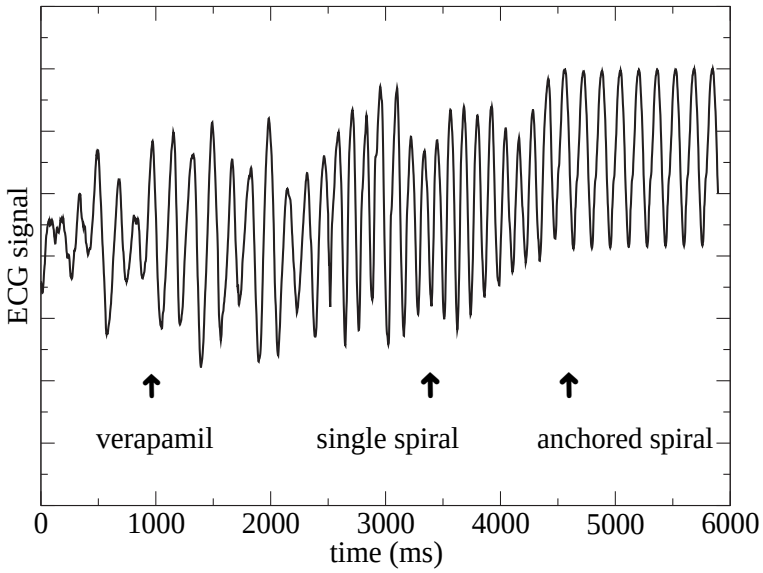


Figure VI.16: ECG recorded 10 cm from the center of the ventricles in the transverse plane when simulating the effects of a $Ca^{2+}$-channel blocker on complex activation. The different stages are indicated with arrows (see text).

ventricular free wall, which showed complex drift and occasional breakups. We found that the wall thickness and hence the rotational anisotropy played an important role in the stability of spiral waves in the ventricular model.

We were able to obtain VF by changing the electrophysiological properties of the ventricular tissue when simulating the effects of ATP-sensitive potassium channel openers. Our results show that during this complex activation only a small number of reentrant sources (from 3 to 6) are present in the ventricles, which supports experimental observations [Jalife et al. 1998b]. The ECG and its Fourier transform with a well defined peak are also closely related to recordings from patients [Clayton et al. 1995, Jalife et al. 1998b]. Note, however, that the mechanism responsible for the onset of VF in the human heart under normal conditions remains unknown. In our case single spiral waves did not spontaneously deteriorate into VF, when the properties of the tissue were normal.

Several experimental and clinical studies have shown that verapamil can, besides reducing the pattern complexity, also decrease the dominant frequency of activation and hence be an effective drug in the fight of VF [Samie et al. 2001]. In the anatomical model of the human ventricles, we found that after blocking the calcium channel a single spiral wave formed, which anchored to the basal ridges around the pulmonary valve after approximately 1.5 seconds and continued rotating at a frequency as low as 5.0 Hz. This decrease in frequency of activation after the spiral anchored is clearly seen on the ECG (Figure VI.16) and shows the main difference of the effects of a calcium-channel blocker in two-dimensional sheets of cardiac tissue or the human ventricular model (compare with results of Chapter III). The slower rate of activation at that stage is due to the longer activation path around the pulmonary valve, compared to the core of the

spiral wave. The observed anchoring is probably dependent on the initial conditions and might not occur in other simulations of VF. In those cases, a drug or a combination of drugs that flattens the APD restitution without decreasing overall APD, could prove useful in the conversion of VF to VT [Garfinkel et al. 2000].
Although the simulated ECGs show some qualitative similarities with recordings in patients, there are quantitative differences, which can probably be attributed to the use of simplified methods of ECG computation which do not include a torso model and use infinite medium potential approximations [Plonsey and Barr 1988]. The Fourier transform of the ECG in the model of the human heart shows a well defined peak, which is similar to recordings in patients during ventricular fibrillation [Clayton et al. 1995, Jalife et al. 1998b].

# VII

# Conclusion and outlook

## 1 Conclusion

Based on ideas used during the construction of a simple three-variable model, we introduced a six-variable model, which we called the rPB model, obtained by a reformulation of the Priebe-Beuckelmann model (PB) of a single human ventricular cell [Priebe and Breuckelmann 1998]. The results of the simulations show that the overall properties of the action potential in the original PB model are well reproduced in the rPB model: the shape of the action potential is similar in both models; the overall time course of the individual ionic currents resembled that in the original model; the reformulated model closely fits experimental data of the $APD$-restitution curve obtained by Morgan et al. [1992a]. Moreover, we were able to reproduce the experimentally observed action potential heterogeneity in the ventricular muscle. The reformulated model is 4.9 times faster for numerical computations and it is more stable than the original model.
We have also developed a method to obtain biphasic restitution curves in ionic models of cardiac tissue, by introducing a new variable and modifying the kinetics of the L-type calcium channel. We have applied this method to the rPB model and showed that it can be used to reproduce experimentally obtained restitution curves by Morgan et al. [1992b].

The numerical accuracy of the models plays an important role in the computational speed of such models. This numerical accuracy is mainly determined by the steepness of the upstroke, which determines at which space and time steps a model can be numerically solved. The steeper the upstroke is, the smaller these steps have to be chosen, and the longer computations take. Unfortunately, most ionic models show a very steep upstroke. By modifying the kinetics of the fast inward currents in ionic models of cardiac tissue, we were able to reduce the steepness of the upstroke without affecting the other properties of the action potential such as its shape and restitution. For this purpose a parameter $\gamma$ was introduced in the equations to slow down the fast processes occurring over an action potential. The resulting model was called the $\gamma$-model. By doing so for the rPB model, we were able to increase the space step from 0.25mm up to 0.5mm, and more, which yielded a speedup factor of about 20 in three-dimensional computations.

We have developed an anatomical computer model of the human ventricles, by using anatomical data obtained by Hren [1996]. This data consisted of voxel representation of the ventricular anatomy of a human heart, with the fiber orientation fitted in each voxel from [Streeter 1979, Nielson et al. 1991]. We have incorporated the rPB model and its $\gamma$-variant in this anatomical model, in order to simulate excitation patterns in the human ventricles, and we have validated the model by comparing normal activation patterns with experimental data obtained by Durrer et al. [1970].

We have applied the developed models to the study of reentrant arrhythmias in two-dimensional sheets of cardiac tissue and in the model of the human ventricles.

For the normal parameter set we have found stable spiral waves in 2D which rotate around a linear core with diameter of about 5cm, and with a frequency of 3.5Hz. In the human ventricles we found stable vortices in the right ventricular free wall and in the interventricular septum, whereas a vortex initiated in the left ventricular free wall showed a complex meandering behaviour and occasional breakups. We believe that the rotational anisotropy, which is much more pronounced in the left ventricle, plays a non-negligible role in these different spiral wave dynamics.
We simulated the effects of a potassium channel opener, e.g. cromakalim, on spiral waves. In 2D and in the human ventricles, the rotors broke up spontaneously after a few rotations and a turbulent pattern set in. In the two-dimensional sheet of ventricular tissue, the number of spiral waves varied between 2 and 70 during this fibrillation-like pattern, whereas in the human ventricles only 3 to 6 distinct rotors were observed. Moreover, the Fourier transform of the calculated ECGs showed a fractionated spectrum in the case of the two-dimensional simulation, whereas it showed a single dominant frequency of about 5.5Hz in the anatomical model of the human ventricles, which is typical of recordings from patients [Clayton et al. 1995, Jalife et al. 1998b].
We have investigated the influence of the class IV anti-arrhythmic drugs (calcium channel blockers) on the turbulent patterns obtained after simulation of cromakalim. In 2D we found a transition to a stable state consisting of 2 or 6 stable spiral waves rotating at a frequency of 10Hz, depending on the boundary conditions. In the model of the human ventricles a single spiral wave formed a few seconds after application of the drug and it anchored to the basal ridge-like structure around the pulmonary valve, showing a true transition from ventricular fibrillation to ventricular tachycardia, as observed in experimental studies on verapamil [Samie et al. 2001]. The gained stability of the spiral waves could be the result of a flattening of the $APD$-restitution curve after blocking the calcium channel.

## 2 Future improvements of the model

A major caveat of the rPB model is the lack of the intracellular ionic concentration handling. It puts some constraints on the applicability of the model; the dynamics of calcium overload, sodium overload, etc., can no longer be studied. On the other hand, it should be noted that even the most recent models Jafri et al. [1998] of the calcium subsystem fail to represent fundamental properties of the calcium handling. Moreover, these models consist of as much as 40 variables, making them computationally very demanding. It would be good, in the expectation of better models and more powerful computers, to develop a low-dimensional model of the calcium subsystem which could reproduce the calcium transients in a phenomenological way and incorporate it into first generation ionic models.

A second objective would be to incorporate a bidomain description of the propagation of excitation in our human heart model. Bidomain models provide a more accurate description of the propagation of excitation in cardiac tissue by treating the intracellular and extracellular space domains separately. An important property of these model, is that they have a separate description of the extracellular field, and therefore can be applied for the modeling of several important problems in cardiology such as cardiac defibrillation: the application of a large external electrical field. Bidomain models can also describe cardiac tissue with nonequal anisotropy ratio, i.e. different extents of

anisotropy in the intracellular and extracellular spaces of myocardium. This leads to many surprising results, especially under the application of external electrical fields, such as *virtual electrodes*, initiation of reentry by unipolar stimulation, etc [Roth and Krassowska 1998]. The incorporation of the bidomain model could be performed by using an approach proposed by Keener and Bogar [1998].

The ventricles of the mammalian heart are activated by a specialised conduction system, called the His-Purkinje system. It is a complex network of fibers responsible for the conduction of the electrical impulse from the atria to the ventricular muscle. The incorporation of the conduction system is important for an accurate description of normal cardiac excitation, and can also influence the dynamics of spiral waves during arrhythmias [Berenfeld and Jalife 1998]. The conduction system starts at the atrioventricular node, where it is called the His bundle, which is divided in a right and left bundle branch. The distal conduction system of the ventricles mostly consists of specialised Purkinje cells which are cylindrical like myocardial cells, but have a larger diameter ($100\mu$m). As a result, the propagation of activation is up to three times faster in the Purkinje fibers than along myocardial fibers. The Purkinje fibers cover the left and right ventricular trabeculata in a network like fashion [Tawara 1906], but they are electrically separated from the myocardium except at some discrete points, called insertion sites [Overholt et al. 1984, Rawling and Joyner 1987]. It is through these points of junction that the Purkinje network can activate the myocardium (antegrade conduction) or the myocardium can reactivate the Purkinje fibers (retrograde conduction). There are two main approaches for the incorporation of a conduction system: it can be modeled as a three-dimensional object [Hren 1996, Berenfeld and Jalife 1998], or as a network of one-dimensional cables [Lieburg 1997]. We plan, in a near future, to incorporate a conduction system by using the approach of Lieburg [1997] and anatomical data obtained by Hren [1996].

One of the main factors which influences wave propagation in excitable media is anisotropy. In cardiac tissue, this anisotropy is structurally dependent, where the velocity of wave propagation along cardiac fibers can be 2 to 5 times faster than across them. Until recently numerous theoretical studies of the effects of anisotropy were based on the idea that electrical properties of the heart are isotropic in the plane orthogonal to the fiber direction (axial isotropy). This results in a conduction tensor with two distinct eigenvalues. However, it was recently found that cardiac tissue should be viewed as an electrically orthotropic structure [Hooks et al. 2002] in which fibers are assembled into distinct layers (myocardial sheets [LeGrice et al. 1994]). Such structure assumes that the conduction tensor has at any point three eigenvalues and three microstructurally defined directions. Studies of the effects of orthotropic anisotropy on defibrillation were started in [Hooks et al. 2002]. Studies of other basic effects of orthotropic anisotropy have not yet been performed. We intend to perform a systematic study of the effects of orthotropic anisotropy on the geometry of wave propagation and on dynamics of scroll waves in media with simple as well as with anatomically accurate geometries.

## 3 Future applications of the model

The anatomical model of the human ventricles can be used for several studies involving the electrical activation of the ventricles. Here, we will discuss two possible future

applications of the model: the first consists in the localisation of reentrant arrhythmias in the ventricles using electrocardiographic methods. The second, discuss a possible mechanism of ventricular fibrillation which could be investigated with the presented model.

Recently, a data base of QRS-integral maps was set up by SippensGroenewegen et al. [1990], in which the hearts of 12 patients were paced via catheters at 182 distinct endocardial sites. The pacing rate was 100 to 150 beats/min and the electrical potential was recorded by 62 electrodes on the torso. A QRS-integral map is obtained by integration of the electrical potential recorded in these electrodes over a time interval corresponding to the QRS complex on a standard 12-lead ECG, which corresponds to the activation of the ventricles. The main conclusion of SippensGroenewegen et al. [1990], is that the QRS-integral map depends only on the site of stimulation and do not vary much from patient to patient. On the basis of this conclusion, an atlas was generated which shows characteristic QRS-integral maps at 38 stimulation sites.
In 1997 a clinical study involved 4 patients with documented spontaneous ventricular fibrillation [Peters 1997]. Polymorphic ventricular tachycardia was induced in these patients during electrophysiological studies by a programmed stimulation protocol. The electrical potential of the heart was recorded in 62 leads on the torso. On the basis of these recordings, QRS-integral maps were constructed and compared to the data base of SippensGroenewegen et al. [1990]. It was found that the origin of the excitation source drifted in space, which seems to support the hypothesis by Gray et al. [1995a], that explains polymorphic ventricular tachycardia as a non-stationary spiral wave. The main problem here, is that it is impossible to perform a detailed recording of the spatial excitation pattern of the heart surface.
Hence, our model could be applied to study QRS-integral maps generated by spiral waves at different locations in the heart and compare it with experimental data of Peters [1997]. We would make use of a software package developed by Horáček [1974], Hren [1996], which would enable us to compute the electrical potential in the 62 leads on the torso and compute QRS-integral maps.

It is well known that several factors can facilitate the onset of ventricular fibrillation. One of them is discontinuous conduction. Structural discontinuities in cardiac tissue occur at several space scales: cell membranes are connected by discretely distributed gap junctions, the myocardial cells are organised into bundles and layers separated by connective tissue septae . Discontinuities also include the micro and macro vascular tree and other anatomical structures. Additional discontinuities occur as a result of myocardial infarction and involve increased fibrosis; which in some areas can have a density of up to 40% . The role of fibrosis in fibrillation is however not clear, because such isolating barriers may give rise to discontinuous conduction on one hand, which promotes fibrillation, but may also serve to anchor and stabilise reentry which prevents fibrillation. There are no doubts that the presence of both micro and macro discontinuities facilitates the onset of cardiac arrhythmias and fibrillation, but the exact mechanisms are still unknown.
Recently, some progress has been achieved in understanding how structural discontinuities can result in the formation of blocks and abnormal (reentrant) sources of excitation. However, the precise mechanism of the onset of ventricular fibrillation due to structural discontinuities remains unknown. It was shown theoretically and in experiment that the formation of unidirectional blocks (precursors of reentrant arrhythmias) occurred

on two types of macroscopic discontinuity: isthmus and geometrical expansion [Cabo et al. 1998]. Theoretical studies [Agladze et al. 1991] and experimental observations [Cabo et al. 1998] showed the formation of a reentrant source (spiral wave) at an inexcitable obstacle at high frequency pacing of cardiac tissue. However, this mechanism cannot explain the onset of self developing cardiac fibrillation, as it requires that the period of the external pacing should be faster than the period of the spiral wave which will be formed at this obstacle. This means that once created, the spiral wave will not be able to generate new ones, and hence degenerate into fibrillation. Recently this problem was elegantly studied in experiments performed by Bub et al. [2002], where break up of spiral waves was observed when decoupling gap junctions in cultures of cardiac cells. This was further illustrated by a similar behaviour in computations using a cellular automaton to reproduce cardiac electrical activity [Bub et al. 2002]. However, the precise mechanism of the onset of ventricular fibrillation due to discontinuities remain unknown.

We intend to study the influence of discontinuities on the dynamics of spiral waves in two-dimensional sheets of cardiac tissue and in the anatomical model of the human ventricles, by extending methods presented by Panfilov [2002].

# Appendix A

# Equations of the reduced PB model

All parameter values are listed in Table A.1.

– Equilibrium potentials:

$$E_{Na} = \frac{RT}{F} \ln \frac{\left[\mathrm{Na}^+\right]_e}{\left[\mathrm{Na}^+\right]_i} \tag{0.1}$$

$$E_{Ca} = \frac{2RT}{F} \ln \frac{\left[\mathrm{Ca}^{2+}\right]_e}{\left[\mathrm{Ca}^{2+}\right]_i} \tag{0.2}$$

$$E_K = \frac{RT}{F} \ln \frac{\left[\mathrm{K}^+\right]_e}{\left[\mathrm{K}^+\right]_i} \tag{0.3}$$

$$E_{to} = \frac{RT}{F} \ln \frac{0.043\left[\mathrm{Na}^+\right]_e + \left[\mathrm{K}^+\right]_e}{0.043\left[\mathrm{Na}^+\right]_i + \left[\mathrm{K}^+\right]_i} \tag{0.4}$$

where $R$ is the universal gas constant, $T$ the absolute temperature and $F$ the Faraday constant.

– Inward currents:

∗ Fast $\mathrm{Na}^+$ current

$$I_{Na} = g_{Na} \cdot m^3 \cdot v^2 \cdot (V_m - E_{Na}) \tag{0.5}$$

$$\alpha_m = \frac{0.32(V_m + 47.13)}{1 - \exp\left[-0.1(V_m + 47.13)\right]} \tag{0.6}$$

$$\beta_m = 0.08 \cdot \exp\frac{-V_m}{11} \tag{0.7}$$

$$v_\infty = 0.5\left[1 - \tanh\left(7.74 + 0.12V_m\right)\right] \tag{0.8}$$

$$\tau_v = 0.25 + 2.24\frac{1 - \tanh\left(7.74 + 0.12V_m\right)}{1 - \tanh\left[0.07(V_m + 92.4)\right]} \tag{0.9}$$

∗ Slow $\mathrm{Ca}^{2+}$ current

$$I_{Ca} = g_{Ca} \cdot d_\infty \cdot f \cdot f_{Ca} \cdot (V_m - E_{Ca}) \tag{0.10}$$

$$d_\infty = \frac{\alpha_d}{\alpha_d + \beta_d} \tag{0.11}$$

$$\alpha_d = \frac{14.98 \cdot \exp\left[-0.5(\frac{V_m - 22.36}{16.68})^2\right]}{16.68 \cdot \sqrt{2\pi}} \tag{0.12}$$

$$\beta_d = 0.1471 - \frac{5.3 \cdot \exp\left[-0.5(\frac{V_m - 6.27}{14.93})^2\right]}{14.93 \cdot \sqrt{2\pi}} \tag{0.13}$$

$$\alpha_f = \frac{0.00687}{1 + \exp\left(\frac{V_m - 6.1546}{6.12}\right)} \tag{0.14}$$

$$\beta_f = 0.000575 + \frac{0.069 \cdot \exp\left[-0.11(V_m + 9.825)\right] + 0.011}{1 + \exp\left[-0.278(V_m + 9.825)\right]} \tag{0.15}$$

$$f_{Ca} = \frac{1}{1 + \frac{\left[\mathrm{Ca}^{2+}\right]_i}{0.0006}} \tag{0.16}$$

– Outward currents:

∗ Transient outward current

$$I_{to} = g_{to} \cdot r_\infty \cdot to \cdot (V_m - E_{to}) \tag{0.17}$$

$$r_\infty = \frac{\alpha_r}{\alpha_r + \beta_r} \tag{0.18}$$

$$\alpha_r = \frac{0.5266 \cdot \exp\left[-0.0166(V_m - 42.2912)\right]}{1 + \exp\left[-0.0943(V_m - 42.2912)\right]} \tag{0.19}$$

$$\beta_r = \frac{5.186 \cdot 10^{-5} \cdot V_m + 0.5149 \cdot \exp\left[-0.1344(V_m - 5.0027)\right]}{1 + \exp\left[-0.1348(V_m - 5.186 \cdot 10^{-5})\right]} \tag{0.20}$$

$$\alpha_{to} = \frac{5.612 \cdot 10^{-5} \cdot V_m + 0.0721 \cdot \exp\left[-0.173(V_m + 34.2531)\right]}{1 + \exp\left[-0.1732(V_m + 34.2531)\right]} \tag{0.21}$$

$$\beta_{to} = \frac{1.215 \cdot 10^{-4} \cdot V_m + 0.0767 \cdot \exp\left[-0.166 \cdot 10^{-9} \cdot (V_m + 34.0253)\right]}{1 + \exp\left[-0.1604(V_m + 34.0253)\right]} \tag{0.22}$$

$$\tau_{to}(V_m) = \frac{1}{p\alpha_{to}(V_m) + p\beta_{to}(V_m)} \tag{0.23}$$

$$to_\infty(V_m) = \frac{\alpha_{to}(V_m - V_{shift})}{\alpha_{to}(V_m - V_{shift}) + \beta_{to}(V_m - V_{shift})} \tag{0.24}$$

∗ Delayed rectifier $K^+$ current

$$I_K = g_K \cdot X^2 \cdot (V_m - E_K) \tag{0.25}$$

For endo- and epicardial cells

$$X_\infty = \frac{0.988}{1 + \exp\left(-0.861 - 0.062 \cdot V_m\right)} \tag{0.26}$$

$$\tau_X = 240 \cdot \exp\left[-\frac{(V_m + 25.5)^2}{156}\right] + 182 \cdot \left[1 + \tanh\left(0.154 + 0.0116 \cdot V_m\right)\right] + \tau'_X \tag{0.27}$$

$$\tau'_X = 40\left[1 - \tanh\left(160 + 2 \cdot V_m\right)\right] \tag{0.28}$$

For M cells

$$X_\infty = \frac{0.972}{1 + \exp\left(-2.036 - 0.0834 \cdot V_m\right)} \tag{0.29}$$

$$\tau_X = 380 \cdot \exp\left[-\frac{(V_m + 25.5)^2}{156}\right] + 166 \cdot \left[1 + \tanh\left(0.558 + 0.0169 \cdot V_m\right)\right] \tag{0.30}$$

* Inward rectifier $K^+$ current

$$I_{K1} = g_{K1} \cdot K1_\infty \cdot (V_m - E_K) \tag{0.31}$$

$$K1_\infty = \frac{\alpha_{K1}}{\alpha_{K1} + \beta_{K1}} \tag{0.32}$$

$$\alpha_{K1} = \frac{0.1}{1 + \exp\left[0.06(V_m - E_K - 200)\right]} \tag{0.33}$$

$$\beta_{K1} = \frac{3 \cdot \exp\left[2 \cdot 10^{-4} \cdot (V_m - E_K + 100)\right] + \exp\left[0.1(V_m - E_K - 10)\right]}{1 + \exp\left[-0.5(V_m - E_K)\right]} \tag{0.34}$$

– Background currents:

* $Ca^{2+}$ background current

$$I_{Ca,b} = g_{Ca,b} \cdot (V_m - E_{Ca}) \tag{0.35}$$

* $Na^+$ background current

$$I_{Na,b} = g_{Na,b} \cdot (V_m - E_{Na}) \tag{0.36}$$

– Pump and exchanger currents:

* $Na^+$-$K^+$ pump

$$I_{NaK} = g_{NaK} \cdot f_{NaK} \cdot f'_{NaK} \tag{0.37}$$

$$f_{NaK} = \frac{1}{1 + 0.1245 \cdot \exp\left(-0.0037 \cdot V_m\right) + 0.0365 \cdot \sigma \cdot \exp\left(-0.037 \cdot V_m\right)} \tag{0.38}$$

$$f'_{NaK} = \frac{1}{1 + \left(\frac{10}{\left[\mathrm{Na}^+\right]_i}\right)^{1.5}} \cdot \frac{\left[\mathrm{K}^+\right]_e}{\left[\mathrm{K}^+\right]_e + 1.5} \tag{0.39}$$

$$\sigma = 0.1428 \cdot \left[\exp\left(\frac{\left[\mathrm{Na}^+\right]_e}{67.3}\right) - 1\right] \tag{0.40}$$

* $Na^+/Ca^{2+}$ exchanger

$$I_{NaCa} = g_{NaCa} \cdot f_{NaCa} \tag{0.41}$$

$$f_{NaCa} = \frac{1}{87.5^3 + \left[\mathrm{Na}^+\right]_e^3} \cdot \frac{1}{1.38 + \left[\mathrm{Ca}^{2+}\right]_e} \cdot \frac{1}{0.1 \cdot \exp\left(-0.024 \cdot V_m\right)} \cdot \left\{\left[\mathrm{Na}^+\right]_i^3 \cdot \left[\mathrm{Ca}^{2+}\right]_e \cdot \exp\left(0.013 \cdot V_m\right) - \left[\mathrm{Na}^+\right]_e^3 \cdot \left[\mathrm{Ca}^{2+}\right]_i \cdot \exp\left(-0.024 \cdot V_m\right)\right\} \tag{0.42}$$

| | |
|---|---|
| T (°C) | 37 |
| $g_{Na}$ (nS/pF) | 16 |
| $g_{Ca}$ (nS/pF) | 0.064 |
| $g_K$ (nS/pF) | 0.019 |
| $g_{to}$ (nS/pF) | 0.4 |
| $g_{Na,b}$ (nS/pF) | 0.001 |
| $g_{Ca,b}$ (nS/pF) | 0.00085 |
| $g_{K1}$ (nS/pF) | 3.9 |
| $g_{NaK}$ (nS/pF) | 1.3 |
| $g_{NaCa}$ (nS/pF) | 1000 |
| $[\mathrm{Ca}^{2+}]_i$ (mM) | 0.0004 |
| $[\mathrm{Ca}^{2+}]_e$ (mM) | 2 |
| $[\mathrm{Na}^{+}]_i$ (mM) | 10 |
| $[\mathrm{Na}^{+}]_e$ (mM) | 138 |
| $[\mathrm{K}^{+}]_i$ (mM) | 140 |
| $[\mathrm{K}^{+}]_e$ (mM) | 4 |

Table A.1: Parameter values of the reduced PB model

# Appendix B

# Numerical methods

## 1 The technique of Rush and Larsen [1978] for the integration of the gating equations

Models based on the Hodgkin-Huxley formulation of the gating variables, involve equations of the following type:

$$\frac{dy}{dt} = \alpha_y(V_m)\,(1-y) - \beta_y(V_m)\,y \tag{1.1}$$

for a gating variable $y$ and its gating functions $\alpha_y$ and $\beta_y$ (see Chapter I). This equation can be rewritten in a more useful way, as a relaxation equation:

$$\frac{dy}{dt} = \frac{y_\infty(V_m) - y}{\tau_y(V_m)} \tag{1.2}$$

with $y_\infty(V_m) = \frac{\alpha_y(V_m)}{\alpha_y(V_m)+\beta_y(V_m)}$ and $\tau_y(V_m) = \frac{1}{\alpha_y(V_m)+\beta_y(V_m)}$. Thus, if the functions $\alpha_y$ and $\beta_y$ remain constant over a time increment $\Delta t$, we can solve equation (1.2) and find:

$$y(t) = y_\infty(V_m) - (y_\infty(V_m) - y(0))\,e^{-\frac{\Delta t}{\tau_y(V_m)}} \tag{1.3}$$

Now, if equation (1.3) is assumed sufficiently accurate over one time increment, which will be the case if $\Delta t$ is sufficiently small, we can setup the following numerical scheme for solving the dynamical gating equations of a Hodgkin-Huxley like model:

$$y_{n+1} = y_\infty(v_n) - (y_\infty(v_n) - y_n)\,e^{-\frac{\Delta t}{\tau_y(v_n)}} \tag{1.4}$$

where $y_n$ and $v_n$ denote the values of $V_m$ and $y$ at the $n$th time step. The advantage of this approach is that the functions $y_\infty$ and $e^{-\frac{\Delta t}{\tau_y}}$ can be tabulated beforehand and scheme 1.4 performed in a very efficient and rapid way.

## 2 Numerical approach for the discretisation of the diffusion term in the ventricular geometry

The membrane equation in the anatomical model is given by:

$$C_m \frac{\partial V_m}{\partial t} = -I_{ion} + \nabla d \nabla V_m \tag{2.5}$$

with $d$ the diffusion matrix accounting for the local fiber orientation. For the integration of the PDE we need to evaluate at each point the term :

$$\nabla d \nabla V_m = \frac{\partial}{\partial x} I_x + \frac{\partial}{\partial y} I_y + \frac{\partial}{\partial z} I_z \tag{2.6}$$

where $\vec{I} = (I_x, I_y, I_z)$ is the "axial" current (i.e. the lumped current in the intracellular and extracellular space):

$$I_i = d_{ii}\frac{\partial V_m}{\partial x} + d_{ij}\frac{\partial V_m}{\partial y} + d_{ik}\frac{\partial V_m}{\partial z} \tag{2.7}$$

We also need to evaluate this term at the boundary, where we impose the no-flux (no-"axial" current) conditions.

If $h$ is the (small) spatial scale of our anatomical model, we can approximate the first term of (2.6) by (and similar formula's for the other terms) a centred difference :

$$\frac{\partial I_x}{\partial x}(X,Y,Z) = \frac{I_x(X+0.5h,Y,Z) - I_x(X-0.5h,Y,Z)}{h} \tag{2.8}$$

In order to find $I_x(X \pm 0.5h, Y, Z)$ in (2.8) from (2.7), we need to calculate spatial derivatives of $V_m$ and the diffusion matrix $d$ in the points $(X \pm 0.5h, Y, Z)$. Note that the fields $V_m$ and $d$ are only calculated in the grid points. In what follows we shall consider the point $(X + 0.5h, Y, Z)$ and calculate $I_x$ in that point using (2.7):

- *Term* $\frac{\partial V_m}{\partial x}(X + 0.5h, Y, Z)$*:* We readily find:

  $$\frac{\partial V_m}{\partial x}(X+0.5h,Y,Z) = \frac{V_m(X+h,Y,Z) - V_m(X,Y,Z)}{h} \tag{2.9}$$

  If $(X + h, Y, Z)$ lies outside the heart, we impose the no-flux boundary conditions by putting $\frac{\partial V_m}{\partial x}(X + 0.5h, Y, Z) = 0$.
- *Term* $\frac{\partial V_m}{\partial y}(X + 0.5h, Y, Z)$*:* Since the space scale is assumed to be small, we can find by linear interpolation that:

  $$\frac{\partial V_m}{\partial y}(X+0.5h,Y,Z) = \frac{1}{2}\left(\frac{\partial V_m}{\partial y}(X+h,Y,Z) - \frac{\partial V_m}{\partial y}(X,Y,Z)\right) \tag{2.10}$$

  Moreover, we have

  $$\frac{\partial V_m}{\partial y}(X+h,Y,Z) = \frac{V_m(X+h,Y+h,Z) - V_m(X+h,Y-h,Z)}{2h} \tag{2.11}$$

  $$\frac{\partial V_m}{\partial y}(X,Y,Z) = \frac{V_m(X,Y+h,Z) - V_m(X,Y-h,Z)}{2h} \tag{2.12}$$

  Again, if $(X + h, Y + h, Z)$ or $(X + h, Y - h, Z)$ lies outside the heart $\frac{\partial V_m}{\partial y}(X + h, Y, Z) = 0$. If $(X, Y + h, Z)$ or $(X, Y - h, Z)$ lies outside the heart $\frac{\partial V_m}{\partial y}(X, Y, Z) = 0$. Hence

  $$\begin{aligned}\frac{\partial V_m}{\partial y}(X+0.5h,Y,Z) = \frac{1}{4h}(&V_m(X+h,Y+h,Z) - V_m(X+h,Y-h,Z)\\ &+ V_m(X,Y+h,Z) - V_m(X,Y-h,Z))\end{aligned} \tag{2.13}$$

  keeping the boundary conditions in mind.

– *Term* $\frac{\partial V_m}{\partial z}(X+0.5h,Y,Z)$*:* Analogous to previous calculations, we find:

$$\begin{aligned}\frac{\partial V_m}{\partial z}(X+0.5h,Y,Z) =& \frac{1}{4h}(V_m(X+h,Y,Z+h) - V_m(X+h,Y,Z-h) \\ &+ V_m(X,Y,Z+h) - V_m(X,Y,Z-h))\end{aligned} \tag{2.14}$$

– *diffusion matrix:* Linear interpolation yields :

$$d_{1j}(X+0.5h,Y,Z) = \frac{1}{2}(d_{1j}(X+h,Y,Z) + d_{1j}(X,Y,Z)) \quad j=1,2,3 \tag{2.15}$$

Substitution of (2.15), (2.14), (2.13) and (2.9) in (2.8) and similar calculation in the point $(X-0.5h,Y,Z)$ yields the first term of (2.6). Analogously we obtain the two other terms of (2.6), which yields a discretisation given by :

$$L(i,j,k) = \nabla d \nabla V_m(i,j,k) = \sum_{l=0}^{18} w_l \; V_m(l) \tag{2.16}$$

where $l$ is an index running over the neighbours $(X \pm h, Y \pm h, Z \pm h)$ of the point $(X,Y,Z)$, the point itself included and $w_l$ are the computed weights of each neighbour. These weights can easily be found by putting $V_m$ to 0 in all heart points, except the desired neighbour and applying above method.

Note that in our representation, the boundary conditions are handled automatically, i.e. if a neighbour $l$ of a point is situated outside the heart, it will get a weight $w_l$ zero and will not affect the wave propagation. Computed weight for each heart point are stored in an array and evaluation of term (2.16) is performed in a very efficient way, just as a matrix product.

## Bibliography


K.I. Agladze, J.P. Keener, S.C. Müller and A.V. Panfilov, Rotating spiral waves created by geometry, *Science* **264**, 1746–1748 (1991).

K.I. Agladze and V.I. Krinsky, Multiarmed vortices in an active chemical medium, *Nature* **292**, 424–426 (1982).

R.R. Aliev and A.V. Panfilov, A simple two-variable model of cardiac excitation, *Chaos, Solitons and Fractals* **7**, 293–301 (1996).

M.A. Allessie, F.I.M. Bonke and F.J.G. Schopman, Circus movement in rabbit atrial muscle as a mechanism of tachycardia, *Circ. Res.* **33**, 54–62 (1973).

C. Antzelevitch, V.V. Nesterenko, A.L. Muzikant, J.J. Rice, G. Chen and T. Colatsky, Influence of transmural repolarisation gradients on the electrophysiology and pharmacology of ventricular myocardium. cellular basis for the brugada and the long QT-syndromes, *Phil. Trans. R. Soc. London* **359**, 1201–1216 (2001).

H. Arce, A. Xu, H. González and M.R. Guevara, Alternans and higher-order rhythms in an ionic model of a sheet of ischemic ventricular muscle, *Chaos* **10**, 411–426 (2000).

J.A. Armour and W.C. Randall, Structural basis for cardiac function, *Am. J. Physiol* **218**, 1517–1523 (1970).

S.M. Ashamalla, D. Navarro and C.A. Ward, Gradient of sodium current across the left ventricular wall of adult rat hearts, *J. Physiol. (Lond.)* **536**, 439–443 (2001).

R.C. Barr, T.C. Pilkington, J.P. Boineau and M.S. Spach, Determining surface potentials from current dipoles, with application to electrocardiography, *IEEE Trans. Biomed. Eng.* **13**, 88–92 (1966).

B.G. Bass, Restitution of the action potential in cat papillary muscle, *Am. J. Physiol.* **228**, 1717–1724 (1975).

G.W. Beeler and H.J. Reuter, Reconstruction of the action potential of ventricular myocardial fibers, *J. Physiol.* **268**, 177–210 (1977).

O. Berenfeld and J. Jalife, Purkinje-muscle reentry as a mechanism of polymorphic ventricular arrhythmias in a 3-dimensional model of the ventricles, *Circ.Res.* **82**, 1063–1077 (1998).

O. Bernus, B. Van Eyck, H. Verschelde and A.V. Panfilov, Transition from ventricular fibrillation to ventricular tachycardia: a simulationi study on the role of $Ca^{2+}$-blockers in human ventricular tissue, *Phys. Med. Biol.* **47**, 4167–4179 (2002a).

O. Bernus, H. Verschelde and A.V. Panfilov, Modified ionic models of cardiac tissue for efficient large scale computations, *Phys. Med. Biol.* **47**, 1947–1959 (2002b).

O. Bernus, H. Verschelde and A.V. Panfilov, Reentry in an anatomical model of the human ventricles, *Int. J. Bif. Chaos (accepted)* (2003a).

O. Bernus, H. Verschelde and A.V. Panfilov, Spiral wave stability in cardiac tissue with biphasic restitution, *Phys. Rev. E (submitted)* (2003b).

O. Bernus, R. Wilders, C.W. Zemlin, H. Verschelde and A.V. Panfilov, A computationally efficient electrophysiological model of human ventricular cells, *Am. J. Physiol. Heart Circ. Physiol.* **282**, H2296–H2308 (2002c).

D.J. Beuckelmann, M. Nabauer and E. Erdmann, Intracellular calcium handling in isolated ventricular myocytes from patients with terminal heart failure, *Circulation* **85**, 1046–1055 (1992).

D.J. Beuckelmann, M. Nabauer and E. Erdmann, Alterations of $K^+$ currents in isolated human ventricular myocytes from patients with terminal heart failure, *Circ Res* **73**, 379–385 (1993).

G. Bub, A. Shrier and L. Glass, Spiral wave generation in heterogeneous media, *Phys. Rev. Lett.* **88**(5), 058101 (2002).

C. Cabo, A.M. Pertsov, J.M. Davidenko, W.T. Baxter, R.A. Gray and J. Jalife, *Chaos* **8**, 116–126 (1998).

D.M. Cassidy, J.A. Vassalo, F.E. Marchlinsky, A.E. Buxton, W.J. Untereker and M.E. Josephson, Endocardial mapping in humans in sinus rhythm with normal left ventricles: activation patterns and characteristics of electrograms, *Circulation* **70**, 37–42 (1984).

E.M. Cherry, H.S. Greenside and C.S. Henriquez, A space-time adaptive method for simulatin complex cardiac dynamics, *Phys. Rev. Lett.* **84**, 1343–1346 (2000).

F.J. Chorro, J. Canoves, J. Guerrero, L. Mainar, J. Sanchis, L. Such and V. Lopez-Merino, Alteration of ventricular fibrillation by flecainide, verapamil, and solatol. an experimental study, *Circulation* **101**(1606-1615) (2000a).

F.J. Chorro, J. Canoves, J. Guerrero, L. Mainar, J. Sanchis, L.M. Such, A. Rosado and V. Lopez-Merino, Opposite effects of myocardial stretch and verapamil on the complexity of the ventricular fibrillatory pattern: and experimental study, *Pacing Clin. Electrophysiol.* **23**, 1594–1603 (2000b).

R.H. Clayton and A.V. Holden, A method to quantify the dynamics and complexity of re-entry in computational models of ventricular fibrillation, *Phys. Med. Biol.* **47**, 225–238 (2002).

R.H. Clayton, A. Murray and R.W. Campbell, Objective features of the surface electrocardiogram during ventricular tachyarrhythmias, *Eur. Heart J.* **16**, 1115–1119 (1995).

M. Courtemanche, L. Glass and J. P. Keener, Instabilities of a propagating pulse in a ring of excitable media, *Phys. Rev. Lett.* **70**, 2182–2185 (1993).

M. Courtemanche, J.P. Keener and L. Glass, A delay equation representation of pulse circulation on a ring of excitable media, *SIAM J. Appl. Math.* **56**, 119–142 (1996).

M. Courtemanche, R.J. Ramirez and S. Nattel, Ionic mechanisms underlying human atrial action potential properties: insights from a mathematical model, *Am.J.Physiol.* **275**, H301–H321 (1998).

R.Th. van Dam, Ventricular activation in human and canine bundle branch block, In H.J.J. Wellens, K.I. Lie and M.J. Janse, editors, *The Conduction System of the Heart: Structure, Function and Clinical Implications* pages 377–392. Lea & Febiger Philadelphia (1976).

J.M. Davidenko, Spiral wave activity as common mechanism for polymorphic and monomorphic ventricular tachycardias, *J. Cardiovasc. Electrophysiol.* **4**, 730–746 (1993).

J.M. Davidenko, A.M. Pertsov, R. Salomontsz, W. Baxter and J. Jalife, Stationary and drifting spiral waves of excitation in isolated cardiac muscle, *Nature* **355**, 349–351 (1991).

D. Durrer, R.T. Van Dam, G.E. Freud, M.J. Janse, F.L. Meijler and R.C. Arzbaecher, Total excitation of the isolated human heart, *Circulation* **41**, 899–912 (1970).

I.R. Efimov, V. I. Krinsky and J. Jalife, Dynamics of rotating vorticees in the Beeler-Reuter model of cardiac tissue, *CHaos, Solitins abd Fractals* **5**, 513–526 (1995).

I.R. Efimov, V.Y. Sidorov, Y. Cheng and B. Wollenzier, Evidence of 3d scroll waves with ribbon-shaped filament as a mechanism of ventricular tachycardia in the isolated rabbit heart, *J. Cardiovasc. Electrophysiol.* **10**, 1452–1462 (1999).

W.J. Eifler, E. Macchi, H.J.R. Van Eck, B.M. Horacek and P.M. Rautaharju, Mechanism of generation of body surface electrocardiographic p-waves in normal, middle, and lower sinus rhythms, *Circ. Res.* **48**, 168–182 (1981).

W. Einthoven, Weiteres uber das elektrokardiogram, *Pfluger Arch. ges. Physiol.* **122** (517-548) (1908).

L.P. Endresen and N. Skarland, Limit cycle oscillations in pacemaker cells, *IEEE Trans Biomed Eng* **47**, 1134–1137 (2000).

V.G. Fast, I.R. Efimov and V.I. Krinsky, Transition from circular to linear cores in excitable media, *Phys.Lett.A* **151**, 157–161 (1990).

F. Fenton, E.M. Cherry, H.M. Hastings and S.J. Evans, Multiple mechanisms of spiral wave breakup in a model of electrical cardiac activity, *Chaos* **12**, 852–892 (2002).

F. Fenton and A. Karma, Vortex dynamics in three-dimensional continuous myocardium with fiber rotation: filament instability and fibrillation, *Chaos* **8**, 20–47 (1998).

R. FitzHugh, Impulses and physiological states in theoretical models of nerve membrane, *Biophys. J.* **1**, 445–465 (1961).

M.R. Franz, J. Schaefer, M. Schóttler, W.A. Seed and M.I.M. Noble, Electrical and mechanical restitution of the human heart at different rates of stimulation, *Circ. Res.* **53**, 815–822 (1983).

D.W. Frazier, P.D. Wolf, J.M. Wharton, A.S.L. Tang, W.M. Smith and R.E. Ideker, Stimulus-induced critical points: Mechanism for electrical induction of reentry in normal canine myocardium, *J. Clin. Invest.* **83**, 1039–1052 (1989).

D. Gabor and C.V. Nelson, The determination of the resultant dipole of the heart from measurements on the body-surface., *J. Apll. Phys.* **25**, 413–416 (1954).

A. Garfinkel, Y.H. Kim, O. Voroshilovsky, Z. Qu, J.R. Kil, M.H. Lee, H.S. Karagueuzian, J.N. Weiss and P.S. Chen, Preventing ventricular fibrillation by flattening cardiac restitution, *Proc. Natl. Acad. Sci. USA* **97**, 6061–6066 (2000).

L.S. Gettes, W. E. Cascio and W. E. Sanders, Mechanisms of sudden cardiac death, In D.P. Zipes and J. Jalife, editors, *Cardiac electrophysiology. From cell to bedside, 2nd edition* pages 527–538 Philadelphia (1995). Saunders.

L. Glass, Dynamics of cardiac arrhythmias, *Physics Today* **49**, 40–45 (1996).

E. Goldberger, The avl, avr and avf leads; a simplification of standard lead electrocardiography, *Am. Heart J.* **24**(378-396) (1942a).

E. Goldberger, A simple indifferent electrocardiographic electrode of zero potential and a technique of obtaining augmented, unipolar extremity leads, *Am. Heart J.* **23** (483-492) (1942b).

N.A. Gorelova and J.J. Bures, *J. Neurobiol.* **14**, 353–363 (1983).

R.A. Gray, J. Jalife, A. Panfilov, W.T. Baxter, C. Cabo, J.M. Davidenko and A.M. Pertsov, Mechanisms of cardiac fibrillation, *Science* **270**, 1222–1223 (1995a).

R.A. Gray, J. Jalife, A. Panfilov, W.T. Baxter, C. Cabo and A.M. Pertsov, Nonstationary vortex-like reentrant activity as a mechanism of polymorphic ventricular tachycardia in the isolated rabbit heart, *Circulation* **91**, 2454–2469 (1995b).

R.A. Gray, A.M. Pertsov and J. Jalife, Spatial and temporal organization during cardiac fibrillation, *Nature* **392**, 75–78 (1998).

R.A. Greenbaum, S. Yen Ho, D.G. Gibson, A.E. Becker and R.H. Anderson, Left ventricular fibre architecture in man, *Br. Heart J* **45**, 248–263 (1981).

M.R. Guevara, A. Ward, A. Shrier and L. Glass, Electrical alternans and period doubling bifurcations, *IEEE Comp. Cardiol.* **562**, 167–170 (1984).

R.M. Gulrajani, *Bioelectricity and Biomagnetism*, John Wiley and Sons New-York (1998).

F.O. Hadlock, A shortest path algorithm for grid graphs, *Networks* **7**, 323–334 (1977).

A.L. Hodgkin and A.F. Huxley, A quantitative description of membrane current and its application to conduction and excitation in nerve, *J. Physiol.* **117**, 500–544 (1952).

D.A. Hooks, K.A. Tomlinson, S.G. Marsden, I.J. LeGrice, B.H. Smail, A.J. Pullan and P.J. Hunter, Cardiac microstructure: implication for propagation and defibrillation in the heart, *Circ. Res.* **91**, 331–338 (2002).

B.M. Horáček, Numerical model of an inhomogeneous human torso, *Adv Cardiol* **10**, 51–57 (1974).

W. Hort, Untersuchungen uber die Muskelfaserdehnung und das Gefuge des Myokards in der rechten Herzkammerwand des Meerschweinchens, *Virchows. arch.* **329**, 694–731 (1957).

R.G. Hoyt, J.L. Cohen and J.E. Saffitz, Distribution and three-dimensional structure of intercellular junctions in canine myocardium, *Circ. Res.* **64**, 563–574 (1989).

R. Hren, *A realistic model of the human ventricular myocardium: Application to the study of extopic activation*, PhD thesis, Dalhouse University, Halifax (1996).

H. Iunuma and K. Kato, Mechanisms of augmented premature responses in canine ventricular muscle, *Circ. Res.* **44**, 624–629 (1979).

M.S. Jafri, J.J. Rice and R.L. Winslow, Cardiac $Ca^{2+}$ dynamics: the roles of rayodine receptor adaptation and sarcoplasmic reticulum load, *Biophys. J.* **74**, 1149–1168 (1998).

W. Jahnke, Ch. Henze and A.T. Winfree, Chemical vortex dynamics in three-dimensional excitable media, *Nature* **336**, 662–665 (1988).

J. Jalife, Ventricular fibrillation: mechanisms of initiation and maintenance, *Annu Rev Physiol.* **62**, 25–50 (2000).

J. Jalife, O. Berenfeld, A. Skanes and R. Mandapati, Mechanisms of atrial fibrillation: mother rotors or multiple daughter wavelets, or both?, *J Cardiovasc Electrophysiol* **9**, S1–S12 (1998a).

J. Jalife, R.A. Gray, G.E. Moeley and J.M. Davidenko, Self-organization and the dynamical nature of ventricular fibrillation, *Chaos* **8**, 79–93 (1998b).

M.J. Janse, Vulnerability to ventricular fibrillation, *Chaos* **8**, 149–156 (1998).

H.J. Jongsma and R. Wilders, Gap junctions in cardiovascular disease, *Circ.Res.* **86**, 1193–1197 (2000).

A. Karma, Electrical alternans and spiral wave breakup in cardiac tissue, *Chaos* **4**, 461–472 (1994).

J.P. Keener and K. Bogar, A numerical method for the solution of the bidomain equations in cardiac tissue, *Chaos* **8**, 234–241 (1998).

M.L. Koller, M.L. Riccio and R.F. Gilmour Jr, Dynamics restitution of action potential duration during electrical alternans and ventricular fibrillation, *Am.J.Physiol* **275**, H1635–H1642 (1998).

S. Koumi, C.L. Bakker and C.E. Arentzen, Characterization of inwardly rectifying $K^+$ channel in human myocytes. alterations in channel behavior in myocytes isolated from patients with idiopathic dilated cardiomyopathy, *Circulation* **92**, 164–174 (1995).

V.I. Krinsky, Spread of excitation in an inhomogeneous medium (state similar to cardiac fibrillation), *Biophysics* **11**, 776–784 (1966).

J. Lechleiter, S. Girard, E. Peraltal and D. Clapham, *Science* **252**, 123–126 (1991).

M.H. Lee, Z. Qu, G.A. Fishbein, S.T. Lamp, E.H. Chang, T. Ohara, O. Voroshilovsky, J.R. Kil, A.R. Hamzei, N.C. Wang, S.F. Lin, J.N. Weiss, A. Garfinkel, H.S. Karagueuzian and P.S. Chen, Patterns of wave break during ventricular fibrillation in isolated swine right ventricle, *Am. J. Physiol. Heart. Circ. Physiol.* **281**(H253-265) (2002).

I.J. LeGrice, P.J. Hunter and B.H. Smail, Laminar structure of the heart. II. Mathematical model, *Am. J. Physiol.* (1994), submitted.

G.R. Li, J. Feng, L. Yue and M. Carrier, Transmural heterogeneity of action potentials and $I_{to1}$ in myocytes isolated from the human right ventricle, *Am. J. Physiol. Heart. Circ. Physiol.* **275**, H369–H377 (1998).

T. Lieburg, *Modeling the ventricular conduction system. Report.*, Pharmacology, SUNY,USA (1997).

D.W. Liu, G.A. Gintant and C. Antzelevitch, Ionic bases for electrophysiological distinctions amogn epicardial, midmyocardial, and endocardial myocytes from the free wall of the canine left ventricle, *Circ. Res.* **72**, 671–687 (1993).

R. Lower, *Tractatus de Corde*, J Allestry London (1669).

K.F.W. Ludwig, Uber den Bau und Bewegung der Herzventrekel., *Z. Rationelle Med.* **7**, 189–220 (1849).

C.H. Luo and Y. Rudy, A model of the ventricular cardiac action potential. Depolarization, repolarization, and their interaction, *Circ. Res.* **68**, 1501–1526 (1991).

C.H. Luo and Y. Rudy, A dynamic model of the cardiac ventricular action potential. i. simulations of ionic currents and concentration changes., *Circ. Res.* **74**, 1071–1096 (1994).

T.M. MacRobert, *Spherical harmonics: an elementary treatise on harmonic functions with applications*, Pergamon Press Oxford (1967).

M.C. Main, S.M. Bryant and G. Hart, Regional differences in action potential characteristics and membrane currents of guinea-pig left ventricular myocytes, *Exp. Physiol.* **83**, 747–761 (1998).

J. Malmivuo and R. Plonsey, *Bioelectromagnetism*, Oxford University Press Oxford (1995).

D.W. Marquardt, An algorithm for least-squares estimation of nonlinear parameters., *J. SIAM* **11**, 431–441 (1963).

G.K. Moe, W.C. Rheinbolt and J.A. Abildskov, A computer model of atrial fibrillation, *Am. Heart J.* **67**, 200–220 (1964).

J.M. Morgan, D. Cunninggham and E. Rowland, Dispersion of monophasic action potential duration: demonstrable in humans after premature ventricular extrastimulation but not in steady state, *J. Am. Coll. Cardiol.* **19**, 1244–1253 (1992a).

J.M. Morgan, D. Cunninggham and E. Rowland, Electrical restitution in the endocardium of the intact human right ventricule, *Br. Heart J.* **67**, 42–46 (1992b).

R.J. Myerburg, K.M. Kessler, Interian Jr A., P. Fernandez, S. Kimura, P.L. Kozlovskis, T. Furukawa, A. L. Bassett and A. Castellanos, In D. P. Zipes and J. Jalife, editors, *Cardiac electrophysiology. From cell to bedside* page 666 Philadelphia (1990). Saunders.

J.S. Nagumo, S. Arimoto and S. Yoshizawa, An active pulse transmission line simulating nerve axon, *Proc. IRE.* **50**, 2061–2071 (1962).

P.P. Nánási, A. Varró, C. Pankucsi, P. Homolay, T.K. Knilans, L. Kovács, G.J. Papp and D.A. Lathrop, Electrical restitution in diseased human ventricular myocardium, *Clinical Physiology* **16**, 339–351 (1996).

P.M.F. Nielson, I.J. LeGrice, B.H. Smail and P.J. Hunter, A mathematical model of the geometry and fibrous structure of the heart, *Am. J. Physiol.* **260**, H1365–H1378 (1991).

D. Noble, A modification of the Hodgkin−Huxley equation applicable to purkinje fiber action and pacemaker potential, *J. Physiol.* **160**, 317–352 (1962).

D. Noble, A. Varghese, P. Kohl and P. Noble, Improved guinea pig ventricular cell model incorporating a diadic space, $I_{Kr}$ and $I_{Ks}$, and length- and tension-dependent processes, *Can. J. Cardiol.* **14**, 123–134 (1998).

A. Nygren, C. Fiset, L. Firek, J.W. Clark, D.S. Lindblad, R.B. Clark and W.R. Giles, Mathematical model of an adult human atrial cell. the role of $k^+$ currents in depolarization., *Circ. Res.* **82**(63-81) (1998).

Y.S. Orlov, M.A. Brodsky, M.V. Orlov and B. Allen, Near doubling of heart rate after intravenous verapamil for treatment of atrial fibrillation without preexcitation, *Pacing Clin. electrophysiol.* **20**, 2867–2869 (1997).

E.D. Overholt, R.W. Joyner, R.D. Veenstra, D.A. Rawling and R. Weidmann, Unidirectional block between Purkinje and ventricular layers of papillary muscles, *Am J Physiol* **247**, H584–H595 (1984).

A.V. Panfilov, Modelling of reentrant patterns in an anatomical model of the heart, In A.V. Panfilov and A.V. Holden, editors, *Computational Biology of the Heart* pages 259–276 Chichester (1997). Wiley.

A.V. Panfilov, Spiral breakup as a model of ventricular fibrillation, *Chaos* **8**, 57–64 (1998).

A.V. Panfilov, Three-dimensional organization of electrical turbulence in the heart, *Phys. Rev. E* **59**, R6251–R6254 (1999).

A.V. Panfilov, Spiral breakup in an array of coupled cell: the role of the intercellular conductance, *Phys. Rev. Lett.* **88**, 118101 (2002).

A.V. Panfilov and A.V. Holden, Spatio−temporal irregularity in a two-dimensional model of cardiac tissue, *Int. J. Bif. and Chaos* **1**, 119–129 (1991).

A.V. Panfilov and J.P. Keener, Re-entry in an anatomical model of the heart, *Chaos, Solitons and Fractals* **5**, 681–689 (1995a).

A.V. Panfilov and J.P. Keener, Re-entry in three−dimensional myocardium with rotational anisotropy, *Physica D* **84**, 545–552 (1995b).

A.V. Panfilov and A.F.M. Marée, Spiral breakup in excitable tissue due to lateral instability, *Phys. Rev. Lett.* **78**, 1819–1822 (1997).

A.V. Panfilov and A.M. Pertsov, Ventricular fibrillation: evolution of the multiple wavelet hypothesis, *Phil. Trans. R. Soc. Lond. A* **359**, 1315–1325 (2001).

A.M. Pertsov, J.M. Davidenko, R. Salomontsz, W. Baxter and J. Jalife, Spiral waves of excitation underlie reentrant activity in isolated cardiac muscle, *Circ. Res.* **72**, 631–650 (1993).

H. Peters, *Clinical value of body surface mapping for locatization and anaysis of arrhythmogenic substrates*, PhD thesis, Utrecht University, Utrecht (1997).

R. Plonsey and R.C. Barr, *Bioelectricity: a quantitative approach*, Plenum New York (1988).

R. Plonsey and R.C. Barr, *Bioelectricity*, Plenum Publishing Corporation, NY (1989).

R Pool, Heart like a wheels, *Science* **247**, 1294–1295 (1990).

W.H. Press, Flannery B.P., S.A. Teukolsky and W.T. Vetterling, *Numerical recipes in C*, Cambridge University Press Cambridge, New York, Port Chester, Melbourne, Sydney (1992).

L. Priebe and D.J. Breuckelmann, Simulation study of cellular electric properties in heart failure, *Circ.Res.* **82**, 1206–1223 (1998).

Z. Qu and A. Garfinkel, An advanced algorythm for solving partial differential equation in cardiac conduction, *IEEE Trams. Biomed. Eng.* **46**, 1166–1168 (1999).

Z. Qu, A. Garfinkel, P.S. Chen and J.N. Weiss, Mechanisms of discordant alternans and induction of reentry in simulated cardiac tissue, *Circulation* **102**, 1664–1670 (2000a).

Z. Qu, J. Kil, F. Xie, A. Garfinkel and J.N. Weiss, Scroll wave dynamics in a three-dimensional cardiac tissue model: roles of restitution, thickness, and fiber rotation, *Biophys. J.* **78**, 2761–2775 (2000b).

Z. Qu, J.N. Weiss and A. Garfinkel, Spatiotemporal chaos in a simulated ring of cardiac cells, *Phys.Rev.Lett.* **78**, 1387–1390 (1997).

Z. Qu, J.N. Weiss and A. Garfinkel, Cardiac electrical restitution properties and stability of reentrant spiral waves: a simulation study, *Am. J. Physiol.* **276**, H269–H283 (1999).

Z. Qu, J.N. Weiss and A. Garfinkel, From local to global spatiotemporal chaos in a cardiac tissue model, *Phys. Rev. E* **61**, 727–732 (2000c).

D.A. Rawling and R.W. Joyner, Characteristics of junctional regions between Purkinje and ventricular muscle-cells of canine ventricular subendocardium, *Circ Res* **60**, 585–585 (1987).

M.L. Riccio, M.L. Koller and R.F. Gilmour Jr, Electrical restitution and spatiotemporal organization during ventricular fibrillation, *Circ Res* **84**, 955–963 (1999).

J.J. Rice, M.S. Jafri and R.L. Winslow, Modeling gain and gradedness of $Ca^{2+}$ release in the functional unit of the cardiac diadic space, *Biophys. J.* **77**, 1871–1884 (1999).

H.H. Rotermund, W. Engel, M. Kordesch and G. Ertl, *Nature* **343**, 355– (1990).

B.J. Roth and W. Krassowska, The induction of reentry in cardiac tissue. the missing link: How electric fields alter transmembrane potential., *Chaos* **8**, 204–220 (1998).

S. Rush and H. Larsen, A practical algorithm for solving dynamic membrane equation, *IEEE Trans Biomed Eng* **25**, 389–392 (1978).

F.H. Samie, O. Berenfeld, J. Anumonwo, S.F. Mironov, S. Udassi, J. Beaumont, S. Taffet, A.M. Pertsov and J. Jalife, Rectification of the background potassium current: a determinant of rotor dynamics in ventricular fibrillation, *Circ. Res.* **89**, 1216–1223 (2001).

R.C. Saumarez, A.J. Camm, A. Panagos, J.S. Gill, J.T. Stewart, M.A. de Belder, I.A. Simpson and W.J. McMenna, Ventriculat fibrillation in hypertrophic cardiomyopathy is assosiated with increased fractionation of paced right ventricular electrograms, *Circulation* **86**, 467–474 (1992).

F. Siegert and C.J. Weijer, Three dimensional scroll waves organize dictyostelium slugs, *Proc. Natl. Acad. Sci. USA.* **89**, 6433–6437 (1992).

A. SippensGroenewegen, H. Spekhorst, N.M. van Hemel, J.H. Kingma, R.N.W. Hauer, M.J. Janse and A.J. Dunning, Body surface mapping of ectopic left and right ventricular activation: QRS spectrum in patients without structural heart disease, *Circulation* **82**, 879–896 (1990).

A.J. Stewart, J.D. Allen, A.B. Devine and A.A. Adgey, Effects of blockade of fast and slow inward current channels on ventricular fibrillation in the pig heart, *Heart* **76**, 513–519 (1996).

D.D. Streeter, M.M. Spotnitz, D.P. Patel, J.Jr. Ross and E.H. Sonnenblick, Fiber orientation in the canine left ventricle during diastole and systole, *Circ. Res.* **24**, 339–347 (1969).

D.D.Jr. Streeter, Gross morphology and fiber geometry of the heart, In *Handbook of physiology. - Section 2: The cardiovascular system, Volume I: The heart* pages 61–112 Bethesda, MD (1979). Am. Physiol. Soc.

S. Tawara, *Das Reizleitungssystem des Saügetierherzens. Eine anatomisch-histologische Studie über das Atrioventrikularbündel und die Purkinjeschen Fädern*, Gustav Fischer Verlag Jena (1906).

C.E. Thomas, The muscular architecture of the ventricles of hog and dog hearts, *Am. J. Anat.* **101**, 17–57 (1957).

N. Trayanova, Concepts of ventricular defibrillation, *Phil.Trans.R.Soc.Lond.A.* **359**, 1327–1337 (2001).

T. Uchida, M. Yashima, M. Gotoh, Z. Qu, A. Garfinkel, J.N. Weis, M.C. Fishbein, W.J. Mandel, P.S. Chen and Karagueuzian H.S., Mechanism of acceleration of functional reentry in the ventricle: effects of ATP-sensitive potassium channel opener, *Circulation* **99**, 704–712 (1999).

A. van Oosteroom, Forward and inverse problems in electrocardiography, In A.V. Panfilov and A.V. Holden, editors, *Computational Biology of the Heart* pages 295–343 Chichester (1996). Wiley.

A. van Oosteroom and T.F. Oostendorp, *Electric volume conduction in bio-medicine*, Catholic University Nijmegen Nijmegen, The Netherlands. (1999).

J.A. Vassalo, D.M. Cassidy, F.E. Marchlinsky, A.E. Buxton, H.L. Waxman, J.U. Doherty and M.E. Josephson, Endocardial activation of the left bundle branch block, *Circulation* **69**, 914–923 (1984).

P.G. Volders, K.R. Sipido, E. Carmeliet, R.L. Spatjens, H.J. Wellens and M.A. Vos, Repolarizing $K^+$-currents $I_{to1}$ and $I_{Ks}$ are larger in the right than left canine ventricular myocardium, *Circulation* **99**, 206–210 (1999).

F.N. Wilson, F.D. Johnston, A.G. Macleod and P.S. Barker, Electrocardiograms that represent the potential variations of a single electrode, *Am. Heart J.* **9**, 447–471 (1934).

F.N. Wilson, F.D. Johnston, F.F. Rosenbaum, H. Erlanger, C.E. Kossmann, H. Hecht, N. Cotrim, R. Menezes de Olivieira, R. Scarsi and P.S. Barker, The precordial electrogram, *Am. Heart J.* **27**, 19–85 (1944).

A.T. Winfree, Spiral waves of chemical activity, *Science* **175**, 634–636 (1972).

A.T. Winfree, Electrical instability in cardiac muscle: Phase singularities and rotors, *J.Theor. Biol.* **138**, 353–405 (1989).

A.T. Winfree, Electrical turbulence in three-dimensional heart muscle, *Science* **266**, 1003–1006 (1994).

F.X. Witkowsky, L.J. Leon, P.A. Penkoske, W.R. Giles, M.L. Spano, W.L. Ditto and A.T. Winfree, Spatiotemporal evolution of ventricular fibrillation, *Nature* **392**, 78–82 (1998).

R.L. Woosley, New antiarrhythmic drugs, In D.P. Zipes and J. Jalife, editors, *Cardiac electrophysiology. From cell to bedside, 3rd edition* pages 939–943 Philadelphia (1999). Saunders.

C.R. Wyndham, M.K. Meeran, T. Smith, R.M. Engelman, S. Levitsky and K.M. Rosen, Epicardial activation in human left anterior fascicular block, *Am J Cardiol* **44**, 638–644 (1979a).

C.R. Wyndham, M.K. Meeran, T. Smith, A. Saxena, R.M. Engelman, S. Levitsky and J.P. Roos, Epicardial activation of the intact human heart without conduction defect, *Circulation* **59**, 161–168 (1979b).

C.R. Wyndham, T. Smith, M.K. Meeran, R. Mammana, S. Levitsky and K.M. Rosen, Epicardial activation in patients with left bundle branch block, *Circulation* **61**, 696–703 (1980).

A.N. Zaikin and A.M. Zhabotinsky, Concentration wave propagation in two-dimensional liquid-phase self-organising system, *Nature* **225**, 535–537 (1970).

C.W. Zemlin and A.V. Panfilov, Spiral waves in excitable media with negative restitution, *Phys. Rev. E* **63**, 041912–041914 (2001).

A.C. Zygmunt, G.T. Edelstone, G.P. Thomas, V.V. Nesterenko and C. Antzelevitch, Larger late sodium conductance in m cells contributes to electrical heterogeneity in canine ventricle, *Am. J. Physiol. Heart Circ. Physiol.* **281**, H689–H697 (2001).

A.C. Zygmunt, R.J. Goodrow and C. Antzelevitch, $I_{NaCa}$ contributes to electrical heterogeneity within the canine ventricle, *Am. J. Physiol. Heart Circ. Physiol.* **278**, H1671–H1678 (2000).

# Samenvatting

De contracties van het hart worden veroorzaakt door elektrische golven van excitatie die door het hartweefsel propageren. De overdracht van informatie door excitatiegolven is een vaak voorkomend fenomeen in de biologie, en vindt plaats in zenuw- en spierweefsel, zoals het hart. Modelleren in de elektrofysiologie is één van de belangrijkste en boeiendste voorbeelden van de toepassing van theoretische en computationele fysica in de geneeskunde en biologie. Deze tak van de wetenschap ontstond meer dan vijftig jaar geleden met het Hodgkin-Huxley model voor de propagatie van excitatie in zenuwcellen [Hodgkin and Huxley 1952], dat de Nobelprijs won in 1963. Later werd het modelleren eveneens toegepast op hartweefsel door Noble [1962] en FitzHugh [1961], en deze modellen werden verder verfijnd naarmate de experimentele technieken om de eigenschappen van celmembranen te onderzoeken, verbeterd werden [Beeler and Reuter 1977, Luo and Rudy 1991, 1994, Noble et al. 1998]. Het bleek dat onregelmatigheden in de pulspropagatie in het hart aan de basis liggen van de gevaarlijkste hartritmestoornissen en plotse hartstilstanden, die één sterfgeval op tien in geïndustrialiseerde landen op hun rekening nemen [Winfree 1994].

Vanuit een fysisch standpunt is het hart een exciteerbaar medium aangedreven door *limit-cycle* oscillaties [Glass 1996]. Een exciteerbaar medium is een continu systeem waarin, zonder bijkomende invloed, een evenwichtstoestand heerst. Een kleine, maar eindige verstoring zal aanleiding geven tot een excitatie, die een relatief lange duur heeft, vooraleer het evenwicht hersteld wordt (in hartweefsel spreken we van een actiepotentiaal). De excitatie doet zich voor als een elektrische golf die de hartspier aanzet tot contracties. De voortplanting van een golf in een exciteerbaar medium volgt twee belangrijke regels:

1. een geprikkelde cel kan een elektrische puls naar haar buurcellen geleiden, waardoor een excitatiegolf ontstaat.
2. na een golf wordt een zogenaamde refractorische periode waargenomen, gedurende de welke geen tweede golf kan propageren.

Een bijzonder verschijnsel dat waargenomen wordt in exciteerbare media is het proces van circulatie of *reentry*. Indien we een ring van prikkelbaar weefsel beschouwen waarin we een golf in één richting laten propageren, zien we dat de golf een volledige omloop maakt in een tijd $l/CV$ waarin $CV$ de golfsnelheid is en $l$ de lengte van de ring. Indien deze tijd groter is dan de refractorische periode, zal de golf onbeperkt blijven roteren. Dit is een voorbeeld van één-dimensionale reentry.

Laten we dit fenomeen uitbreiden naar een twee-dimensionaal medium. Beschouw in het medium een niet-exciteerbaar obstakel en een vlak golffront dat in één richting propageert en grenst aan het obstakel. We merken dat verschillende punten van het golffront langs verschillende banen bewegen. De golftip begint te roteren rond het obstakel, terwijl het golffront ver van het obstakel rechtlijnig blijft propageren. Dit

resulteert in de kromming van een oorspronkelijk vlak golffront en heeft een stationaire spiraalgolf tot gevolg, die met een zekere periode roteert. Het blijkt dat spiraalgolven eveneens kunnen ontstaan in media zonder obstakels, waar ze dan roteren om de refractorische staart van hun tip.

Roterende spiraalgolven, eveneens gekend als rotors [Winfree 1972] of vortices [Agladze and Krinsky 1982], komen voor in heel wat verschillende niet-lineaire prikkelbare media. Ze worden waargenomen in populaties van *Dictyostelium discoideum* amoebe [Siegert and Weijer 1992], in het netvlies [Gorelova and Bures 1983], in hartweefsel [Allessie et al. 1973, Davidenko et al. 1991] en *Xenopus* oöcyten [Lechleiter et al. 1991]. Ze werden eveneens ontdekt in fysico-chemische systemen zoals in oscillerende reacties [Zaikin and Zhabotinsky 1970, Winfree 1972] en in heterogene catalyse [Rotermund et al. 1990].

Het normale hartritme wordt bepaald door de sinusknoop, een gebied van gespecialiseerde cellen die bij een mens in rust ongeveer zeventig pulsen per minuut genereert. Een spiraalgolf in hartweefsel heeft een periode die twee- tot driemaal kleiner is dan de periode van de sinusknoop. De spiraalgolf neemt de rol van de sinusknoop over, waardoor het hart met een versneld ritme contraheert. Dit versneld hartritme wordt tachycardia genoemd, een ernstige hartritmestoornis. Vaak zal tachycardia vervallen in een toestand waarin het excitatiepatroon van het hart ruimtelijk gedesynchroniseerd is. In zo'n toestand kan de hartspier onmogelijk efficiënt contraheren en het pompen stopt. Deze toestand wordt ventrikulaire fibrillatie genoemd, die de belangrijkste oorzaak is voor sudden cardiac death in de wereld [Pool 1990, Gettes et al. 1995].
Het exacte mechanisme van fibrillatie is nog steeds onbekend, maar er wordt vermoed dat het geassocieerd is aan de complexe dynamica van elektrische golven in het hart. Gedurende vier decennia's werd fibrillatie verklaard aan de hand van de hypothese van Moe et al. [1964]: een turbulent patroon bestaande uit verscheidene wandelende golffrontjes (wavelets) die ontstaan door heterogeniteiten in de refractorische periode van hartcellen. Een meer recente hypothese, die hiermee nauw verwant is, is 'geïnduceerde fibrillatie' [Jalife et al. 1998b]. Heterogeniteiten spelen hierin nog steeds een belangrijke rol, maar de wavelets worden in dit geval geïnduceerd door een stabiele bron die pulsen genereert aan een hoge frequentie. Fibrillatie verdwijnt wanneer de bron wordt verwijderd. Gray et al. [1995a] veronderstelden dat snel wandelende spiraalgolven aan de basis kunnen liggen van ventrikulaire fibrillatie. Andere studies hebben het ontstaan van VF trachten te verklaren als een faseovergang van stabiele spiraalgolven naar een complex turbulent patroon. Stabiliteitsanalyse heeft aangetoond dat deze overgang kan ontstaan door het openbreken van de spiraalgolven, dat een spontane generatie van nieuwe excitatiebronnen tot gevolg heeft. Dit kan het resultaat zijn van een oneindig dimensionale Hopf bifurcatie [Courtemanche et al. 1993] of andere mechanismen opgesomd in [Fenton et al. 2002].
Er werden gelijkaardige mechanismen vooropgesteld voor andere hartritmestoornissen. De zogenaamde monomorfische tachycardias produceren een periodieke elektrocardiogram (ECG). Deze hartritmestoornis zou geassocieerd zijn aan de stationaire rotatie van een excitatiegolf in het hart [Pertsov et al. 1993]. Andere soorten hartritmestoornissen zijn polymorfische tachycardia die aanleiding geven tot een niet-periodische ECG en *torsades de pointes* die twee-periodische ECG's produceren. Recente hypothesen verklaren deze hartritmestoornissen door niet-stationaire spiraalgolven [Gray et al. 1995a], die weliswaar een meer stationair gedrag hebben dan gedurende fibrillatie.

Belangrijk om op te merken is dat al deze fenomenen waargenomen werden in harten

van verschillende dieren: konijn, hond, etc. Het hart van deze dieren verschilt van een menselijk hart in grootte en heeft andere weefseleigenschappen. Onderzoek op het mensenhart is heel beperkt en de redenen hiervoor zijn duidelijk: het is onmogelijk om op een levend hart 500 elektroden aan te brengen gedurende een hartritmestoornis om de elektrische excitatiepatronen vast te leggen of de contracties stop te zetten opdat optische methodes zouden kunnen toegepast worden. Het enige waarover men beschikt zijn meervoudige elektrocardiogrammen, enkele NMR beelden en onderzoek van het magnetische veld van het hart. Spijtig genoeg zijn deze methodes niet zo nauwkeurig en geven slechts een zeer algemeen beeld van de excitatie van het hart. Dit betekent dat er nieuwe methodes moeten ontwikkeld worden om de experimentele data bij dieren te kunnen projecteren op het mensenhart. Het zou eveneens belangrijk zijn om excitatiepatronen in het hart te koppelen aan medisch meetbare signalen, zoals elektrocardiogrammen. Een veelbelovende methode is dat van het computationeel modelleren. Deze methode wordt veelvuldig gebruikt in andere takken van de wetenschap, zoals in de aerodynamica, maar haar gebruik in biomedisch onderzoek staat nog in zijn kinderschoenen. Het idee van een realistisch computermodel voor de golfpropagatie in het hart is meer dan 20 jaar oud (zie overzicht in [Panfilov 1997]). De oudste modellen waren anatomisch gezien niet nauwkeurig genoeg en hadden een slechte ruimtelijke resolutie. Onlangs werd er een gedetailleerd model van het hondenhart ontwikkeld in [Panfilov and Keener 1995a] op basis van anatomische data in [Nielson et al. 1991] en werd succesvol toegepast op de studie van ventrikulair fibrillatie [Gray et al. 1995b]. Spijtig genoeg worden zulke hartsimulaties maar zelden uitgevoerd en ze werden nog niet systematisch toegepast op belangrijke klinische situaties.

In deze thesis bespreken we de ontwikkeling van een anatomisch computermodel van de menselijke ventrikels, dat kan gebruikt worden voor de studie van reentrant hartritmestoornissen (vortices). Allereerst, ontwikkelen we een elektrofysiologisch nauwkeurig model van de elektrische eigenschappen van menselijk ventrikulair hartweefsel. We beschikken eveneens over anatomische data van de menselijke ventrikels, wat ons toelaat de complexe geometrie van de ventrikels vast te leggen. Bovendien bevat deze data eveneens informatie over de spiervezeloriëntatie in elk punt van de ventrikels. Dit laat ons uitendelijk toe verschillende golfpatronen in de menselijke ventrikels te simuleren en de invloed van bepaalde medicijnen na te gaan.

## Modellen van het menselijk ventrikulair weefsel

In een eerste fase ging onze aandacht uit naar de ontwikkeling van een elektrofysiologisch model van het menselijk ventrikulair weefsel. Aangezien we dit model wensen te gebruiken voor de studie van hartritmestoornissen en hun invloed op ECG's, moeten we bijzondere aandacht hebben voor volgende punten: (1) het model moet de vorm van de actiepotentiaal (AP) zo getrouw mogelijk na bootsen, dit teneinde realistische elektrocardiogrammen te genereren [Plonsey and Barr 1989]. Spiraalgolven, of vortices in het algemeen, worden geassocieerd met de ritmestoornissen die we wensen te bestuderen. Het is dan belangrijk de dynamica van spiraalgolven op een nauwkeurige manier te modelleren, wat neerkomt op een realistische weergaven van de restitutie eigenschappen van het weefsel. Dit fenomeen is het gevolg van de afhankelijkheid van de elektrofysiologische eigenschappen aan de tijd verstreken sinds een voorgaande activatie: hoe

korter dit tijdsinterval, hoe korter de duur van een actiepotentiaal ($APD$-restitutie) en hoe trager een puls propageert ($CV$-restitutie).

### Een drie-variabelen model

Ons doel was een eenvoudig model te ontwikkelen met zo weinig mogelijk variabelen, maar waarmee we in staat zijn realistische actiepotentialen en restitutiecurven te bekomen. De meest eenvoudige modellen zijn van het FitzHugh-Nagumo (FHN) type [FitzHugh 1961, Nagumo et al. 1962, Aliev and Panfilov 1996] en bezitten twee variabelen. In 1998 ontwikkelden Fenton en Karma een drie-variabelen model, dat de eigenschappen van een cel op een fenomenologische wijze nabootste [Fenton and Karma 1998]. We ontwikkelden eveneens een drie-variabelen model, waarin de parameters een eenduidig verband tonen met de eigenschappen van het weefsel.

Het bekomen model is een verbetering ten opzichte van klassieke FHN-modellen en is computationeel efficiënt, maar kampt nog altijd met een aantal problemen: de vorm van de actiepotentiaal is, zoals in de meeste gesimplifieerde modellen, geïdealiseerd, waardoor het niet zeker is of getrouwe elektrocardiogrammen mogelijk zijn. Bovendien mist het model een elektrofysiologische onderbouw: De snelle inwaartse stroom mag dan op een relatief eenduidige manier verbonden zijn met de snelle inwaarste natriumstroom $I_{Na}$, de hier gedefinieerde trage stromen zijn abstracte grootheden die ingevoerd werden om een aantal fenomenen na te bootsen. Ze kunnen in geen geval geassocieerd worden met kalium- of calciumstromen in echt weefsel. De $CV$-restitutie wordt daarentegen met ons model beter beschreven dan met klassieke FHN-vergelijkingen, waar het fenomeen slechts met één parameter gemodelleerd wordt, terwijl het in ons geval beschreven wordt met behulp van een dynamische variabele.

### Een gereduceerd ionair model

Recent werd een ionair model voor menselijk ventrikulair weefsel ontwikkeld door Priebe en Beuckelmann [Priebe and Breuckelmann 1998] (PB). Dit model bestaat uit een gedetailleerde beschrijving van de transmembrane stromen en houdt eveneens rekening met de complexe dynamica van de $Ca^{2+}$-ionen binnen de cel, de zogenaamde *calcium handling*. De complexiteit van het model maakt het inefficiënt voor de simulatie van belangrijke golfpatronen in twee- of drie-dimensionale media. Op basis van ideeën die we gebruikten bij het ontwikkelen van het drie-variabelen model, reduceerden we het aantal variabelen van dit model in drie stappen: (1) allereerst werden een aantal zorgvuldig gekozen variabelen adiabatisch geëlimineerd; (2) door gebruik te maken van computationele *voltage clamp* experimenten slaagden we erin de twee inactivatie variabelen van de snelle inwaartse stroom en de twee activatie variabelen van de kaliumstroom telkens tot één variabele te herleiden; (3) de intracellulaire dynamica van ionen blijkt slechts in welbepaalde situaties een rol te spelen, die we verder niet wensen te onderzoeken, en was bovendien een bron van instabiliteiten in het originele PB model. We verwaarloosden bijgevolg deze processen, door alle ionenconcentraties als constant te beschouwen.

Het bekomen model bestaat uit zes variabelen (13 in het originele) en vertoont dezelfde eigenschappen als het oorspronkelijk model wat betreft de actiepotentiaal en de restitutiecurven. Bovendien is het gereduceerd model numeriek stabiel, wat ons toelaat relatief

snelle simulaties op te zetten zonder de link naar de onderliggende elektrofysiologie te verliezen.

### Bifasische restitutie

Zoals reeds vermeld, speelt de restitutie van de duur van de actiepotentiaal een belangrijke rol in de stabiliteit van spiraalgolven. De zogenaamde restitutie-hypothese voorspelt dat een spiraalgolf instabiel wordt en aanleiding kan geven tot turbulente patronen, wanneer $|dAPD/dDI|$ groter wordt dan 1 voor bepaalde diastolische intervallen ($DI$). Het diastolische interval is de tijd verstreken sinds het einde van de voorgaande actiepotentiaal. Experimenten op het mensenhart zijn beperkt en men beschikt daarom slechts over weinig informatie wat $APD$-restitutie in het menselijk ventrikulair weefsel betreft. In de meeste gevallen werden monofasische $APD$-restitutiecurven waargenomen [Morgan et al. 1992a, Nánási et al. 1996], curven die een monotoon stijgend exponentieel verloop vertonen. Een aantal studies hebben echter een ander type restitutiecurven ontdekt, die bij kleine $DI$ een "bump" vertonen, en deze werden bifasische of supernormale restitutiecurven genoemd [Morgan et al. 1992b]. Dit fenomeen is nog steeds onverklaard, maar er wordt vermoed dat het veroorzaakt wordt door de complexe calcium-dynamica in de cel. Het is eveneens onduidelijk wat de invloed van zo'n restitutie kan zijn op de stabiliteit van een spiraalgolf, alhoewel een aantal simulatiestudies laten vermoeden dat nieuwe types instabiliteiten te verwachten zijn: Qu et al. [1997] vonden dat chaos kon ontstaan in een ring met bifasische restitutie, wanneer het dalende deel van de bump steil genoeg wordt. Zemlin and Panfilov [2001] modelleerden een monotoon dalende curve en vonden dat wanneer de afgeleide kleiner werd dan -1, de spiraalgolf openbrak, ver van de kern, terwijl in het monotoon stijgend geval chaotische activatie zich steeds dicht bij de spiraaltip ontwikkelde.

Om bifasische restitutiecurven te bekomen wijzigden we ons gereduceerd ionair model door de calciumstroom $I_{Ca,L}$ afhankelijk te maken van het diastolische interval. We bekwamen een autonoom systeem (zonder expliciet $DI$ te gebruiken) door het invoeren van een nieuwe variabele $d_s$ waarvan de waarde rechtstreeks in verband kon gebracht worden met het diastolisch interval.

Met deze methode slaagden we erin, op een fenomenologische wijze, experimentele restitutiecurven bekomen door Morgan et al. [1992b] na te bootsen.

## Reentry en fibrillatie in 2D

### Normaal myocardium

Voor de normale parameterwaarden van het gereduceerd ionair model waren we in staat spiraalgolven te genereren in vierkant 2D medium, door gebruik te maken van een S1-S2 protocol. Allereerst stimuleerden we één zijde van het medium tien maal met een periode van 350 ms (S1), wat resulteerde in 10 vlakke golven. Eénmaal de refractorische staart van de laatste golf het midden voorbijkwam, stimuleerden we op die plaats het medium met een vlakke elektrode die slechts 3/4 zo lang was als de zijde van het medium. Zo ontstond een S2 golf die in tegengestelde richting propageerde (vergeleken met de S1 golven) en aan zijn vrije uiteinde naar binnen krulde en zich

ontwikkelde tot een spiraalgolf. De spiraalgolf blijkt een frequentie te hebben van 3.3 Hz, wat in overeenstemming is met tachycardias van meer dan 180 pulsen/min. De baan van de tip van de spiraalgolf beschrijft een zogenaamde lineaire kern, met een diameter van 5 cm. Deze dynamica is karakteristiek voor spiraalgolven waargenomen in experimenten in dunne weefselpreparaten [Davidenko et al. 1991] en in wiskundige modellen van hartweefsel [Efimov et al. 1995, Fast et al. 1990]. De elektrocardiogram is typisch voor polymorfische ventrikulaire tachycardia [Clayton et al. 1995].

### De invloed van een $K^+$-kanaal opener

Experimenten op dierenharten hebben uitgewezen dat een bepaalde klasse medicijnen, de zogenaamde ATP-gevoelige kaliumkanaal openers, de frequentie van reentry kunnen verhogen en fibrillatie in de hand werken [Uchida et al. 1999]. In ons model zijn spiraalgolven stabiel en roteren met een frequentie van ongeveer 3 Hz. We hebben de effecten van een ATP-gevoelige kaliumkanaal opener (cromakalim genaamd), nagebootst door de geleidbaarheden van de kaliumstromen $I_K$ en $I_{K1}$ te verhogen en door de extracellulaire kaliumconcentratie te laten toenemen.

Gebruik makende van hetzelfde S1S2-stimulatie protocol als in voorgaande sectie, simuleerden we reentry in een 2D-medium. De spiraalgolf breekt heel snel open, dicht bij de tip, en er onstaat een chaotische toestand waarin voortdurend spiraalgolven verdwijnen en nieuwe gevormd worden. De oorzaak van de instabiliteit is een steile restitutiecurve ($|dAPD/dDI| > 1$). De elektrocardiogram vertoont een onregelmatig patroon, typisch voor fibrillatie. Fourier analyse van deze cardiogram leert ons dat het weefsel met een dominante frequentie wordt geactiveerd die rond 6 Hz ligt (alhoewel we met een gefractioneerd spectrum te maken hebben), dubbel zoveel als gedurende normale reentry. Onze resultaten in een model voor menselijk hartweefsel lijken dus de experimenteel waargenomen invloed van ATP-gevoelige kaliumkanaal openers te reproduceren [Uchida et al. 1999].

### De invloed van bifasische restitutie

Het uitgangspunt van de volgende simulaties was een bifasische restitutiecurve die gefit was aan experimentele data bekomen door Morgan et al. [1992b]. De spiraalgolf blijkt instabiel te zijn en breekt meermaals open, waarbij nieuwe spiraalgolven worden gevormd. Volgens de restitutie-hypothese zou dit te wijten zijn aan een "steil gebied" in de restitutiecurve. De minimale waarde voor de afgeleide bedraagt slechts -0.5, terwijl de maximale waarde rond 2 ligt, boven de instabiliteitsgrens. We vermoeden bijgevolg dat de waargenomen instabiliteit een klassieke instabiliteit is, in de zin dat deze plaatsvindt in het monotoon stijgend deel van de restitutiecurve. Om dit te controleren, maakten we het stijgend deel van de curve vlakker (afgeleide $< 1$), zonder het dalend deel te wijzigen, door bepaalde parameters van het model te wijzigen. In dit geval bleek de spiraalgolf uiterst stabiel, wat ons vermoeden bevestigt.

We bestudeerden de invloed van het dalend deel van de bifasische bump in het geval van een vlak (en dus stabiel) stijgend deel. Door gepaste parameters te wijzigen, zijn we in staat verschillende configuraties te bestuderen. Indien de minimale waarde voor de afgeleide boven -1 ligt, vinden we opnieuw een stabiele spiraalgolf. Wanneer de

minimale afgeleide verder werd verminderd bekwamen we een toegenomen instabiel gedrag: de tip van de spiraalgolf begon een complexe baan te beschrijven, met een drift van de spiraalgolf tot gevolg. Het openbreken van de spiraalgolf duurde hier evenwel langer dan in het oorspronkelijk geval en turbulente patronen ontwikkelden zich pas na een dertigtal rotaties. Deze observaties lijken overeen te komen met resultaten bekomen door Zemlin and Panfilov [2001].

### $Ca^{2+}$-blokkers in de strijd tegen ventrikulaire fibrillatie

Ventrikulaire fibrillatie (VF) is één van de belangrijkste doodsoorzaken in de geïndustrialiseerde wereld [Gettes et al. 1995]. De enige efficiënte behandeling van VF was tot nu toe elektrische defibrillatie: het aanbrengen van een sterk extern elektrisch veld, dat het normale sinusritme kan herstellen door de eliminatie van abnormale bronnen van excitatie [Trayanova 2001]. Recente studies hebben echter aangetoond dat het toedienen van medicijnen de complexiteit van activatiepatronen gedurende VF kan verminderen [Chorro et al. 2000a,b, Samie et al. 2001] of VF zelfs stoppen [Garfinkel et al. 2000]. Samie et al. toonden dat verapamil, een $Ca^{2+}$-blokker, VF kon converteren in ventrikulaire tachycardia (VT) in experimentele studies op konijnenharten en in 2D-simulaties [Samie et al. 2001]. In studies uitgevoerd door Riccio et al. [1999], belette verapamil de ontwikkeling van VF. Garfinkel et al. [2000] toonden aan dat het medicijn bretylium VF kan converteren in VT in experimenten op varkensharten en in 2D- en 3D-simulaties gebruik makende van het Luo-Rudy model [Luo and Rudy 1991].

We onderzochtten de overgang van VF naar VT na toediening van het medicijn verapamil in 2D-simulaties. Het effect van verapamil werd als volgt gemodelleerd, net als in Qu et al. [1999]:

$$g'_{Ca} = g_{Ca} \cdot \left[(1-p) + p \cdot e^{-\frac{t-t_0}{\tau}}\right], \quad t \geq t_0 \tag{0.1}$$

waarin $g'_{Ca}$ de geleidbaarheid van het calciumkanaal voorstelt onder invloed van verapamil, $g_{Ca}$ de normale geleidbaarheid, $p$ de maximale blokkade van de calciumstroom, $t$ de tijd, $t_0$ het tijdstip waarop verapamil wordt toegediend en $\tau$ de relaxatietijd voor de inwerking van het medicijn. In wat volgt gebruikten we $p = 0.75$ en $\tau = 1$s.

In de 2D-simulaties zagen we een duidelijke overgang van complexe activatie naar georganiseerde activatie gepaard gaande met een vermindering van het aantal spiraalgolven. In het geval van 'no-flux' randvoorwaarden evolueerde de chaotische activatie naar een stabiele toestand met 6 spiraalgolven. De gemiddelde frequentie nam toe tot 10.3 Hz, wat qualitatief overeenkomt met de experimenten van Chorro et al. [2000a,b].

### Het $\gamma$-model

De numerieke nauwkeurigheid van een model voor propagerende actiepotentialen is volkomen bepaald door de upstroke van de actiepotentiaal. Hoe steiler deze is, hoe minder nauwkeurig het model is. Om betrouwbare simulaties op te zetten moet het medium dan over een fijn rooster gediscretizeerd worden, wat ten koste gaat van de computationele tijd. De upstroke van een actiepotentiaal is enkel afhankelijk van de

natriumstroom $I_{Na}$, daar het de enige actieve stroom is op dat ogenblik. Het blijkt dat de upstroke in ionaire modellen heel steil is, wat in de meeste gevallen leidt tot een minimale resolutie van 0.25 mm, om numerieke fouten te beperken. Om de berekeningen sneller te laten verlopen, wensen we de resolutie te verkleinen, zonder numerieke nauwkeurigheid en de eigenschappen van het model te wijzigen. Hiertoe ontwikkelden we een methode die ons toeliet de snelle inwaartse natriumstroom te vertragen gedurende de upstroke, waardoor deze minder steil werd. Dit liet ons toe de resolutie te verkleinen tot 0.5 mm, wat een faktor 20 tijdswinst betekende in 3D simulaties.

### Een anatomisch computermodel van de menselijke ventrikels

Voor ons model maken we gebruik van anatomische data die in een computerformaat werden getransformeerd door Hren [1996]. Het basisidee van de aanpak van Hren [1996], was dat het myocard onderverdeeld kan worden in twee distincte anatomische gebieden: compacta, met een sterk georganiseerde vezelstructuur met lokaal grote variaties in vezeloriëntatie en trabeculae, waarvan de vezelstructuur op een meer uniforme wijze georganiseerd is en onafhankelijk is van de structuur van de compacta. Bovendien zitten de compacta bevat in onregelmatige, maar relatief gladde oppervlakken, terwijl het oppervlak van de trabeculae meer complex is. In [Hren 1996] wordt het grensoppervlak van de compacta beschreven door een globaal geparametriseerd model. Aangezien de trabeculae een eenvoudigere vezelstructuur, maar een meer complex oppervlak hebben, werd hier gebruik gemaakt van de interpolatie van digitale data voor de lokale representatie van het endocardiale oppervlak. Beide typen van representatie, lokaal en globaal, werden hiërarchisch gestructureerd.

De harmonische ontwikkelingsmethode werd gebruikt om de belangrijkste oppervlakken te reconstrueren van deze data. Een afzonderlijke set van parameters, met onder andere de oorsprong van de ontwikkeling en de ontwikkelingscoëfficiënten, werd voor elk oppervlak afzonderlijk geëvalueerd. De nauwkeurigheid van de benadering werd bepaald door berekening van de rms-fout (root-mean-square). De parameters werden aangepast zodat de rms-fout kleiner was dan 0.5 mm voor elk oppervlak. Dit is een aanvaardbare fout aangezien de ruimtelijke resolutie van het model 0.5 mm bedroeg. Bovendien werd de betrouwbaardheid van de reconstructie visueel geverifieerd.

Gedurende de constructie van het model, werden de voxels opgeslagen in een $220 \times 220 \times 220$ kubus met de linker ventrikulaire apex in de voxel met coördinaten (110,110,1). De vezeloriëntatie werd geïnterpoleerd uit data van Streeter [1979], Nielson et al. [1991], waarna aan elke voxel van het hart een eenheidsvector in de zin van de spiervezel werd toegekend.

Het model van Hren [1996] bezit dus de nodige details in verband met de anatomische structuur van het hart en de spiervezeloriëntatie.

### Reentry en fibrillatie in de menselijke ventrikels

Vooraleer spiraalgolven te onderzoeken in de menselijke ventrikels, simuleerden we de normale activatie van de menselijke ventrikels. Hiertoe werden zes endocardiale gebieden, de *insertion sites* genaamd, simultaan gestimuleerd. De locatie van de insertion

sites werd door Hren [1996] bepaald en komt overeen met de verbindingspunten van het Purkinje netwerk met de ventrikulaire spier. Bijgevolg zijn dit de gebieden die in de ventrikels het eerst worden geactiveerd. Onze simulatieresultaten vertonen grote overeenkomst met de experimentele data van Durrer et al. [1970], wat ons liet besluiten dat het model geschikt was voor het simuleren van elektrische golven in de menselijke ventrikels.

**Reentry in het rechter en linker ventrikel en in het septum**

We simuleerden spiraalgolven (of vortices) in het rechter en linker ventrikel en in het harttussenschot, door gebruik te maken van een S1S2-stimulatie protocol. Eenmaal de S1-golf het grootste deel van de ventrikels heeft doorlopen, wordt de S2-stimulus op een vooraf bepaalde plaats toegediend. De S2-golf heeft één vrije uiteinde, waarrond een spiraalgolf kan ontstaan.
In het rechter ventrikel en in het septum bekwamen we vrij stabiele vortices, die roteerden met een periode van ongeveer 220 ms. In het geval van een vortex in het rechter ventrikel werd in het linker ventrikel een V-patroon waargenomen; een gebied waar golven, beide afkomstig van dezelfde spiraalgolf, met elkaar botsen en elkaar annihileren. Zo'n patroon werd eveneens in experimenten waargenomen in Jalife et al. [1998b]. De ECG heeft een regelmatig patroon met variërende amplitude, wat typisch is voor polymorfische ventrikulaire tachycardia.
Het epicardiaal activatiepatroon voor de spiraalgolf in het septum vertoont een nieuw kenmerk: epicardiale *breakthroughs*. Dit fenomeen illustreert meteen de belangrijkste beperking van optische methodes: door louter epicardiale afbeeldingen te bekijken, zouden we in dit geval kunnen besluiten dat een aantal cellen van het hart disfunctioneren en spontane activatie vertonen (vaak ook *focal sources* genoemd). Deze cellen zouden met behulp van catheter ablatie kunnen verwijderd worden. Het is duidelijk dat zo'n ingreep in dit geval niet gepast is, daar de abnormale bron van excitatie een spiraalgolf is, die zich in het septum bevindt. Meteen worden de voordelen van het 3D-modelleren duidelijk.
De rotor die we in het linker ventrikel bekwamen vertoonde een veel onregelmatiger gedrag dan in het rechter ventrikel en brak zelfs open na een vijftal rotaties. Het grootste verschil tussen het rechter en linker ventrikel is de dikte van de ventrikulaire wand, en bijgevolg de rotationele anisotropie. Met rotationele anisotropie wordt de roterende spiervezeloriëntatie bedoeld als men gaat van epi- naar endocardium, of omgekeerd. In de dikkere linker ventrikulaire wand is deze rotatie groter. Verschillende simulatiestudies hebben aangetoond dat rotationele anisotropie instabiliteiten kan veroorzaken in vortices en die in sommige gevallen doen openbreken in een complex patroon dat op fibrillatie lijkt [Panfilov and Keener 1995b, Fenton and Karma 1998]. In ons geval vertoont de vortex een onregelmatige baan en breekt open na botsing met de rand van de ventrikels, waarna een complexe toestand zich kan ontwikkelen. Deze resultaten lijken de hypothese te ondersteunen dat de ontwikkeling van VF gemakkelijker verloopt in het linker ventrikel, wat belangrijke medische implicaties kan hebben.

### Ventrikulaire fibrillatie

Net als in de 2D-simulaties, bekwamen we een chaotische activatie van de ventrikels door de invloed van cromakalim te simuleren op een spiraalgolf. In het rechter ventrikel breekt deze na 2-3 rotaties open en er worden nieuwe vortices gecreëerd die het hart op een niet gesynchroniseerde wijze activeren. Het aantal vortices varieerde tussen 2-6, wat de hypothese die VF beschrijft als een klein aantal reentrant loops, lijkt te ondersteunen [Jalife et al. 1998b].

### De overgang van chaotische naar geordende activatie

We hebben de invloed van calciumkanaal blokkers op turbulente activatie eveneens onderzocht in het model van de menselijke ventrikels. Allereerst werd een chaotische toestand bekomen door de invloed van cromakalim na te bootsen. Na 5s werd het calciumkanaal geleidelijk geblokkeerd op een analoge wijze als in de 2D simulaties. Na ongeveer 2.5 s werd de elektrische activiteit regelmatig en slechts één enkele spiraalgolf werd nog waargenomen in het rechter ventrikel. Deze spiraalgolf vertoonde een drift van voorbijgaande aard en verankerde zich aan de vezelstructuur rond de pulmonale klep. Op dat ogenblik verlaagde de activatiefrequentie naar 5Hz en werd op de ECG een echte overgang van fibrillatie naar tachycardia waargenomen, wat blijkt overeen te komen met experimenten van Samie et al. [2001].